Production, Characterization, and Biodistribution of Lignin-Capped Silver Nanoparticles to Combat Multidrug Resistant Bacteria *In Vitro* and *In Vivo*

by

Jason Asnis

B. Eng., McGill University, 2015

A THESIS SUBMITTED IN PARTIAL FULFILLMENT OF

THE REQUIREMENTS FOR THE DEGREE OF

MASTER OF SCIENCE

in

THE FACULTY OF GRADUATE AND POSTDOCTORAL STUDIES

(PHARMACEUTICAL SCIENCES)

THE UNIVERSITY OF BRITISH COLUMBIA

(VANCOUVER)

April 2018

Abstract

One of the most important issues in healthcare today is the development of bacterial resistance to antibiotics which has created a generation of bacteria known as multidrug resistant (MDR) bacteria. Due to antibiotics' inability to treat these MDR bacteria metal and metal oxide nanoparticles have been gaining interest as antimicrobial agents. Among those, silver nanoparticles have been used extensively as broad spectrum antimicrobial agents.

Here we describe the production and characterization of silver nanoparticles made from the wood biopolymer lignin as a reducing and capping agent with excellent antimicrobial activity against MDR bacteria both *in vitro* and *in vivo*. We describe and compare the productions of these lignin-capped silver nanoparticles (L-AgNPs) both through a standard heating procedure and through a microwave-assisted synthesis. The L-AgNPs have been radioactively labeled using both iodine-123 and the novel radioisotope silver-111 to determine their biodistribution by SPECT/CT imaging after subcutaneous injection or intratracheal instillation. The particles were then tested for *in vitro* antimicrobial activity by broth dilution against a variety of Gram-positive and Gram-negative MDR clinical isolate bacterial strains and ATCC strains. They were also tested for efficacy in an *in vivo* cutaneous infection (abscess) model caused by biofilm-forming MDR bacterial strains.

The particles were produced using a simple, one-pot synthesis method and characterized by ultraviolet-visual spectroscopy, dynamic light scattering, x-ray diffraction, and scanning transmission electron microscopy. Characterization of the lignin-capped silver nanoparticles shows uniform spherical nanoparticles with a silver core and a lignin coating with a diameter of about 50 nm for both synthesis methods, but the microwave method was significantly faster (10 min vs. 3 days). The particles radioactively labeled with silver-111 were visible on SPECT/CT and were labeled with high efficiency, but produced a poor size distribution. The L-AgNPs radioactively labeled with iodine-123 and injected subcutaneously remained at the injection site up to 48 hours post-injection. The *in vitro* minimum inhibitory concentration (MIC) of L-AgNPs was ≤ 5 μg/mL for all tested bacterial strains, and a significant decrease in both abscess size and bacterial load was observed against *in vivo* infections caused by MDR strains of *S. aureus* and *P. aeruginosa*.

Lay Summary

Antibiotics are no longer able to treat all bacterial infections. For this reason, extremely small silver particles (nanoparticles) coated with a wood polymer called lignin have been developed to kill the bacteria that antibiotics can no longer treat. Two methods have been developed to produce these silver nanoparticles: a 3-day method that just uses gentle heating and a 10-min method that uses a microwave generator. These silver nanoparticles can be easily and reliably produced, and are effective at killing even the most drug-resistant bacteria. When they are applied directly to a bacterial infection in a mouse, the infected area decreases in size and overall bacterial count.

A radioactive tracer has been used to determine that nanoparticles directly injected into the site of a bacterial infection remain at that desired location. A new radioactive silver tracer has also been developed for this purpose.

Preface

The studies presented in this original thesis were developed and designed by Dr. Urs O. Häfeli and the author, Jason Asnis. Experiments were conducted primarily at the University of British Columbia, Canada in the Häfeli Laboratory in the Faculty of Pharmaceutical Sciences under the supervision of Dr. Urs O. Häfeli who also provided revisions for the writing in this thesis. All research and experimental work was completed by the author except for the sections specified below.

In Chapter 2, the 72-hour aerobic synthesis method was developed in collaboration with Dr. Kristina Ivanova and Dr. Petya Stoyanova at the Universitat Politècnica de Catalunya under the supervision of Dr. Tzanko Tzanov.

In Chapter 4, the *in vitro* broth dilution antimicrobial testing was carried out by Yael N. Slavin under the supervision of Dr. Horacio Bach.

All *in vivo* studies described in this thesis were conducted under protocols that were reviewed and approved by the University of British Columbia Animal Care Committee. The biodistribution studies conducted in Chapter 3 were carried out in adherence to ACC protocol A16-0150 VECTor/CT Biodistribution and Imaging Studies II, and the cutaneous infection model conducted in Chapter 4 was performed in adherence to ACC protocol A14-0363.

Table of Contents

List of Tables

List of Figures

List of Abbreviations

Ag	Silver
$AgNO_3$	Silver Nitrate
AgNPs	Silver Nanoparticles
AMP	Antimicrobial Peptide
CFU	Colony Forming Unit
CT	Computed Tomography
CVD	Chemical Vapor Deposition
DI	Deionized
DLS	Dynamic Light Scattering
DMF	N-Dimethylformamide
DNA	Deoxyribonucleic Acid
HDP	Host Defense Peptide
I.V.	Intravenous
ICP	Inductively Coupled Plasma
IP	Intraperitoneal
L-AgNPs	Lignin-Capped Silver Nanoparticles (contains Ag^0 and AgCl)
LPS	Lipopolysaccharide
MBC	Minimum Bactericidal Concentration
MDR	Multidrug Resistant
MIC	Minimum Inhibitory Concentration
MPS	Mononuclear Phagocyte System
MS	Mass Spectrometry
MW	Microwave
NP	Nanoparticle

PBS	Phosphate Buffer Solution
PDR	Pandrug-Resistant
PVD	Physical Vapor Deposition
RNA	Ribonucleic Acid
ROS	Reactive Oxygen Species
SD	Standard Deviation
SPECT	Single-Photon Emission Computed Tomography
SQ	Subcutaneous
$t_{1/2}$	Half-Life
UV-Vis	Ultraviolet-Visible Spectroscopy
XDR	Extensively Drug-Resistant
XRD	X-Ray Diffraction

Acknowledgements

I would first like to thank my supervisor Dr. Urs O. Häfeli for the tremendous amount of support you have given me during my degree. You have pushed me to constantly strive for excellence and to consider problems from all possible angles. I am incredibly grateful for all of the knowledge and opportunities you have given me during my research.

I would also like to thank Dr. Harvey Wong, Dr. Horacio Bach, Dr. Vikramaditya Yadav, and Dr. Shyh-Dar Li for their time and support as part of my advisory committee.

I would like to thank Dr. Tara Mastren from Los Alamos National Lab (LANL) for helping us to acquire the ^{111}Ag from Oak Ridge National Lab (ORNL), and Dr. Valery Radchenko for helping with the purification.

I am also very grateful to Dr. Katayoun Saatchi, without your expertise, support, and willingness to help me out any time of day or night none of this would have been possible. I would also like to thank Dr. Kristina Ivanova and Dr. Petya Stoyanova for their help in starting this project, Yael N. Slavin for the generous amount of time she spent helping me with all of the bacterial work, and Dr. Daniel Pletzer for all of his patience and support in finally getting the mouse model to work.

Thank you to all of my lab members! Being surrounded by all of your great minds has been inspiring throughout my entire degree. Big shout out to the chirps, I don't think I would have made it here without all of you.

To my friends and family: you have all made this possible through your endless love and support, without all of you I would not be the person I am today and I am forever grateful.

Emma, thank you so much for everything you have done for me and for always being there for me no matter what. You have been the brightest part of my life, and it is beyond words how much you mean to me.

Finally, I would like to thank the Joint Programming Initiative on Antimicrobial Resistance for the financial support of this project.

Dedication

This work is dedicated to my grandparents

I know you would have loved to see me finish it.

Chapter 1: Introduction and Literature Review

1.1 General Introduction

One of the greatest healthcare challenges the world faces today is the spread of multidrug resistant (MDR) bacterial infections otherwise known as “superbugs” [1]. Bacterial infections are common in humans, but the development of MDR bacteria has resulted in a disturbing rise in the frequency and severity of these infections over the last two decades even in areas where high levels of sanitary infrastructure are in place. Infections that were once easily treatable have become increasingly more difficult to treat, and result in higher morbidity and mortality. For example, it has been suggested that by 2050 MDR bacteria could surpass cancer and kill up to 10 million people per year, however, current data reporting on morbidity and mortality due to MDR bacteria is unreliable and this estimate is a worst-case scenario [2]. The development of these MDR bacterial strains is likely due to the widespread overuse of antibiotics in both clinical and agricultural settings [3]. At this time, resistant organisms have been identified for all or nearly all available antibiotics, and the development of new antibiotics has slowed to a crawl [4-6]. Due to the inability of antibiotics to deal with the rising issue of MDR bacteria, the need for the development of novel, broad spectrum antimicrobials has arisen.

Many different possibilities for novel antimicrobials have been explored, and many more are still being investigated. The simplest strategy to combat the rise of MDR bacteria has been to revitalize old antibiotics by using them in combination with other antibiotics or with resistance breakers. For example, when using a β-lactam antibiotic against a resistant organism a β-lactamase inhibitor is added as a resistance breaker to overcome the bacterial resistance mechanism [7]. Similar strategies have been used for aminoglycoside-modifying enzyme inhibitors and antibiotic efflux pump inhibitors [8,9].

There is also increased interest in antimicrobial peptides (AMPs), or host defense peptides (HDPs) which have been isolated from a wide variety of natural sources such as bacteria, insects, frogs, and mammals [10-12]. These AMPs are naturally produced as part of an immune response, and they perform a wide variety of functions for their host including direct antimicrobial action against

a wide variety of Gram-negative and Gram-positive bacteria [13]. However, natural AMPs are quite often subject to enzymatic degradation and inconvenient optimization so a wide variety of synthetic systems have been developed to overcome these challenges [14-16].

Another interesting method of combatting MDR bacteria is phage therapy. Recently interest has grown in the use of specific viruses called bacteriophages that selectively infect bacteria. Bacteriophages are of particular interest for their ability to very specifically target bacterial strains and their highly effective antimicrobial activity against MDR bacteria [17,18]. The concept of phage therapy was introduced by Félix d'Hérelle in 1917, but unpredictable results, non-double-blinded studies, and the fact that this therapy actually used viruses contributed to public rejection of the therapy [19,20]. On top of this, when penicillin became easily available in the 1950s phage therapy was basically abandoned [21]. However, now that antimicrobial resistance is a hot topic in research phage therapy is once again being investigated.

Other areas of investigation include: natural compounds with antimicrobial activity, the use of liposomes for targeted delivery of antibiotics, the use of ultrasound waves alone or in addition to conventional antibiotics, and the development of RNA-based antisense agents to silence resistance genes [22-29]. There are many available options for combatting drug resistance but, perhaps the largest and fastest expanding field in the development of novel antimicrobials is nanotechnology.

The explosion of the nanotechnology field began in 2000 when the US launched the National Nanotechnology Initiative (NNI) with $497 million in funding [30]. Since then it has been at the forefront of scientific development with the 21st Century Nanotechnology Research and Development Act (NRDA) (Public Law 108-153) being signed into law in October of 2005 allowing for $3.7 billion in federal funding over a 4-year period. Since then the NNI has received $1.6, $1.5, and $1.2 billion dollars in funding for 2016 to 2018, respectively [31,32]. Nanotechnology includes a wide array of scientific fields ranging from manufacturing and energy storage to materials science and healthcare, and has already had many profound effects on our economy and society. Of particular interest is the development of nanoparticles (NPs) for drug delivery in healthcare.

The definition of what constitutes a NP varies slightly depending on the source, but in general they are objects with at least one dimension in the size range of about 1 to 100 nm and an average size of less than a micrometer [33,34]. There are a wide variety of different physical, chemical, and biological synthesis techniques which can be employed to tailor the size and shape of NPs depending on exact size or material requirements [35,36]. Many different applications for NPs exist, but in this thesis I will be focusing on their biomedical applications for drug delivery systems.

NPs are ideal drug delivery systems because their size allows them to have extensive interactions at the cellular level. Nanocarriers can be used to increase uptake of a conjugated drug into specific cells to enhance drug delivery to a specific tissue or cell type. NPs have been successfully used to deliver many different drugs including anticancer, antitubercular, anti-HIV, anti-Alzheimer, and antibiotic drugs through different conjugation mechanisms [37-42]. NPs of a therapeutic agent of interest can also be produced directly to enhance delivery and uptake. Examples for this type of NPs include antimicrobial metals and inorganic oxides. Of particular interest in this field are silver, copper, titanium dioxide, and zinc oxide [43]. For the purpose of this thesis, I will be mainly focusing on the antimicrobial properties of silver nanoparticles (AgNPs).

It has been known for centuries that metallic silver holds antimicrobial properties, and it has been used for the treatment of both chronic wounds and burns [44,45]. The use of silver in wound care even shows up in the writings of Hippocrates in 400 B.C.E. [46]. Silver is what's known as a broad spectrum antimicrobial, meaning that it is effective against many different Gram-positive and Gram-negative bacterial strains [47]. It also exhibits very low toxicity against mammalian cells, making it an excellent candidate for use in combatting MDR bacteria. Recently many products have been released to market that incorporate silver ions or AgNPs for their antimicrobial activity in a variety of different industries.

AgNPs can be produced by a variety of chemical, physical, or biological synthesis methods [48]. Chemical synthesis methods are the most commonly utilized synthesis methods because a large quantity of high quality NPs can be produced in a short amount of time. However, these synthesis methods generally employ the use of harsh chemicals. With the recent push towards 'Green Chemistry' many natural agents have been investigated for the synthesis of AgNPs. In this thesis

I will explore the use of the wood biopolymer, lignin, for its ability to act as a reducing and capping agent in the synthesis of AgNPs.

In general, AgNPs show greater antimicrobial activity than silver salts alone likely due to the high surface area to volume ratio that is intrinsic of NPs, allowing increased interactions with the surface of bacterial cells [49]. Hundreds of papers have been published showing the antimicrobial effects of AgNPs, but the majority of these papers deal exclusively with the synthesis and *in vitro* antimicrobial testing of these particles. This leaves a huge gap in the literature surrounding the *in vivo* antimicrobial effects and the biodistribution of AgNPs.

The goals of this thesis are threefold:

(1) Investigate the synthesis, characterization, and optimization of AgNPs using the natural compound lignin,

(2) Radioactively tag the AgNPs and determine their biodistribution *in vivo*, and

(3) Evaluate the antimicrobial behavior of the AgNPs both *in vitro* and *in vivo*.

The first goal of this project was to develop a synthesis method to produce stable AgNPs using a chemical synthesis method with the natural agent lignin using multiple strategies. Lignin is the most abundant aromatic polymer in the world and is a waste product of the pulp and paper industry. It has shown the capacity to cap and reduce AgNPs [50,51]. As the general procedure for producing these AgNPs requires a lengthy synthesis, a microwave-assisted synthesis method was developed to reduce processing time.

The second goal of this project was to evaluate the biodistribution of the AgNPs by radioactively tagging the lignin-capped silver nanoparticles (L-AgNPs) using ^{123}I, a common single-photon emission computed tomography (SPECT) isotope, and ^{111}Ag, a novel silver isotope which is potentially useful for SPECT imaging [52,53]. The biodistribution of the particles was examined after subcutaneous (SQ) injection and intratracheal instillation using a SPECT/CT machine.

The final goal of this project was to determine the antimicrobial properties of these L-AgNPs against both non-resistant and MDR bacteria. This project goes beyond most antimicrobial AgNP studies and examines the antimicrobial behavior of the particles against MDR bacteria both *in vitro* and *in vivo*. The *in vitro* work was done using a broth dilution method to determine the minimum inhibitory concentration (MIC) of the particles, while the *in vivo* work was done on a biofilm-forming cutaneous infection (abscess) model.

1.2 Literature Review

1.2.1 Metal Nanoparticles

In the advancement of nanotechnology aimed at developing novel antimicrobials, metal and metal oxide nanoparticles (NPs) show some of the most promising results against MDR bacteria [43,54]. NPs are generally considered to be particles with at least one dimension measuring around 1 to 100 nm [33]. When particle size is reduced below a few hundred nm, the particles begin to show unique properties which change significantly with size and differ from bulk material properties. These changes are likely due to the great increase in surface area to volume ratio that is evident when size is decreased below a micrometer, leading to high specific area and largely increased number of surface atom interactions with their surroundings [34]. For example, bulk gold appears shiny and yellow/gold in color, but gold NPs appear red at sizes less than 100 nm or purple to blue/black for larger particles. Colloidal suspensions are also possible with NPs due to enhanced surface interactions allowing suspensions to form when the materials should otherwise sink or float in a solvent. NPs can be synthesized for a wide variety of metals and metal oxides, and can be modified with functional groups allowing for further modifications with endless numbers of ligands (functional groups), targeting agents (to direct NP to specific location), drugs, or imaging agents (for diagnosis or visualization) for potential applications in many different industries [55].

1.2.1.1 Synthesis Methods

In a very broad sense, metallic NP synthesis methods can be split into two major categories: top-down and bottom-up. Top-down methods involve breaking down large bulk pieces of the metal into NPs using some external force. Examples of top-down methods include: ball milling, grinding,

and laser ablation. Laser ablation is a process in which bulk material surfaces are irradiated with a laser to induce plasma breakdown and shock-wave propagation, and has been used to produce NPs of gold, silver, copper, titanium, and silicon [56-60]. Ball milling and grinding methods rely on the impact and attrition of the grinding media against bulk metals. In most cases top-down methods are not used due to their significant energy use requirements, and inability to properly control all experimental parameters. These factors lead to poor uniformity of particles and extreme difficulty of producing very small particle sizes. However, top-down methods can be very useful if zero solvent contamination is necessary [61].

Bottom-up synthesis methods available for the production of metal NPs can be broadly characterized into methods which produce particles through gaseous phase methods or through liquid phase methods. The bottom-up synthesis method involves starting with atoms in the gaseous or liquid form, then producing oligomeric clusters, and eventually NPs from that atomic state. A synthesis method can be chosen based on the specific physical and chemical properties required for the desired NPs depending upon their application.

In gaseous phase methods, the production of NPs is generally achieved through vapor deposition. The chemical vapor deposition (CVD) method utilizes a chemical reaction occurring in the gaseous phase at various pressures, and generally requires very high heat (>500°C) [62]. This process also requires very precise control of reaction parameters to produce NPs, and can be performed using a chemical flame, plasma process, laser, or electric furnace to pass hot gas through a reaction chamber [61,63]. The physical vapor deposition (PVD) method utilizes the rapid cooling of a gas phase material, usually in a vacuum chamber. The solid or liquid source material is first evaporated into the gas phase and then quickly cooled into the solid phase to produce NPs. This method is generally used to produce coatings for materials through common PVD processes like sputtering and evaporation for thin-film deposition.

1.2.1.1.1 Liquid Phase Synthesis Methods

The most studied NP preparation methods, by far, are liquid phase methods because large quantities of NPs can be produced for low cost using readily available laboratory equipment. These systems can produce very tailored particles through precise control of temperature, pH, mixing speed, reaction time, chemical concentration, and other reaction parameters. These methods begin with a source of metal ions (generally a metal salt) which is converted into NPs through some chemical process. In chemical reduction, the ions are reduced to their zero oxidation state (i.e. $M_n^+ \rightarrow M_n^0$) using a chemical reduction agent [64]. The production of the zero oxidation state of the metal or metal oxide presents a nucleation site for NPs to grow by adding metal atoms to the surface of the NP being formed to produce oligomeric clusters [65-67]. Eventually the particles must be stabilized to prevent aggregation, this can be accomplished through electrostatic repulsion or steric hindrance [68]. Other liquid phase methods include photoreduction, electrochemical reduction, microwave-assisted synthesis, sedimentation methods (e.g., co-precipitation and sol-gel), and biological based methods [61,68].

Chemical reduction is the most utilized synthesis method for the production of metal NPs because it is the simplest and most versatile method, it generally requires readily available materials and produces very homogeneous results. For example, AgNPs are generally synthesized using a reducing agent like sodium borohydride, sodium citrate, Tollens reagent, or N-dimethylformamide (DMF) to reduce Ag^+ ions (provided from a silver salt) to Ag^0 in order to begin nucleation, and eventually NP formation [68]. The particles must also be stabilized during production to prevent sedimentation and agglomeration. This is accomplished using a molecule which can control the growth of the particle, known as a “capping agent” [69]. Many different capping agents such as surfactants, polymers, or other ligands can be used to alter the surface chemistry of the produced metal NP and to add reactive functional groups, prevent aggregation, or increase the biocompatibility of the produced particles. Current synthesis methods prefer the use of multifunctional chemical agents that can act both as a reducing and capping agent so that the entire process can be completed in one step.

1.2.1.1.2 Biological Methods

Typical chemical methods of NP production utilize harsh or non-environmentally friendly chemicals as reducing and capping agents, so the development of natural NP synthesis methods has been a large topic of interest. Biological approaches for the synthesis of metal NPs have been significantly investigated for their eco-friendly nature and low cost. Many different types of biological methods have been utilized for the production of NPs including bacterial strains, fungi, algae, and plants [70-75]. These methods can be considered 'Green Synthesis' routes based on their selections of reducing agent, solvent, and capping agent used to produce the desired NPs [76].

Living organisms have shown the capacity to synthesize NPs both intracellularly and extracellularly through a variety of different mechanisms. Bacteria have been used extensively to produce very stable AgNPs through the reduction of silver ions [77,78]. NP production of gold, platinum, palladium, magnetite, titanium, and many other metals and metal oxides can also be achieved using bacterial synthesis methods [74,79-83]. Fungi have also been used extensively due to their ability to withstand high flow rates and other harsh conditions in bioreactors [74]. Algae have been used to produce NPs as well, but with less success than fungi or bacteria [79].

Probably the most extensively studied natural production method of metal NPs has been the use of plant extracts to reduce and cap NPs. The use of plant extracts is incredibly cost effective and generally follows similar procedures as typical chemical reduction methods, but without the use of harsh chemicals [73]. These methods are also environmentally friendly, can be easily scaled up, and don't require the use of high temperature, pressure, or toxic chemicals [84]. Green tea and black tea extracts have been used as reducing and capping agents for the production of gold and AgNPs with impressive results [85,86]. Particles have also been synthesized from extracts of flowers, fruits, leaves, and wood extracts with varying success [50,87-92].

1.2.1.1.3 Microwave-Assisted Synthesis

Microwave-assisted synthesis of metal NPs is an important topic in NP synthesis discussions due to the ability to significantly increase reaction rates. The use of microwaves to expedite chemical reactions has been widely explored, and is beginning to be applied to the production of NPs.

Microwave radiation is considered to be electromagnetic radiation with a wavelength between 300 MHz and 300 GHz [93]. The uses of microwaves are broadly grouped into heating and power uses and communication uses. The microwave heating effect occurs due to dipolar polarization and ionic conduction. When microwave radiation is applied to a NP production system the dipoles (solvent molecules) and the ions align with each other in the applied electric field. When the field oscillates the dipoles and ions try to align with the electric field and lose energy in the form of heat through molecular friction and dielectric loss [94-96].

There are many advantages to using a microwave-assisted synthesis method over a conventional heating method. In general, the reaction kinetics are increased one or two orders of magnitude when using a microwave-assisted system, and the initial heating step is significantly faster which means less overall energy is used [97]. NPs can thus be produced significantly faster with less overall energy usage when using a microwave-assisted synthesis versus a conventional heating method. Additionally, microwaves provide much more uniform and rapid heating than conventional methods. Conditions can also be easily controlled allowing temperatures over 100°C with higher pressures, and many potential temperature profiles can be utilized to produce large quantities of very uniform NPs [98].

1.2.1.2 Stabilization

When producing particles in the nanoscale range surface properties must be precisely controlled to ensure that they do not become significantly larger particles due to agglomeration. NPs possess a large surface area to volume ratio which provides a significant reactive area between the surface and the surrounding. This is what differentiates NPs from their bulk material counterparts and gives them their unique properties, but it also often forces them to agglomerate into larger clusters (agglomerates) or larger particles (aggregates) to minimize total surface energy of the system [99]. Due to Brownian motion, gravity, and other forces, particles are constantly colliding with each other and can agglomerate if steps are not taken to counteract the attractive forces between particles. The force that causes these NPs to agglomerate is the attractive van der Waals force [100]. This force can be overcome through electrostatic or steric stabilization, or by placing the particles into an ionic liquid.

Electrostatic stabilization overcomes the attractive van der Waals forces through repulsive Coulomb forces between charged particles [101]. When solids are brought into contact with a polar solvent they gain a surface electrical charge through preferential adsorption of ions, dissociation of surface charged species, substitution of ions, accumulation or depletion of electrons at the surface, or physical adsorption of charged species at the particle surface. In order to maintain electroneutrality, counter-ions of an opposite charge must accumulate around the formed particle. This accumulation of charge causes an unequal distribution in charge between the surface of the solid particle and the solvent. The layer of the dispersed phase around the charged particle is known as the electrical double layer, and consists of three main parts: the charged surface, the Stern layer, and the diffuse layer. These three parts can be seen in Figure 1 in addition to the corresponding electrical potential in each part.

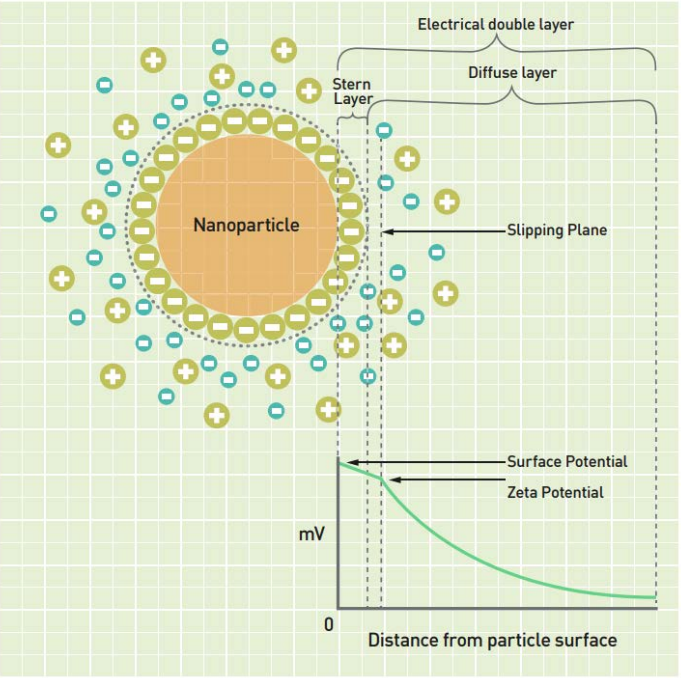

Figure 1: Electric double layer charge representation and corresponding electrical potential as function of distance from surface, figure included with permission from the copyright holder [102]

The charged surface consists mainly of charged ions which have been adsorbed on the surface of the particle. These ions are generally negative and account for the surface potential. The area between the surface of the solid and the diffuse layer is called the Stern layer. The Stern layer is a tightly bound layer of solvent and counter-ions where electric potential drops linearly [103]. Past

the Stern layer is the diffuse layer which consists of a film of solvent containing counter-ions in higher concentration, which diffuse freely, and that decrease in concentration until reaching the average concentration in the solvent. As the particle moves through the solvent a layer of the solvent attached to the particle moves with it. The boundary of this layer is found in the diffuse layer and is called the slipping plane. The electrical potential at the slipping plane relative to a point in the bulk fluid is called the zeta potential.

The zeta potential is widely used as a quantification of charge, but it is not equal to the Stern potential or the surface potential [104]. Zeta potential is generally used as a significant measure of the stability of NPs because the magnitude of the charge is directly proportional to the electrostatic repulsion of like charges. The higher the magnitude of the zeta potential, the more stable the colloidal solution will be and the less likely that the particles will interact and aggregate. In general, moderate stability is characterized by a zeta potential from ±30 to ±40 mV, good stability from ±40 to ±60 mV, and excellent stability at more than ±61 mV [105].

The other major form of particle stabilization is polymeric (or steric) stabilization. There are two main methods of polymeric stabilization: steric stabilization and depletion stabilization. Steric stabilization simply works by adsorbing or grafting macromolecules onto the surface of a particle. Adsorbing or grafting macromolecules onto the surface of a particle creates a coating which provides enough repulsive force to overcome van der Waals attractive forces [106]. Depletion stabilization utilizes macromolecules as well, but in this case they are free in solution. It is also possible to use a combination of both steric stabilization and depletion stabilization to prevent agglomeration.

1.2.2 Silver Nanoparticles and Ions

Antimicrobial activity has been demonstrated using NPs of Ag, MgO, TiO_2, ZnO, CuO, Au, Fe_2O_3, Al_2O_3, Bi, and NiO [107-114]. However, the most effective and widely used antimicrobial metal NP is silver [43]. Ag NPs have shown excellent antimicrobial behavior against a wide variety of Gram-negative and Gram-positive bacterial strains, including MDR strains [115]. Silver has long been used as an antimicrobial to purify drinking water and in the treatment of burns and chronic

wounds with high efficiency and low toxicity [47]. There are many commercially available products that incorporate silver as an antimicrobial, ranging from toothpaste to textiles and urinary catheters to hospital stretchers [49,116-119].

Metallic silver, AgNPs, and soluble silver salts are known to continuously release silver ions which act as an antimicrobial agent [120]. In bulk silver, this release happens quite slowly due to the low surface area to volume ratio, but in NPs this process is expedited and the antimicrobial effect is significantly increased. This has led to silver being used as a widespread antimicrobial agent against bacteria, fungi, and viruses [45]. Due to widely increased production of AgNPs there has been a recent push towards green synthesis routes which utilize naturally derived compounds to both reduce and cap AgNPs.

Table 1: Table of antimicrobial activity of AgNPs produced using natural compounds reported as MIC values

Organism	Particle Diameter (nm)	Functionalization	MIC (µg mL^{-1})	Source
***Bacillus subtilis* ATCC 6633**	6.5 – 43.8	Not reported (Biological)	6.25	[121]
Escherichia coli	44 – 64	*Iresine herbstii* leaf extract	6.25	[122]
Escherichia coli	20 – 30	*Acalypha indica* leaf extract	10	[123]
Escherichia coli	6 – 8	Chitosan	10	[124]
Escherichia coli	20 – 90	Green tea extract	>50.0	[125]
Escherichia coli	8.9	*Paederia foetida* leaf extract	6.293	[126]
***Escherichia coli* ATCC 117**	6.5 – 43.8	Not reported (Biological)	6.25	[121]
***Escherichia coli* ATCC-39403**	28	*Withania somnifera* leaf extract	1.8±0.20	[127]
***Escherichia coli* CCM 3954**	44	Glucose	27	[128]
***Escherichia coli* CCM 3954**	25	Maltose	3.38	[128]
***Escherichia coli* CCM 3954**	35	Lactose	27	[128]
***Escherichia coli strain* (BL 21)**	31 - 40	*Cinnamon zeylanicum* bark extract	50	[129]
Klebsiella pneumoniae	44 – 64	*Iresine herbstii* leaf extract	50	[122]
Pseudomonas aeruginosa	44	Glucose	13.5	[128]
Pseudomonas aeruginosa	50	Galactose	27	[128]
Pseudomonas aeruginosa	25	Maltose	3.38	[128]
Pseudomonas aeruginosa	35	Lactose	13.5	[128]
Pseudomonas aeruginosa	44 – 64	*Iresine herbstii* leaf extract	12.5	[122]

Organism	Particle Diameter (nm)	Functionalization	MIC (μg mL^{-1})	Source
Staphylococcus aureus	44 – 64	*Iresine herbstii* leaf extract	12.5	[122]
Staphylococcus aureus	8.9	*Paederia foetida* leaf extract	4.454	[126]
Staphylococcus aureus	6 – 8	Chitosan	10	[124]
***Staphylococcus aureus* ATCC 6538**	6.5 – 43.8	Not reported (Biological)	12.5	[121]
***Staphylococcus aureus* ATCC-25923**	28	*Withania somnifera* leaf extract	1.2±0.14	[127]
***Staphylococcus aureus* CCM 3953**	44	Glucose	6.75	[128]
***Staphylococcus aureus* CCM 3953**	50	Galactose	54	[128]
***Staphylococcus aureus* CCM 3953**	25	Maltose	6.75	[128]
***Staphylococcus aureus* CCM 3953**	35	Lactose	6.75	[128]
***Staphylococcus aureus* MRSA**	44	Glucose	27	[128]
***Staphylococcus aureus* MRSA**	50	Galactose	54	[128]
***Staphylococcus aureus* MRSA**	25	Maltose	6.75	[128]
***Staphylococcus aureus* MRSA**	35	Lactose	27	[128]
Vibrio cholerae	20 – 30	*Acalypha indica* leaf extract	10	[123]

In Table 1 the minimum inhibitory concentrations (MICs) can be seen for AgNPs produced utilizing green synthesis routes. A comprehensive list of the antibacterial activity of a wide range of metal and metal oxide NPs produced without utilizing green synthesis routes can be found in the review published by Slavin et al. [43]. An overwhelming amount of literature exists showing the synthesis and antimicrobial effectivity of AgNPs *in vitro* against a wide range of both Gram-positive and Gram-negative bacterial strains. It has also been shown that AgNPs show a synergistic effect when combined with antibiotics like penicillin G, amoxicillin, erythromycin, clindamycin, vancomycin, and gentamicin [130,131]. AgNP antimicrobial effects are difficult to directly compare because exact size and morphology of the particles differ significantly between different production mechanisms. Additionally, there is also no real standard for antimicrobial testing conditions, bacterial strains, or choice of media which further complicates the issue. However, it is clear that AgNPs are very effective as a broad-spectrum antimicrobial agent at low concentrations, and can be produced using green synthesis techniques.

1.2.2.1 Antimicrobial Mechanisms of Action

The exact mechanism by which AgNPs exert antimicrobial action is currently a much debated topic, and it is suggested that there are multiple different mechanisms by which AgNPs are toxic to microbes. However, most authors are in agreement that the presence of the positively charge silver ion (Ag^+) is required for antimicrobial activity [132]. AgNPs are known to continuously release silver ions providing a source for antimicrobial activity. The NPs themselves also possess a large surface area to volume ratio which provides more surface interactions with microbes, allowing for increased transfer of silver ions and direct antimicrobial action. It is also important to note that the presence of oxygen is required for antimicrobial action of AgNPs [133].

One of the primary mechanisms of action of AgNPs against bacteria is the direct disruption of the cell membrane and cell wall. AgNPs accumulate and form aggregates around the bacterial membrane, and can also anchor directly to the bacterial cell wall. This interaction likely occurs due to the positively charged surface of the AgNPs interacting electrostatically with the negatively charged membrane of the bacterial cells [134]. This causes direct disruption of the bacterial cell membrane causing electron dense ‘pits’ to form which leads to increased permeability and cell

death [135]. AgNPs also have a high affinity to sulfur and phosphorus which is highly abundant in the proteins on the bacterial membrane. It has been suggested that these interactions increase the penetration of AgNPs into the cell making cell membrane disruption the primary mechanism of toxicity [136]. Differences have also been shown between interactions with Gram-positive and Gram-negative bacterial species. For example, *E. coli* has shown higher sensitivity to AgNPs than *S. aureus*, which is thought to be due to differences in concentration of peptidoglycans at the bacterial cell wall and differences in cell wall thickness [137]. *S. aureus* has a much thicker cell wall and more peptidoglycan than *E. coli*, which has a cell membrane with a large amount of negatively charged lipopolysaccharides (LPS), which likely contribute to the adhesion of AgNPs [138].

The delivery of silver ions beyond the bacterial cell membrane and cell wall is another primary mechanism of action of AgNPs against bacteria. The formation of pits on the bacterial cell wall has been hypothesized to facilitate silver ion delivery to the bacterial cell. Ions have also been shown to enter through porin channels in the bacterial outer membrane, causing a variety of problems for intracellular function [139,140]. Silver ions have been shown to alter transport regulation, interact with phosphorus on DNA causing inhibition of replication, and react with sulfur-containing enzymes to cause enzyme deactivation [141-144]. Both AgNPs and silver ions have been shown to produce significant amounts of reactive oxygen species (ROS) like hydrogen peroxide (H_2O_2), superoxide anion (O_2^-), hydroxyl radical ($OH\cdot$), hypochlorus acid (HOCl), and singlet oxygen [145]. These ROS and free radicals are produced both intracellularly and extracellularly and are able to disrupt the cell membrane [146]. Cellular toxicity can occur through hyperoxidation of lipids, proteins and DNA, reduction of glutathione (GSH), modulation of ROS-metabolizing enzymes, oxidative DNA base damage, and adenosine triphosphate (ATP) depletion through inactivation of essential proteins and enzymes [147-151]. For a more in-depth analysis of the mechanisms by which AgNPs exert toxicity against microbes, excellent reviews have been published by Dakal et al. and Duran et al. [152,153]. Bacterial drug resistance mechanisms are discussed in further detail in Section 1.2.3.

1.2.2.2 Silver Nanoparticles *In Vivo*

An overwhelming amount of research has been conducted on the *in vitro* antimicrobial nature of AgNPs, but the majority of the *in vivo* research has been limited to mainly toxicological and environmental studies. The few efficacy studies which have been released involve AgNPs which are used on implantable medical devices, dental materials, and coatings for wound dressings.

There are also few biodistribution studies which have been recently released. These studies generally use inductively coupled plasma mass spectrometry (ICP-MS) or inductively coupled plasma optical emission spectrometry (ICP-OES) to quantify the accumulation of silver in each organ after sacrificing animals at specific time points and harvesting all organs individually. These methods are effective, but give very little information about how the AgNPs actually move and accumulate *in vivo* over time and do not differentiate between silver particles and silver ions. These methods are also extensively time consuming and require high numbers of animals to obtain reliable results. One study by Chrastina and Schnitzer investigated this issue by radioactively tagging AgNPs capped with poly(N-vinyl-2-pyrrolidone) using the radioisotope ^{125}I for biodistribution analysis in mice through single-photon emission computerized tomography (SPECT) imaging after intravenous (I.V.) injection [154]. AgNPs capped with polyvinylpyrrolidone (PVP) and conjugated with doxorubicin and ^{125}I were also evaluated for their theranostic effectivity in a mouse tumor model using a γ-ray scintillation counter after I.V. injection [155]. Another study conducted by Ashraf et al. radiolabeled AgNPs using ^{99m}Tc, and evaluated their biodistribution in rabbits after I.V. injection using SPECT imaging [156]. All three studies concluded that the majority of the AgNPs accumulated mainly in the liver and spleen with minimal uptake in the thyroid, lungs, and kidneys. However, the research into biodistribution of AgNPs through radioactive methods has been limited to intravenous administration despite the many other potential routes of administration which are currently being investigated.

General systemic NP clearance mechanisms occur mainly through renal clearance or clearance through the mononuclear phagocyte system (MPS) resulting in clearance through the kidneys, liver, or spleen. It is well described that when NPs are administered via I.V. injection that particles with diameters below 8 nm are cleared by the kidney, between 10 – 150 nm are cleared by the

liver, and larger than 200 nm are rapidly cleared by the spleen [157]. Additionally, the clearance through the renal system is a passive process while clearance through the MPS is an active process. This means that without any specific stealth or targeting modifications it is expected that I.V. administered NPs with diameters from 10 – 200 nm will be quickly cleared through the liver and spleen.

One other interesting method of evaluating the biodistribution of silver-loaded NPs has been the use of ^{111}Ag as a radiotracer. Aweda et al. delivered N-heterocyclic silver carbine complex (SCC), polyphosphoester-based degradable, and hydrocarbon-based non-degradable shell crosslinked knedel-like (SCK) NPs loaded with ^{111}Ag to mice through a nebulizer for direct lung delivery [53]. The biodistribution of these NPs was measured by sacrificing the animals and measuring the radioactivity of each organ using a γ counter, or by imaging using autoradiography [52,53]. These studies show great accumulation of NPs in the lungs at about 10-50 times greater amounts than in other organs. By administering particles through a nebulizer Aweda et al. circumvented the issue of particles accumulating in the liver and spleen.

AgNPs coated with PVP have also been labeled with ^{110m}Ag and delivered via oral gavage to pregnant or lactating female rats to study their accumulation in the placenta, fetus, and breast milk [158]. Melnik et al. used a γ-counter to determine that AgNPs can transfer through the placenta and enter the breast milk in significant quantities. Particles can also enter the fetus, but only at levels of 0.085 – 0.147% of the administered dose. This method is not an ideal labeling strategy due to the extremely long half-life of ^{110m}Ag of almost 250 days.

1.2.2.3 Toxicity

So far the majority of toxicity reports have indicated AgNPs as safe for human use. AgNP toxicity is greatly related to properties such as size, surface coating, stability, and chemical composition. In particular, the size-dependent toxicity of AgNPs has been shown both *in vivo* and *in vitro* where smaller particles tend to be more toxic [159,160]. AgNPs tend to accumulate in the spleen, liver, lungs, and kidneys [161,162]. They have also been shown to cross over to zebra fish embryos *in vivo*, and to cross the blood brain barrier in rats [163,164]. AgNP exposure generally occurs

through one of three major pathways: dermal, oral, or inhalation. AgNPs administered through inhalation to Sprague-Dawley rats over 28 days showed no significant health effects or related toxicity [165]. Systemic exposure after administration through inhalation has also shown to be significantly decreased relative to oral, dermal, or I.V. exposure.

Oral ingestion is the primary route of entry for silver compounds, and daily intake is estimated at 20 – 80 µg per day [166]. Oral exposure generally occurs through food products or supplements containing AgNPs, or through drinking water treated with silver [119]. In an acute oral toxicity study conducted by Kim et al., no death or significant abnormal signs were observed at a dose level of 2000 mg/kg [167]. Another acute oral toxicity test conducted by Maneewattanapinyo et al. found that oral administration of up to 5000 mg/kg AgNPs did not produce any significant toxicological effects [168]. A study by Kim et al. showed that Sprague-Dawley rats orally dosed with AgNPs for 28 days showed induction of slight liver toxicity, but no signs of any DNA damage and only at administration of more than 300 mg/kg [161]. Another study conducted by Nakkala et al. found that Wistar rats fed up to 10 mg/kg AgNPs synthesized using *Ficus religiosa* for 28 days showed slight liver toxicity on day 29, but no significant toxicological issues after a washout period of 60 days [169].

AgNPs are used extensively in wound dressings to promote wound healing and for the treatment of burns [170-172]. The main adverse effect of AgNPs is indicated as discoloration of the skin to a blue/grey color (argyria), or similar discoloration of the eyes (argyrosis) [173]. AgNP coatings for wound dressings have shown some toxicity to keratinocytes and fibroblasts *in vitro*, but show no significant toxicity effects *in vivo* and are still commercially available [170,174]. AgNPs have been shown to translocate to other organs in rats after subcutaneous (SQ) injection, but in extremely small amounts relative to the injection site and amount excreted [175].

1.2.3 Bacterial Drug Resistance

Bacteria are generally characterized as either Gram-positive or Gram-negative depending on the makeup of their cell wall. Gram-positive bacteria have a thick, single layered cell wall around 20 to 80 nm thick that consists of mostly peptidoglycan which protects the inner plasma membrane.

The cell wall contains more non-peptidoglycan accessory polymers like teichoic acids, teichuronic acids, and other polysaccharides which are covalent linked to the peptidoglycan [176]. Gram-negative bacteria have a much more complex cell wall structure than Gram-positive bacteria. The Gram-negative bacterial cell is comprised of a small peptidoglycan layer (5 to 10 nm thick) surrounded by an outer membrane (7.5 to 10 nm thick) that consists of lipopolysaccharides, proteins, and phospholipids [177]. The cytoplasmic cell membrane lies inside the small peptidoglycan cell wall, with the area between outer and inner membranes being called the periplasmic space. This periplasmic space contains a variety of binding proteins and can hold bacterial virulence factors. These differences in cell wall structure are thought to be part of the reason that Gram-positive bacteria typically show more resistance to antimicrobial NPs [141,178,179].

Microbial drug resistance can never be avoided due to the constantly evolving nature of microbes. The spread of resistance can be conceptualized broadly as a perfect example of natural selection, and the sheer number of bacteria mutating in response to antibiotic pressure can result in resistant strains developing quite quickly [180]. When antibiotics are applied to bacteria a significant amount of them are quickly killed, but due to genetic variability there will be a few remaining microbes that possess mechanisms providing resistance to the specific antibiotic in use. The antibiotic will kill off all surrounding bacteria, except for the resistant forms, which are now free to proliferate in the void created by the use of the antibiotic. To add to the complexity of the situation, bacteria can also obtain resistance from surrounding organisms.

Bacterial drug resistance can be obtained through two major pathways: (1) mobile transfer of resistance genes or (2) mutation of an existing gene or genes. Bacterial resistance genes can be transferred between bacteria of different species using mobile genetic elements (MGEs) through plasmids, transformation (acquired from naked DNA), transposons, or bacteriophages [181]. Mobile gene transfer is the most common form of acquired antimicrobial resistance. Development of mutational resistance is often costly to cell homeostasis, and is mostly maintained in direct response to the application of the antibiotic.

Widespread misuse of antibiotics has led to the propagation of bacterial drug resistance, causing a large increase in the occurrence of drug resistant bacterial infections world-wide. This problem has arisen over the past two decades with many different terms being used to describe the patterns of resistance exhibited by these bacteria. To create a standardized international terminology, a joint initiative by the European Centre for Disease Prevention and Control (ECDC) and the Centers for Disease Control and Prevention (CDC) was started to classify these patterns of resistance [182]. They have defined antimicrobial categories for which resistance is tested and organisms are broken down into multidrug-resistant (MDR), extensively drug-resistant (XDR), and pandrug-resistant (PDR) bacteria [182]. The antimicrobial categories are different for different organisms, but an example of the categories and agents for *Pseudomonas aeruginosa* can be seen in Table 2. MDR bacteria are defined as organisms which are resistant to one or more agent in three or more antimicrobial categories, XDR are resistant to one or more agent in all but 2 or fewer categories, and PDR are resistant to all antimicrobial agents [182].

Table 2: Antimicrobial categories and agents for determination of resistance profile of Pseudomonas aeruginosa [182]

Antimicrobial Category	Antimicrobial Agent
Aminoglycosides	Gentamicin
	Tobramycin
	Amikacin
	Netilmicin
Antipseudomonal carbapenems	Imipenem
	Meropenem
	Doripenem
Antipseudomonal cephalosporins	Ceftazidime
	Cefepime
Antipseudomonal fluoroquinolones	Ciprofloxacin
	Levofloxacin
Antipseudomonal penicillins + β-lactamase inhibitors	Ticarcillin-clavulanic acid
	Piperacillin-tazobactam
Monobactams	Aztreonam

Antimicrobial Category	Antimicrobial Agent
Phosphonic acids	Fosfomycin
Polymyxins	Colistin
	Polymyxin B

Bacterial resistance to a single class of antimicrobial can develop through multiple different biochemical pathways, all of which can be present in a single bacterial strain. For example, resistance to β-lactam antibiotics can be achieved through production of β-lactamase enzymes which degrade β-lactams, reduction of access to penicillin-binding proteins (PBPs), or production of PBPs with very low binding affinity for β-lactams [183]. The use of novel antibiotics on already-resistant microbes can lead to the development of MDR, providing additive resistance through multiple pathways. The most common pathways by which microbes are resistant to antibiotics include direct modifications to the antibiotic drug, decreased uptake of antibiotic, increase of cellular efflux pump, and modification to antibiotic target site [184].

1.2.3.1 Minimum Inhibitory Concentration and Minimum Bactericidal Concentration

A major concern in the use of AgNPs as an antimicrobial agent is the development of bacterial resistance to them. Bacterial resistance to silver ions has been reported in sectors where silver is continuously used such as hospital burn units, sewage sludge, and the soil around silver mines [185-187]. The plasmid pMG101 has been identified as a silver resistance plasmid which can also confer resistance to mercury ions, although this plasmid is only found in soils contaminated with heavy metals and not associated with pathogenesis [186]. It is likely that the mechanism of silver resistance occurs through upregulated efflux pumps of silver ions and a deficiency of major porin channels all leading to the decreased accumulation of silver ions inside the cell [139]. It was also found that due to the porin deficiency, the resistant bacteria grew significantly slower in regular media and on rigid surfaces which was likely due to the interior colonies being starved for nutrients. AgNPs present a much more complex problem for bacteria, however, a few studies have suggested that AgNPs are not sufficient for controlling silver-resistant bacteria although these results could be due to aggregation of AgNPs [188,189]. For a more in-depth review of the genetic

mechanisms behind bacterial silver resistance, an excellent review has been published by Simon Silver [190].

The following chapter contains the synthesis and characterization of the lignin-capped silver nanoparticles (L-AgNPs). This includes the development of the simple heating and microwave-assisted synthesis methods, and the results of the characterization of the produced particles. These results include the chemical structure of the synthesized particles obtained through UV-Vis, and X-ray diffraction (XRD) analysis. Particle size is measured using dynamic light scattering (DLS) analysis and stability is determined by measuring zeta potential. The surface chemistry of the particles is determined by scanning transmission electron microscopy (STEM). A general discussion of AgNP synthesis is included with an emphasis on starting concentrations of agents and pH effects.

Chapter 4 includes the results obtained from the radioactive labeling of the L-AgNPs using ^{123}I or ^{111}Ag, and the biodistribution experiments conducted using ^{123}I. The labeling efficiency and particle characterization of the radioactive tagging experiments is presented for ^{123}I and ^{111}Ag. Biodistribution images obtained from SPECT/CT imaging are presented for SQ injection and intratracheal instillation of ^{123}I-labeled L-AgNPs. The labeling efficiencies, and biodistribution of both administration routes is discussed along with the choice of radiotracer.

In chapter 5 the antimicrobial activity of the L-AgNPs is evaluated *in vitro* and *in vivo* along with the determined toxicity. For the *in vitro* broth dilution tests, results of the MIC testing will be presented. In regard to the *in vivo* abscess model, bacterial load will be presented in addition to abscess size measurements. The *in vitro* antimicrobial effects of the particles are discussed including the differences in effect of the particles produced by a simple heating method and those produced by the microwave-assisted method. The *in vivo* activity and toxicity is also discussed.

Finally, in chapter 6 a brief summary of the work is presented. This includes some general conclusions and suggestions for future work.

Chapter 2: Synthesis and Characterization of Lignin-Capped Silver Nanoparticles

Lignin is known as a cross-linked, phenolic wood polymer, and exists with one possible structure shown in Figure 2 [191]. It is a waste product of the pulp and paper industry and is the most abundant aromatic polymer in nature. Lignin has shown the capacity to reduce silver salts to AgNPs and to cap the produced NPs for enhanced stability [192]. This process has also been repeated using lignin and $CuSO_4$ to produce lignin-capped Cu_2O particles, and to produce platinum, palladium, and gold NPs [193-196]. The lignin-capped silver nanoparticles (L-AgNPs) have shown excellent antimicrobial properties, even against multidrug resistant (MDR) bacteria [197].

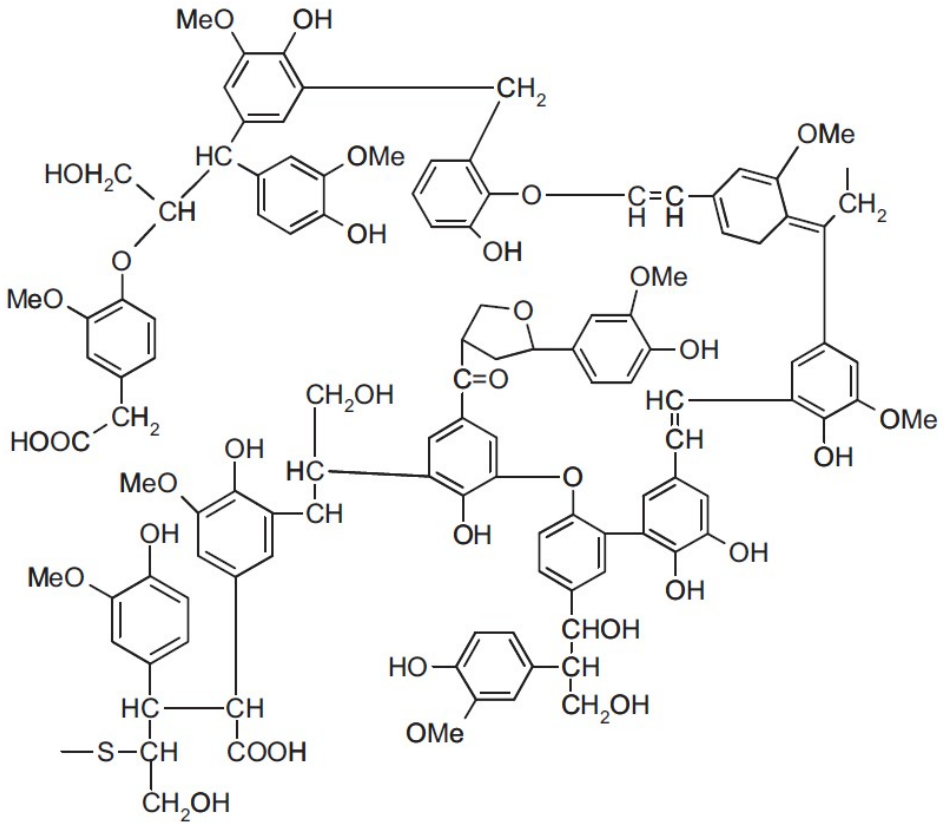

Figure 2: One possible chemical structure of lignin, included with permission from [191]

The reaction of silver salt reduction and capping with lignin requires very precise temperature and pH control. At alkaline pH the silver salts can very quickly form Ag_2O particles which provide a

surface for Ag^+ ions to adsorb onto, where they are quickly reduced in an autocatalytic reaction which produces very small particles [192,198]. Temperature also has a major impact on the reaction kinetics, leading to a much faster reaction time at higher temperatures.

2.1 Hypothesis and Objectives

L-AgNPs can be produced using a simple heating method which produces reliable results but requires a processing time of 72 hours. I hypothesize that by utilizing a microwave-assisted synthesis I can significantly decrease that processing time while maintaining particle size, chemical composition, and morphology. The particles produced using these synthesis methods will have a silver core surrounded by a coating of lignin, and all particles will be very stable in aqueous media.

This chapter contains the results of the synthesis and characterization of the L-AgNPs. This includes the development of the simple heating and microwave-assisted synthesis methods, and the characterization of the produced particles. The characterization includes the chemical structure of the synthesized particles obtained through UV-Vis and X-ray diffraction (XRD) analysis. Particle size is measured using dynamic light scattering (DLS) analysis and stability is determined by measuring zeta potential. The surface chemistry of the particles is determined by scanning transmission electron microscopy (STEM). A general discussion of AgNP synthesis is included with an emphasis on starting concentrations of agents and pH effects.

2.2 Chemical Synthesis Methods

2.2.1 Aerobic 72-Hour Heating Ag-Lignin Nanoparticle Synthesis

L-AgNPs were produced in a similar method to that described by Hu et al., utilizing an aerobic 72-hour heating synthesis method [50]. For all experiments low sulfonate (~4%) content, alkali (kraft) lignin with a molecular weight of 10,000 (#471003, Sigma-Aldrich) was used. First, 30 mL of 1% lignin solution was prepared in DI water and the pH was adjusted to 5.5 using 1 M HCl and 1 M NaOH. Then 20 mL of a 2 mg/mL $AgNO_3$ solution was prepared in DI water. The two solutions were separately heated to 68°C for 10 min and then mixed together and stirred at 150

rpm in a closed vessel at 68°C for 72 h. Hydrodynamic diameter and zeta potential were measured by Dynamic Light Scattering using a Malvern Zetasizer (Westborough, MA, USA). The UV-Vis absorbance of the mixture was measured using a Nanodrop ND-1000 (Thermo Scientific, Rockford, IL, USA) and checked every 24 h by mixing 20 µL of the solution with 180 µL of DI water to follow the reaction. The final product was stored in the fridge in the dark.

2.2.2 Anaerobic 72-Hour Heating Ag-Lignin Nanoparticle Synthesis

An anaerobic synthesis method was developed to determine if the absence of air in the system would produce more homogeneous L-AgNPs. For this synthesis method 30 mL of 1% lignin solution in DI water was prepared and the pH was adjusted to 5.5 using 1 M HCl and 1 M NaOH, and 20 mL of a 2 mg/mL $AgNO_3$ solution was prepared in DI water. The two solutions were purged of air by bubbling nitrogen through the system, and then separately heated to 60°C for 10 min. The solutions were then anaerobically mixed together and the mixture was stirred at 650 rpm in a closed vessel at 60°C for 72 h in an oil bath. The UV-Vis absorbance of the mixture was checked by mixing 20 µL of the solution with 180 µL of DI water to follow the reaction, and the final product was stored in the fridge in the dark.

2.2.3 Microwave-Assisted Synthesis of Ag-Lignin Nanoparticles (Varying Temperature)

While the 72-hour heating methods were simple and reliable, they were very time-intensive, so a microwave-assisted synthesis method was developed to attempt to decrease the processing time. All microwave-assisted synthesis methods were conducted in a Biotage Initiator$^+$ (Biotage Sweden AB, Uppsala, Sweden) microwave reactor. For this synthesis method 30 mL of 1% lignin solution was prepared in DI water and the pH was adjusted to 5.5 using 1 M HCl and 1 M NaOH, and 20 mL of a 2 mg/mL $AgNO_3$ solution was prepared in DI water. Rather than using the entire amount of stock solutions, 1.5 mL of the lignin solution and 1 mL of the $AgNO_3$ solution were mixed together in a 2 – 5 mL microwave vial and sealed. The mixture was then microwaved for 4 or 6 h at 60°C and 5 bar, or 10 min at 5 bar and 100°C, 105°C, 110°C, or 120°C. The UV-Vis absorbance of the mixture was checked by mixing 20 µL of the solution with 180 µL of DI water, and the final product was stored in the fridge in the dark.

2.2.4 Microwave-Assisted Synthesis of Ag-Lignin Nanoparticles (Varying Silver Concentration)

After a reliable synthesis method had been developed for the production of L-AgNPs, varying silver concentrations were investigated to determine if L-AgNPs could be produced with a greater silver content. For this synthesis method stock solutions were again produced by preparing 30 mL of 1% lignin solution in DI water with the pH adjusted to 5.5 using 1 M HCl and 1 M NaOH, and 20 mL each of $AgNO_3$ solutions in DI water were produced at concentrations of 2, 2.5, 5, 10, and 20 mg/mL $AgNO_3$. The same ratio of 1.5 mL of the lignin solution and 1 mL of the $AgNO_3$ solution were mixed together in a 2 – 5 mL microwave vial and sealed. The mixture was then microwaved for 10 min at 120°C and 5 bar. The absorbance of the mixture was checked by mixing 20 µL of the solution with 180 µL of DI water, and the final product was stored in the fridge in the dark.

2.3 Results and Discussion

2.3.1 72-Hour Heating Synthesis

This synthesis method is related to the method described by Hu et al. and was developed by Kristina Ivanova and Petya Stoyanova [50].

2.3.1.1 Ultraviolet-Visible Spectroscopy Analysis

Ultraviolet-visible spectroscopy (UV-Vis) is a common tool for the characterization of synthesized AgNPs that can be used to confirm their synthesis and stability [199]. It functions on the principle of exciting molecules using light in the ultraviolet and visible range, then recording the absorption of light over that range. This method is a very quick and reliable technique that can be used to characterize colloidal suspensions.

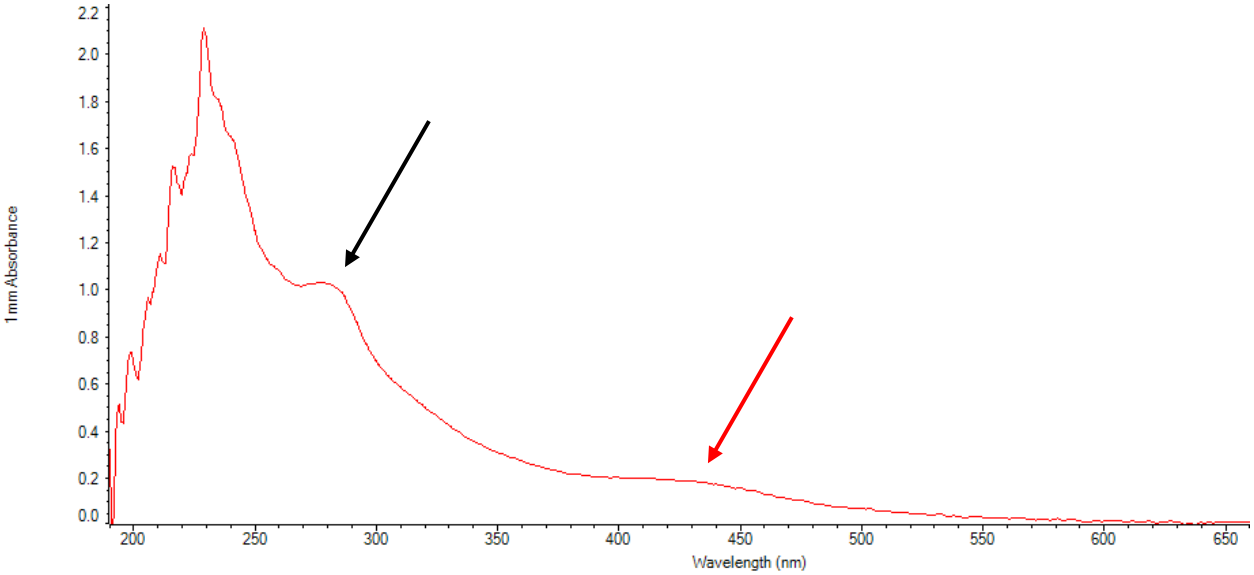

Figure 3: UV-Vis analysis of L-AgNPs produced by 72-hour heating aerobic synthesis, batch 019 showing peak around 280 nm due to lignin (black arrow) and peak around 420 nm due to AgNPs (red arrow)

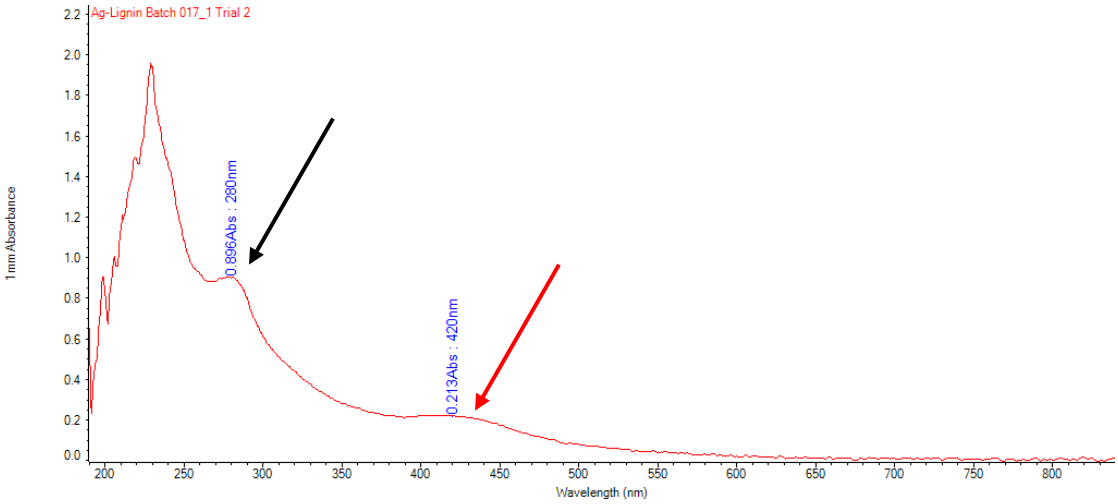

Figure 4: UV-Vis analysis of L-AgNPs produced by 72-hour heating anaerobic synthesis, batch 017 showing peak around 280 nm due to lignin (black arrow) and peak around 420 nm due to AgNPs (red arrow)

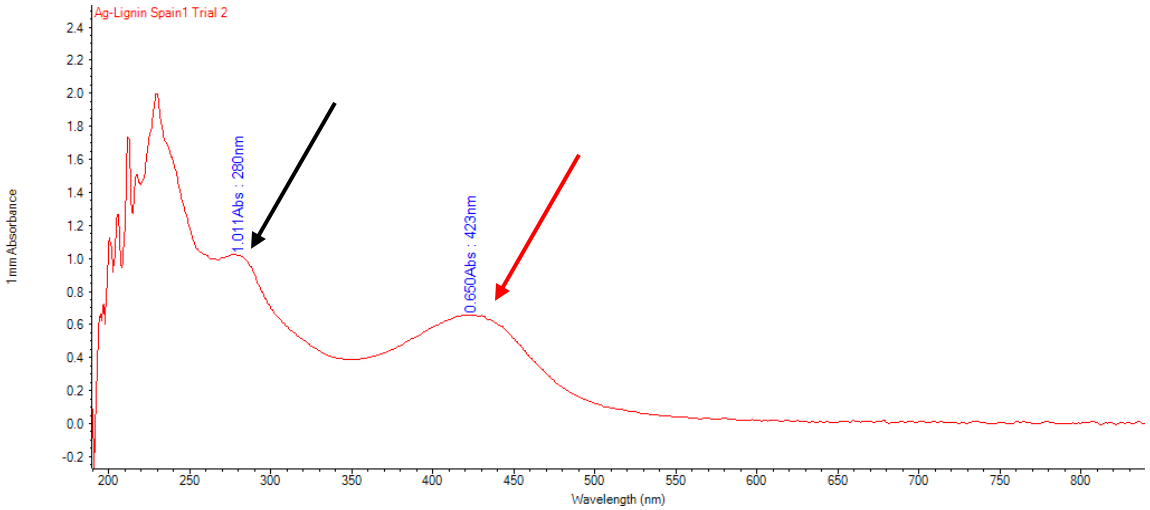

Figure 5: UV-Vis analysis of L-AgNPs produced without pH modification showing peak around 280 nm due to lignin (black arrow) and peak around 420 nm due to AgNPs (red arrow)

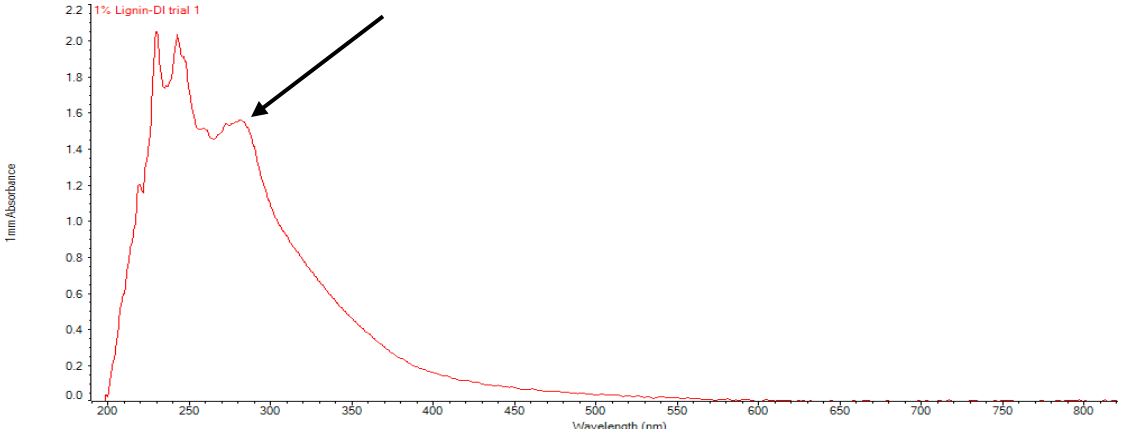

Figure 6: UV-Vis analysis of 1% lignin in DI water showing peak around 280 nm due to lignin (black arrow)

The UV-Vis analyses in Figure 3 and Figure 4 clearly show a peak around 420 nm (red arrow) which signifies AgNP formation because it is in the range of the characteristic surface plasmon resonance of metallic silver due to the oscillation of the free electrons in resonance with the frequency of the light wave [200]. Based on the UV-Vis analysis I can conclude that AgNPs can be produced using the 72-hour heating synthesis method under either aerobic or anaerobic conditions. It is also clear from Figure 5 that decreasing the pH of the lignin solution to 5.5 before particle synthesis is not necessary for production of NPs as there is still a visible peak around 420 nm signifying successful AgNP production. The peak around 280 nm (black arrow) is likely caused by the aromatic bonds in the structure of the lignin. The control UV-Vis spectrum of lignin (Figure 6) shows the presence of the same peak without the addition of $AgNO_3$. Additionally, no peak

around 420 nm is observed with lignin alone, which further confirms the synthesis of AgNPs in the 72-hour heating synthesis method.

2.3.1.2 X-Ray Diffraction Analysis

X-ray diffraction (XRD) analysis is a general crystallography technique that is used to determine that atomic and molecular structure of a given sample. It is a very useful technique for determining the chemical makeup of a crystal formed by a metal, salt, mineral, or any other molecule. This technique determines the structure of a crystal by measuring how it scatters X-ray radiation [201]. The produced L-AgNPs were lyophilized overnight to produce a powder for XRD analysis which was performed on a Bruker D8-Advance X-ray diffractometer in Bragg-Brentano configuration and equipped with a LynxEye silicon strip detector. A copper source was used with a nickel filter, the generator was set to 40 kV and 40 mA, and slit sizes were 1.0 mm (divergence), 8.0 mm (anti-scatter), and 2.5° (soller).

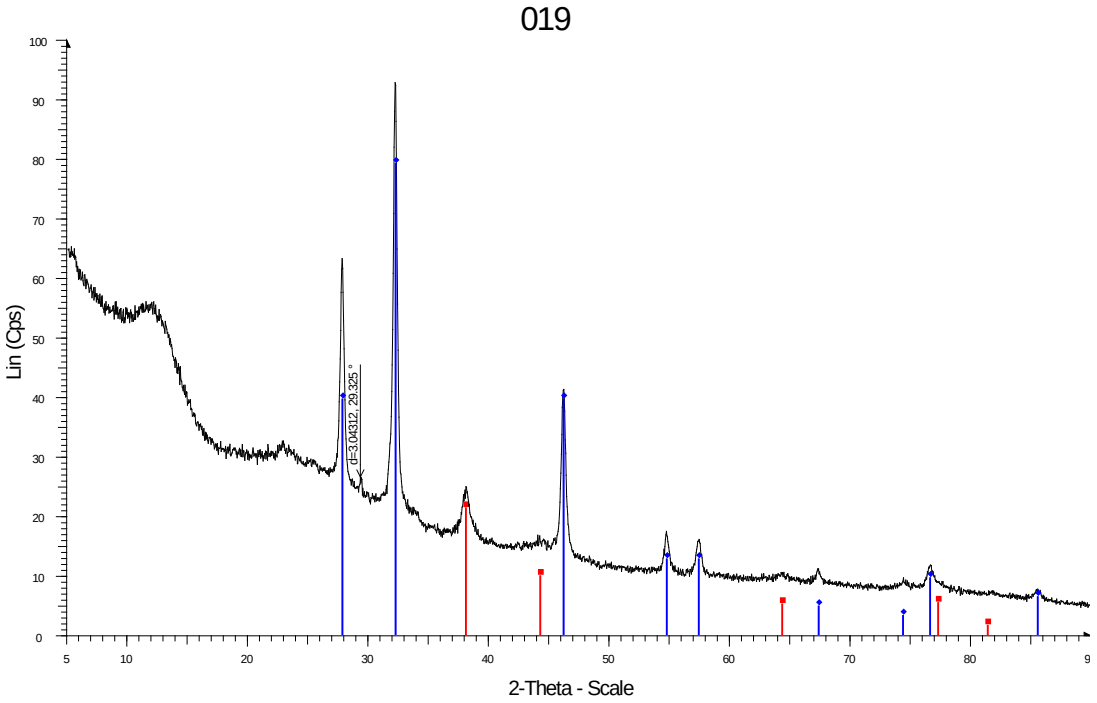

Figure 7: XRD analysis of L-AgNPs produced by 72-hour heating aerobic synthesis, batch 019 (blue line corresponds to AgCl and red line corresponds to Ag0)

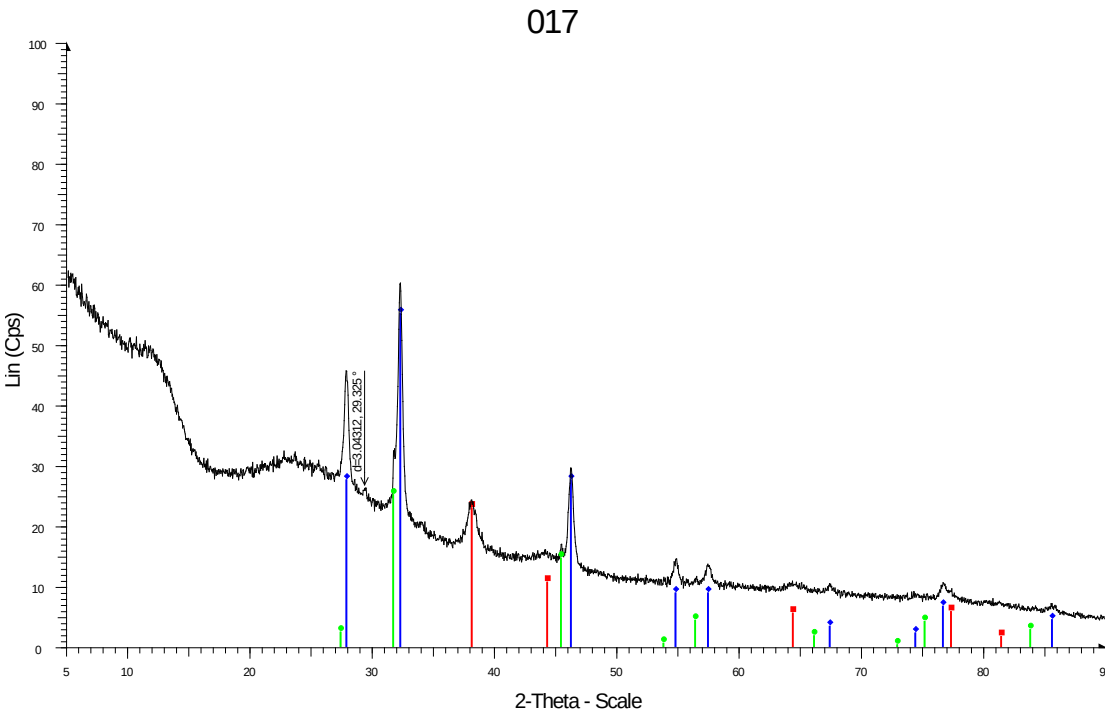

Figure 8: XRD analysis of L-AgNPs produced by 72-hour heating anaerobic synthesis, batch 017 (blue/green lines corresponds to AgCl and red line corresponds to Ag^0)

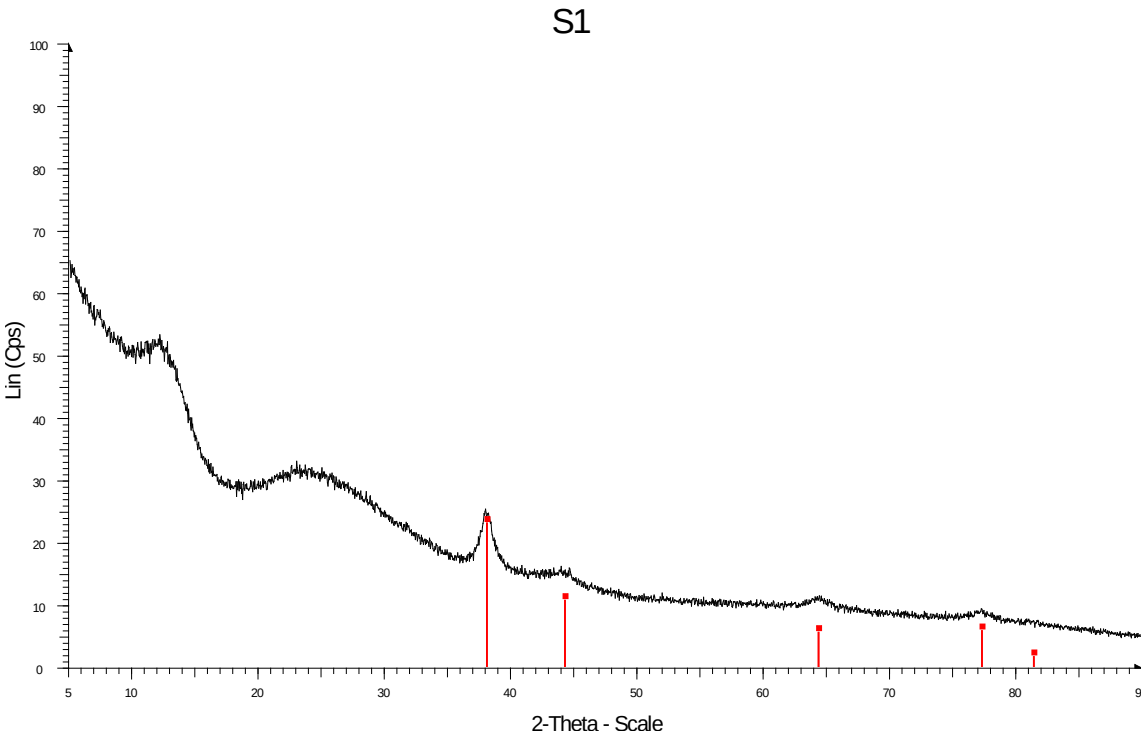

Figure 9: XRD analysis of first L-AgNP batch produced by 72-hour heating aerobic synthesis without decreasing lignin pH to 5.5 (red line corresponds to Ag0)

From the XRD analysis it is clear that the produced particles are crystalline in form and all contain crystalline Ag^0. The presence of 2-Theta peaks around 28, 32, 46, 55, 57, and 77 degrees matches the standard XRD pattern of crystalline AgCl and can be seen in to Figure 7 and Figure 8 (produced at lignin pH=5.5), but are absent in Figure 9 (lignin pH not decreased). The particles produced with a lower pH using HCl produces some crystalline AgCl salts under both aerobic and anaerobic conditions. Without any pH modification only crystalline Ag^0 is produced. It appears that significantly more AgCl is produced under aerobic conditions, while relative amounts of Ag^0 seem to be constant under both aerobic and anaerobic conditions. AgCl particles show an UV-Vis peak around 250 nm so it is likely that the presence of the lignin (peak at 280 nm) obscured the UV-Vis peak for the AgCl particles.

It is seldom discussed in the literature, but the presence of AgCl NPs in biogenically produced AgNPs is quite common, and has been discussed in one review paper published by Durán et al. [202]. They state that AgCl NPs can be produced, but when they are irradiated with UV light they are converted to Ag^0. According to their findings a significant amount of biogenically produced AgNPs contain both Ag^0 and AgCl according to the XRD analysis, but in the majority of papers only the presence of Ag^0 is discussed. They also claim that AgCl NPs are not essential for antimicrobial behavior, but they can provide an additional source of silver ions to produce enhanced antimicrobial effects. The presence of AgCl NPs in the L-AgNPs might thus provide synergistic effects and enhance the antimicrobial activity of the particles. Further work and additional controls might, however, be necessary in the future to determine the contribution of each silver source. For the remainder of this thesis it is assumed that the L-AgNPs contain both Ag^0 and AgCl.

2.3.1.3 Dynamic Light Scattering Analysis

Dynamic light scattering (DLS) analysis is an important technique used to determine the hydrodynamic diameter of a particle and is accurate from below a micrometer to around 1 nm. This technique is especially powerful in the range of 2 – 500 nm [203]. DLS analysis functions by measuring the scattering of laser light by a colloidal suspension as a function of time to determine the hydrodynamic diameter of the particles in suspension. Smaller particles move more rapidly

due to bombardment of solvent molecules and hence, the scattered light fluctuates more rapidly. Hydrodynamic diameter is a measure of how a particle behaves in suspension and is generally larger than the diameter of particles measured by electron microscopy, especially when the particles are metallic in nature and have a non-metallic coating. For all DLS measurement the results are reported as an intensity distribution because it is the naturally weighted distribution based on the light scattering. When the intensity distribution is converted to a number or volume distribution more weight is attributed towards smaller particle sizes which can discount any of the larger particles or aggregates that are observed.

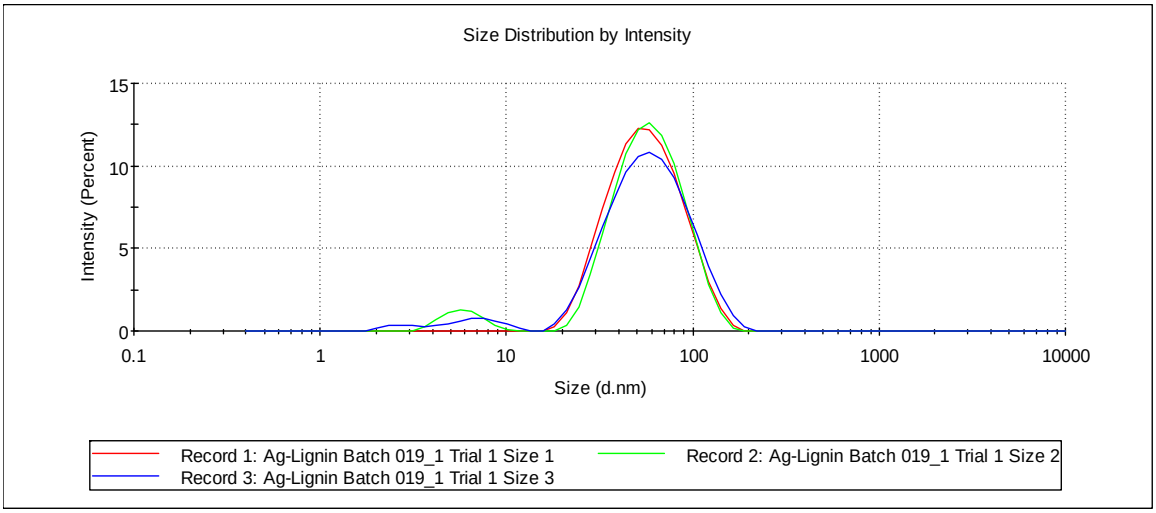

Figure 10: DLS size analysis of L-AgNPs produced by 72-hour heating aerobic synthesis, batch 019

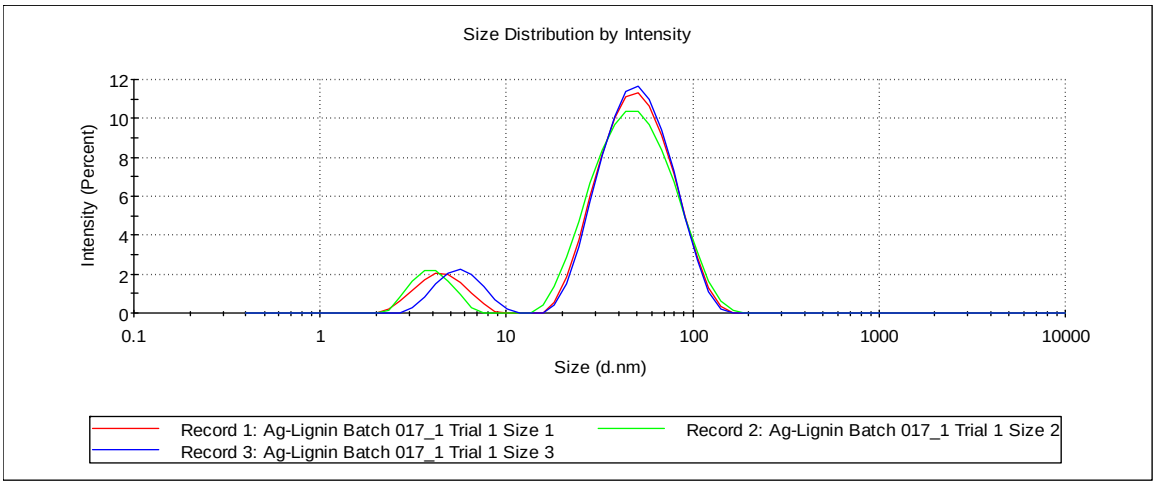

Figure 11: DLS size analysis of L-AgNPs produced by 72-hour heating anaerobic synthesis, batch 017

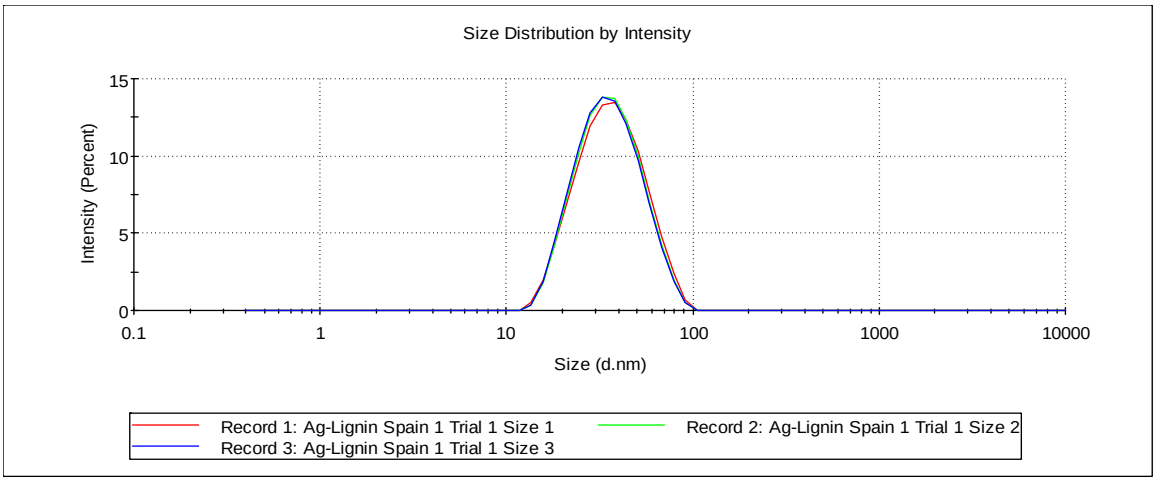

Figure 12: DLS size analysis of first L-AgNP batch produced by 72-hour heating aerobic synthesis without decreasing lignin pH to 5.5 before synthesis

In both the aerobic and anaerobic 72-hour heating synthesis methods it is clear that AgNPs are produced as one set of particles with a mean size around 6 nm and another set of particles with a mean size of around 50 nm (Figure 10 and Figure 11). This effect is significantly more pronounced when particles are produced via an anaerobic synthesis pathway. The synthesis method without any pH modification produces particles with a single mean size around 50 nm (Figure 12). The DLS size analysis confirms the presence of nano-sized particles, which corroborates the presence of AgNPs when combined with the results of the UV-Vis analysis. The particles produced at a higher pH tend to be slightly bigger than those at a lower pH. This phenomenon is likely due to the pH-related reaction kinetics. Without any pH modification, the 1% lignin solution generally has a pH of around 9. At the lower pH of 5.5 the reaction proceeds slower and produces larger particles [50]. The smaller particle formation can likely be attributed to the presence of some Ag_2O which has been described to cause a rapid, auto-catalyzed reduction of silver ions to produce very small AgNPs [198]. Additionally, this phenomenon seems to be more apparent in the anaerobic synthesis pathway than in the aerobic synthesis.

2.3.1.4 Zeta Potential Analysis

The zeta potential is an important parameter for determining the stability of a colloidal solution with the magnitude being directly proportional the electrostatic repulsion of like charges. It is measured by laser Doppler electrophoresis and phase analysis light scattering by applying an

electrical field across a sample and measuring the speed at which particles migrate towards an electrode [102].

Table 3: Zeta potential analysis for particles produced by aerobic or anaerobic 72-hour synthesis methods

	Anaerobic 017	Aerobic 019
Zeta Potential (mV)	-43.9	-48.6
Standard Deviation (mV)	1.01	2.54

Both synthesis methods produced L-AgNPs with good stability as apparent by the highly negative zeta potentials (Table 3). Such particles are expected to not aggregate or agglomerate due to their highly negative zeta potential.

2.3.1.5 Scanning Transmission Electron Microscopy (STEM) Analysis

Scanning transmission electron microscopy (STEM) is a type of transmission electron microscopy (TEM) where images are produced from electrons passing through a sample. In STEM, a very focused electron beam (0.05 – 2 nm in diameter) scans across the surface of a sample in a raster pattern to produce an image. More dense samples absorb more electrons and show up darker on the produced image. Metallic samples are easy to see in STEM because they are very dense, but organic material is very difficult to visualize so often a negative stain must be used [204]. In our work the produced particles were negatively stained with uranyl acetate which should collect around the lignin cap and provide contrast in the form of a halo around the metallic silver particles.

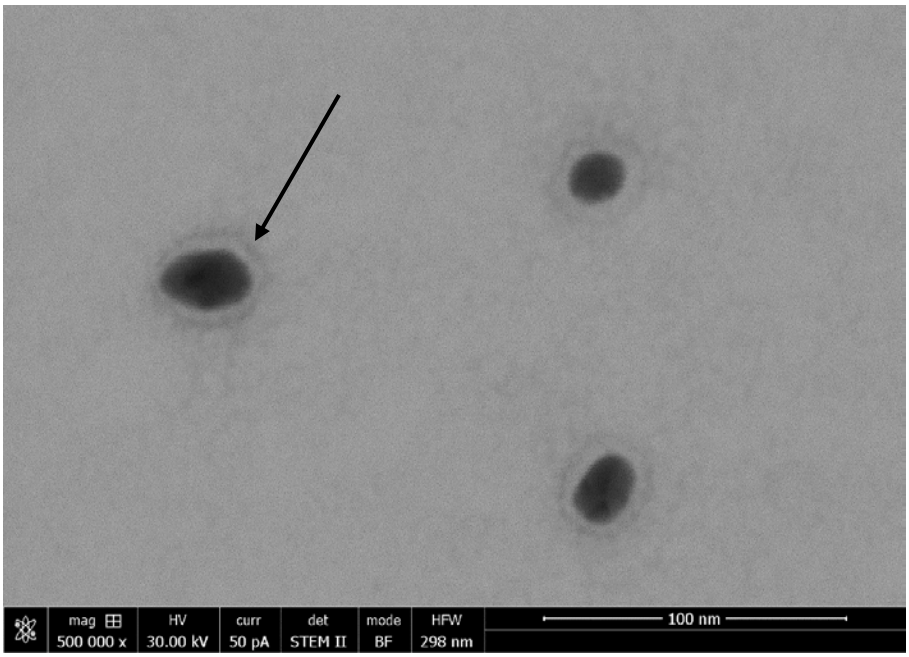

Figure 13: Negatively stained STEM image of L-AgNP batch 019 produced by 72-hour heating aerobic synthesis with pH control (500,000x magnification) showing a halo produced by negative staining of lignin (black arrow)

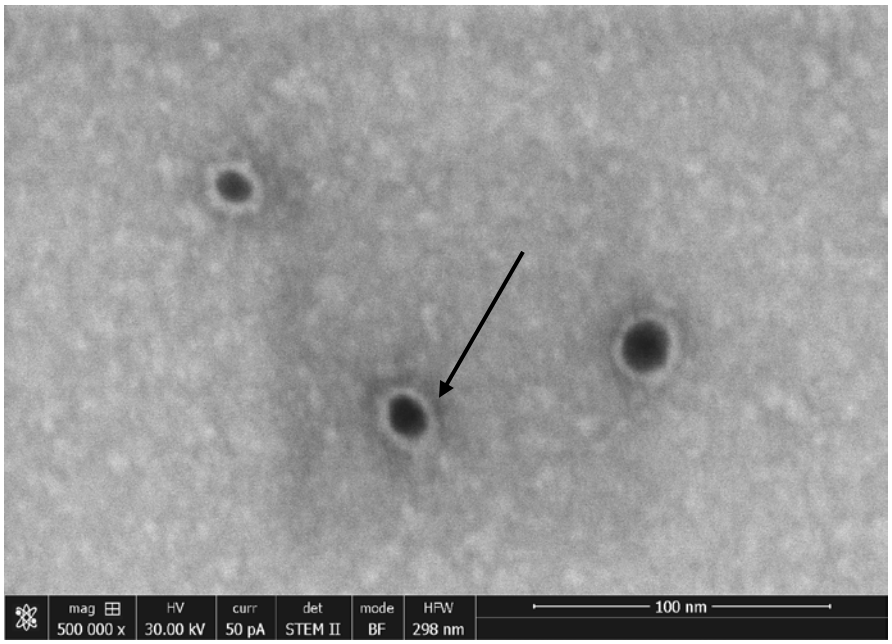

Figure 14: Negatively stained STEM image of first L-AgNP batch produced by 72-hour heating aerobic synthesis without pH control (500,000x magnification) showing a halo produced by negative staining of lignin (black arrow)

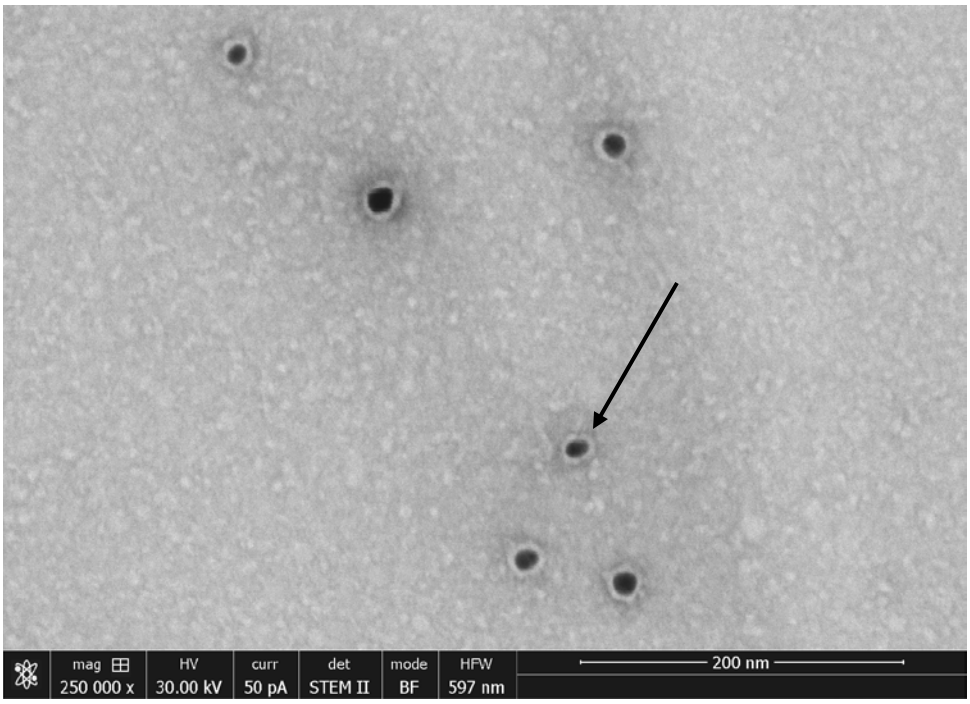

Figure 15: Negatively stained STEM image of first L-AgNP batch produced by 72-hour heating aerobic synthesis without pH control (250,000x magnification) showing a halo produced by negative staining of lignin (black arrow)

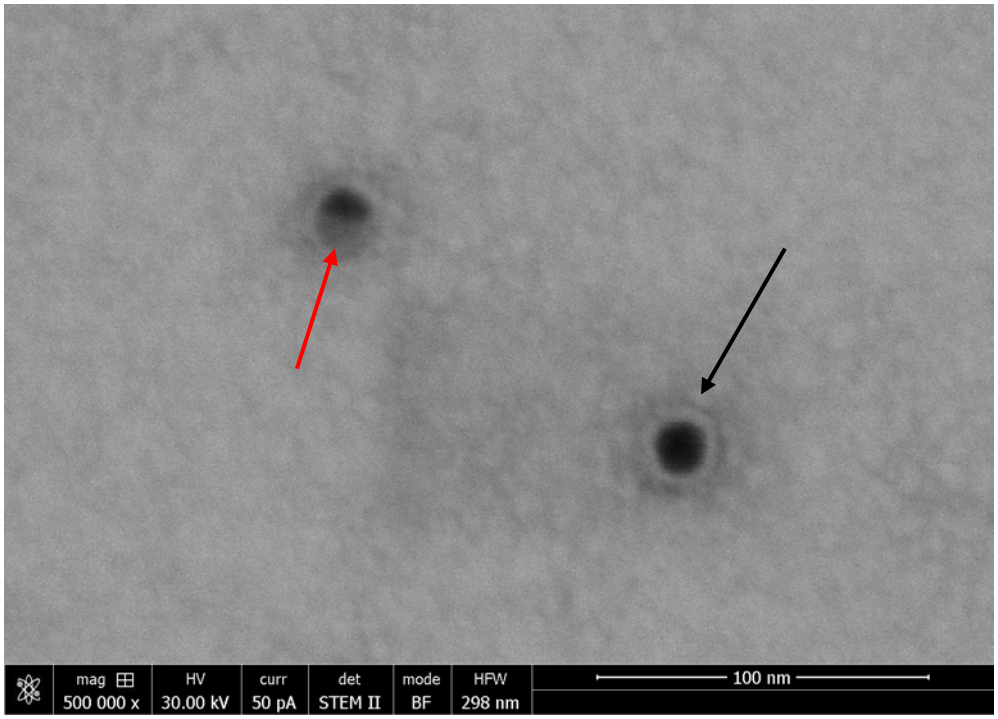

Figure 16: Negatively stained STEM image of L-AgNP batch 013 produced by 72-hour heating aerobic synthesis (500,000x magnification) showing a halo produced by negative staining of lignin (black arrow) and less dense area, potentially AgCl (red arrow)

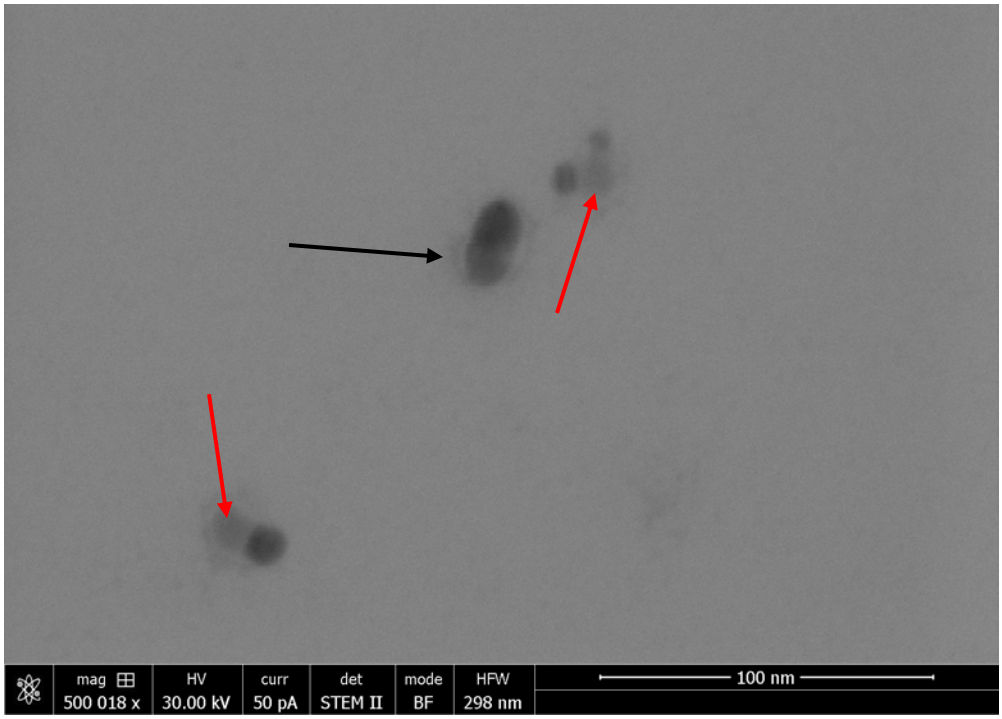

Figure 17: Negatively stained STEM image of L-AgNP batch 017 produced by 72-hour heating anaerobic synthesis (500,018x magnification) showing halos produced by negative staining of lignin (black arrow) and less dense area, potentially AgCl (red arrow)

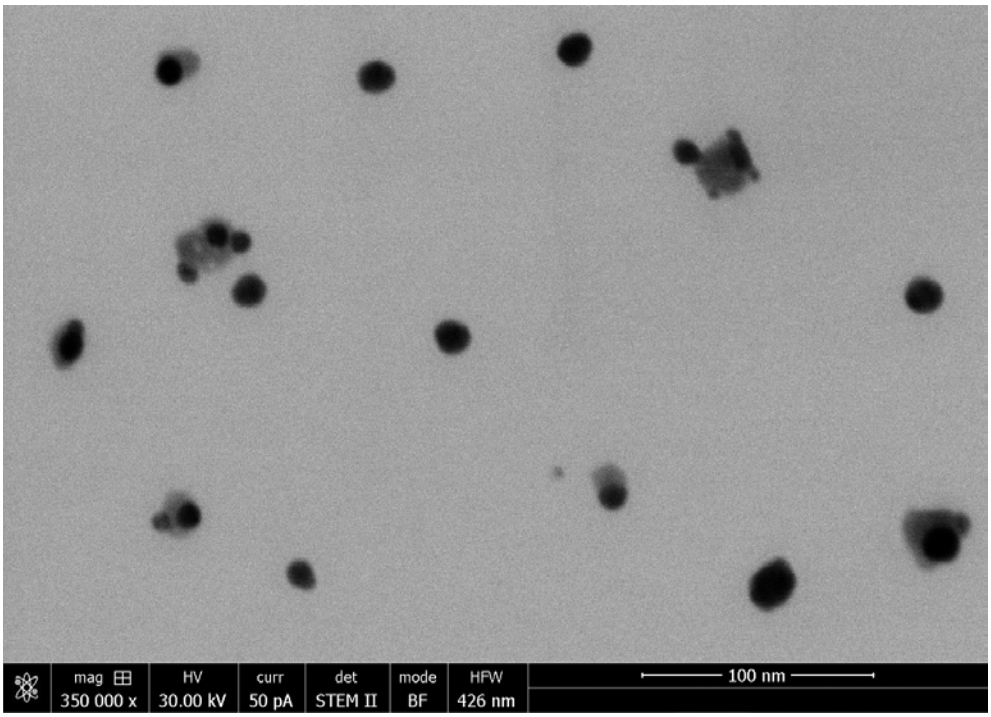

Figure 18: STEM image of L-AgNP batch 013 produced by 72-hour heating aerobic synthesis without negative staining (350,000x magnification)

The presence of very dark, dense objects in all figures indicates the formation of metallic particles in the nano-scale range. When combined with the UV-Vis and XRD analysis the NPs produced with pH modification can be assumed to contain some amounts of crystalline Ag^0 and AgCl, while the particles produced without pH modification only contain Ag^0. It is difficult to see a difference between the images of the particles produced with and without pH modification, but it is possible that some of the more lightly shaded particles (red arrows) contain the less dense AgCl while the darker particles contain the denser Ag^0.

The approximate diameter of the particles seen in the STEM images is around 20 nm which is smaller than the mean size of around 50 nm as determined by DLS analysis. This is expected because DLS analysis measures hydrodynamic diameter which is always larger than diameter measured by EM.

Negative staining with uranyl acetate produces a distinctive halo (black arrow) around the metallic core of the particle indicating the formation of an organic lignin coating (Figure 13 – Figure 17). The absence of this halo in Figure 18 where the particles have not been negatively stained with UrAc indicates that the produced halo is due to the negative staining and not some other phenomenon. Additionally, it does not appear that there are any morphological differences between the particles produced with or without pH modification. The formation of significantly smaller particles by Ag_2O in the anaerobic synthesis can be visualized in Figure 17 where it appears that the particles are agglomerates of smaller particles surrounded by a lignin coating.

The mechanism by which lignin forms a coating on the AgNPs is likely due to interactions between the charged cations on the surface of the AgNPs and the charged hydroxyl groups on lignin as well as cation-π binding between the silver ions and the aromatic structures on lignin [205]. The sulfonate groups that are added to alkali lignin to increase the solubility in water have also shown an affinity for AgNPs, so the ionic interactions between silver ions and the sulfonate groups on lignin could provide an additional mechanism for the capping of AgNPs with lignin [50].

2.3.1.6 Conclusions

The production of AgNPs by simple, 72-hour heating synthesis has been characterized with and without pH modification and under aerobic or anaerobic conditions. All synthesis methods are capable of producing AgNPs in roughly the same size range (mean diameters from 40 to 65 nm), however, there are some chemical differences between the particles produced with and without pH modification. When the starting pH of the lignin solution was decreased to 5.5 the produced particles show some amounts of AgCl formation. The conclusions that can be drawn for the remaining work are made considering that L-AgNPs contain both Ag^0 and AgCl. The particles produced by anaerobic synthesis show formation of very small sized AgNPs (confirmed by DLS) and the larger particle sizes are likely due to aggregation of smaller particles surrounded by a lignin coating (confirmed by STEM). All particles produced by the 72-hour heating synthesis methods seem long-term stable as confirmed by solidly negative zeta potential measurements. The mechanism by which lignin caps the produced AgNPs is likely through ionic interactions between negatively charged functional lignin groups and the positively charged silver ions on the surface of the AgNPs.

2.3.2 Microwave-Assisted Synthesis

A microwave-assisted synthesis method has been developed to decrease the processing time of the simple 72-hour heating synthesis method while maintaining particle size, morphology, and chemical structure. This method decreases processing time by applying elevated temperature and pressure in a more even distribution to reaction vial.

2.3.2.1 Ultraviolet-Visible Spectroscopy Analysis

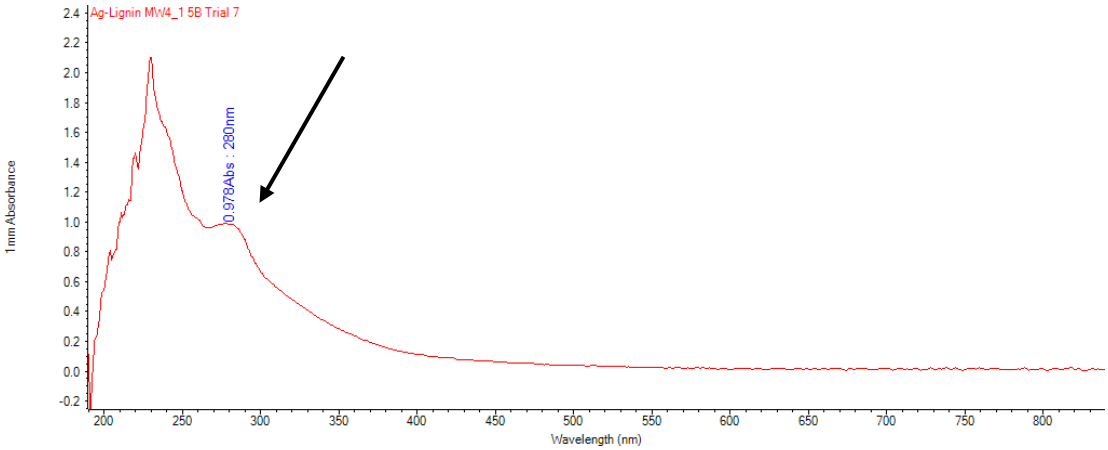

Figure 19: UV-Vis analysis of L-AgNPs produced by microwaved-assisted synthesis for 4 hours at 60°C showing peak around 280 nm due to lignin (black arrow)

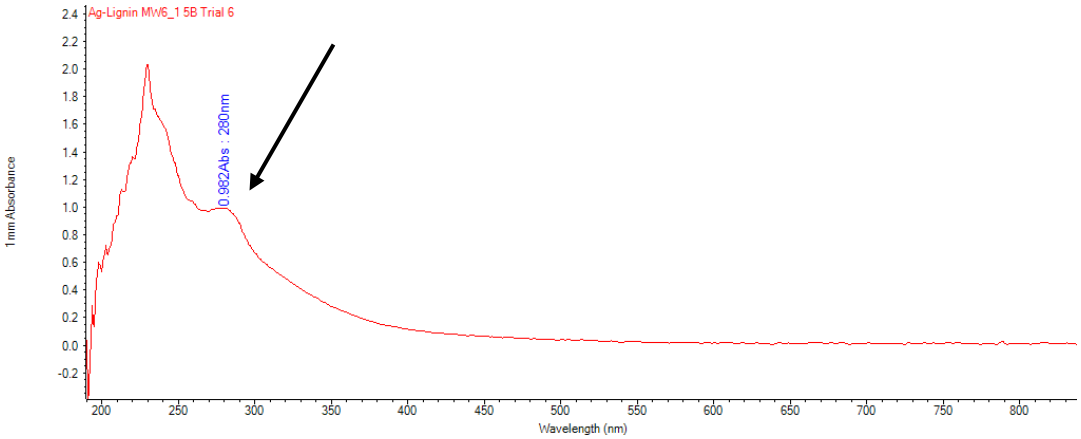

Figure 20: UV-Vis analysis of L-AgNPs produced by microwaved-assisted synthesis for 6 hours at 60°C showing peak around 280 nm due to lignin (black arrow)

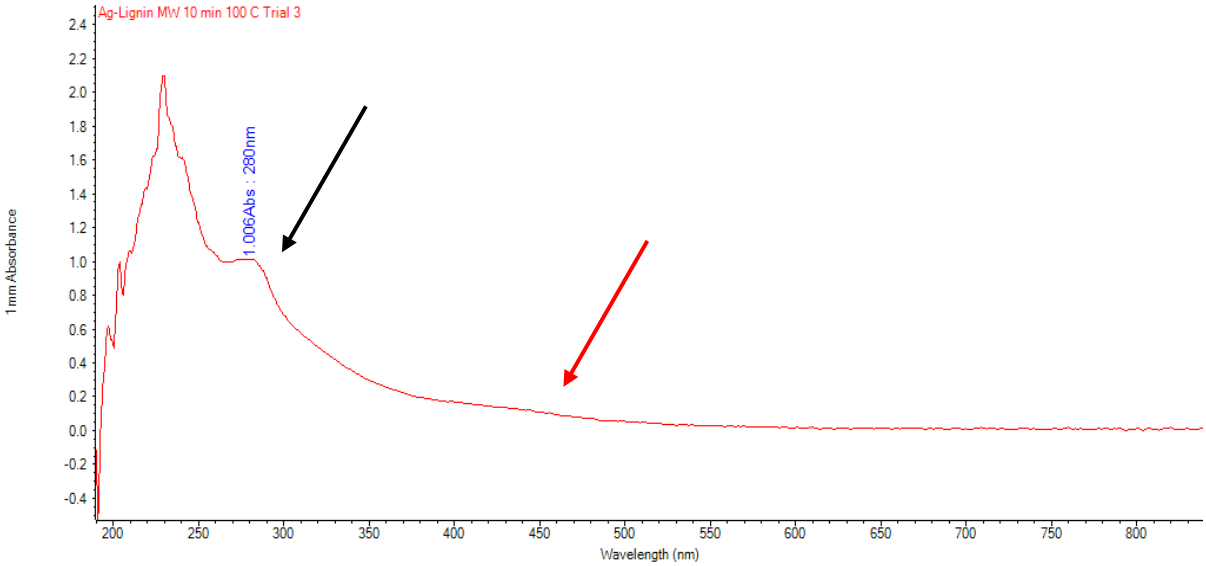

Figure 21: UV-Vis analysis of L-AgNPs produced by microwaved-assisted synthesis for 10 minutes at 100°C showing peak around 280 nm due to lignin (black arrow) and peak around 420 nm due to AgNPs (red arrow)

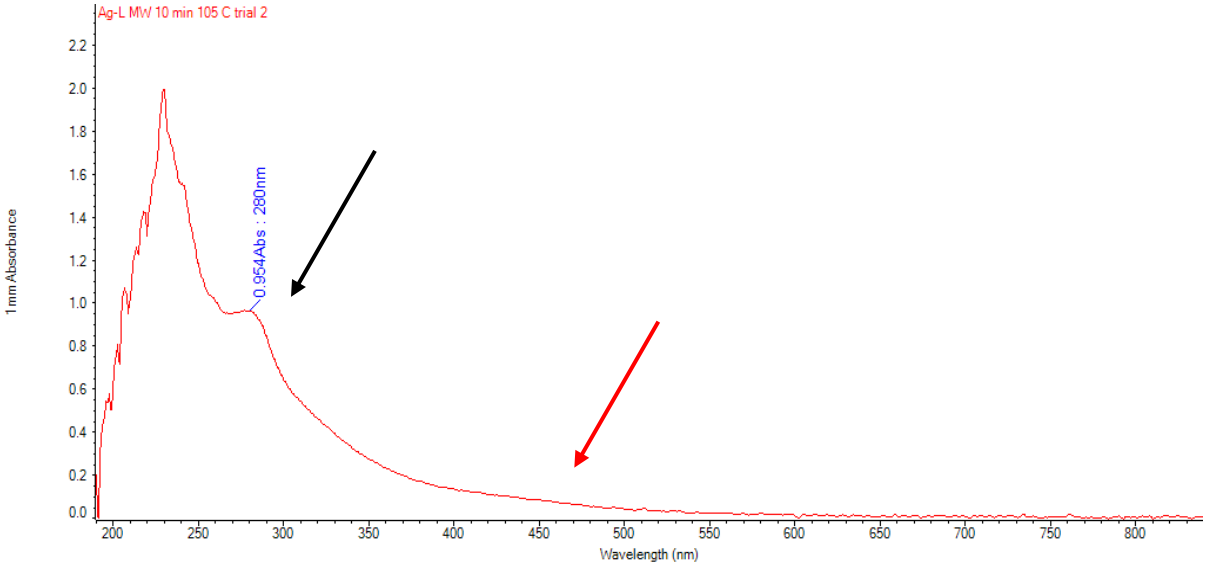

Figure 22: UV-Vis analysis of L-AgNPs produced by microwaved-assisted synthesis for 10 minutes at 105°C showing peak around 280 nm due to lignin (black arrow) and peak around 420 nm due to AgNPs (red arrow)

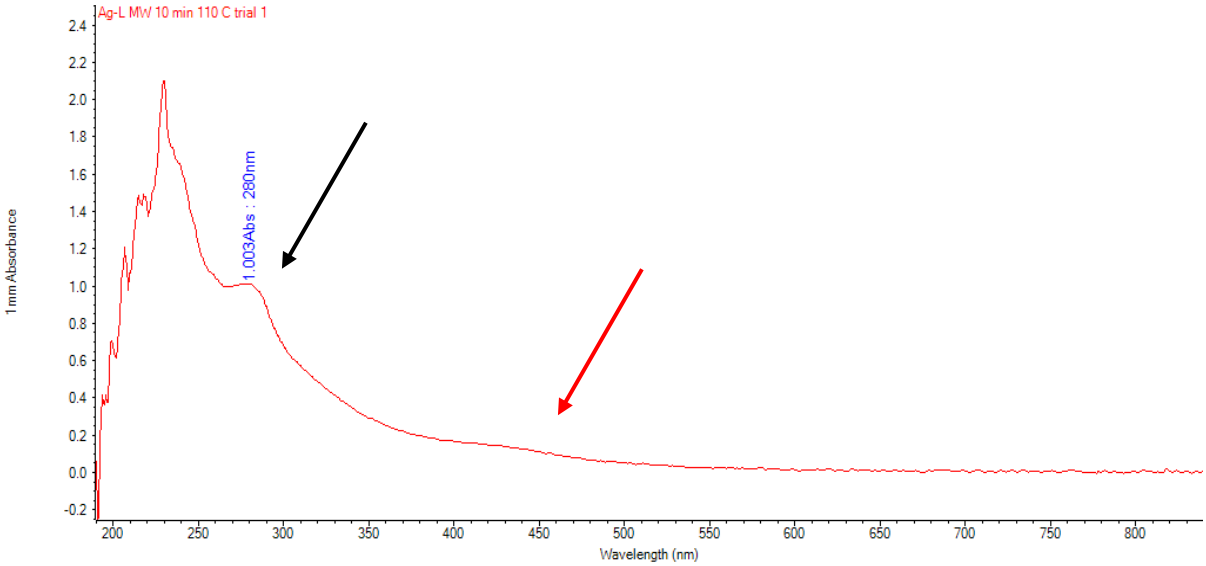

Figure 23: UV-Vis analysis of L-AgNPs produced by microwaved-assisted synthesis for 10 minutes at 110°C showing peak around 280 nm due to lignin (black arrow) and peak around 420 nm due to AgNPs (red arrow)

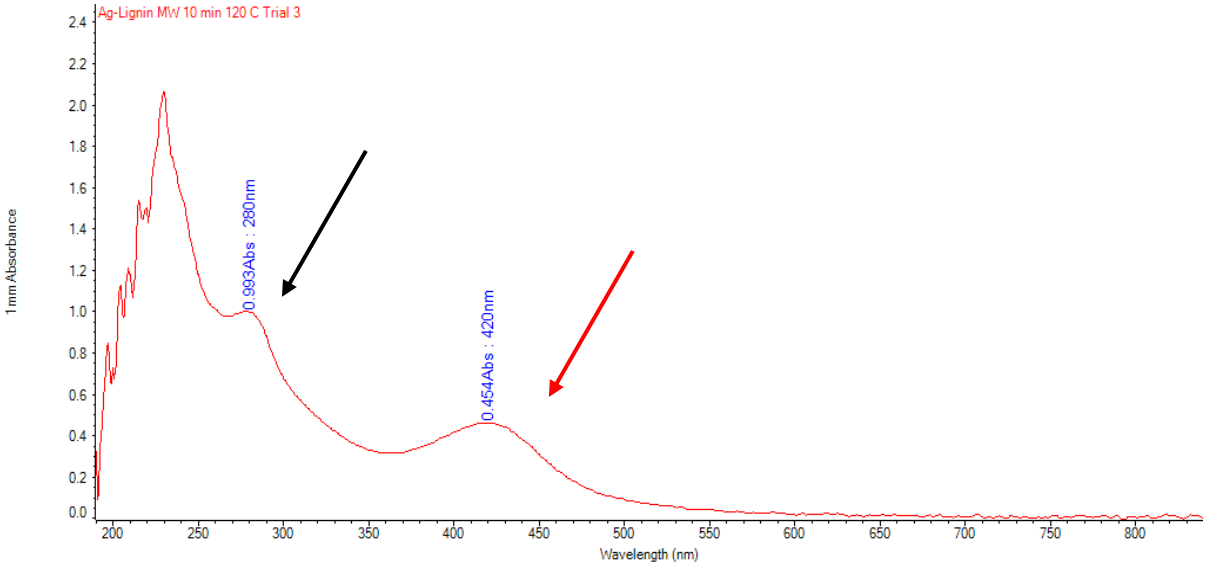

Figure 24: UV-Vis analysis of L-AgNPs produced by microwaved-assisted synthesis for 10 minutes at 120°C showing peak around 280 nm due to lignin (black arrow) and peak around 420 nm due to AgNPs (red arrow)

The analyses in Figure 19 and Figure 20 show a peak around 280 nm (black arrow) but no peak around 420 nm indicating the presence of lignin, but no AgNPs. At 60°C there is an undetectable amount of AgNP formation even after 6 hours of processing time. As the temperature is increased starting at 100°C (Figure 21) a small shoulder can be seen around 420 nm (red arrow) up to 110°C (Figure 23), while at 120°C (Figure 24) a full peak can be seen at 420 nm indicating reliable AgNP

formation in just 10 minutes. Particles produced by microwave-assisted synthesis show slight AgNP formation in 10 minutes from 100°C to 110°C and definite AgNP formation at 120°C.

2.3.2.2 X-Ray Diffraction Analysis

The particles produced by microwave-assisted synthesis for 10 minutes at 120°C were the only particles that showed reliable AgNP formation, so they were the only condition selected for XRD analysis.

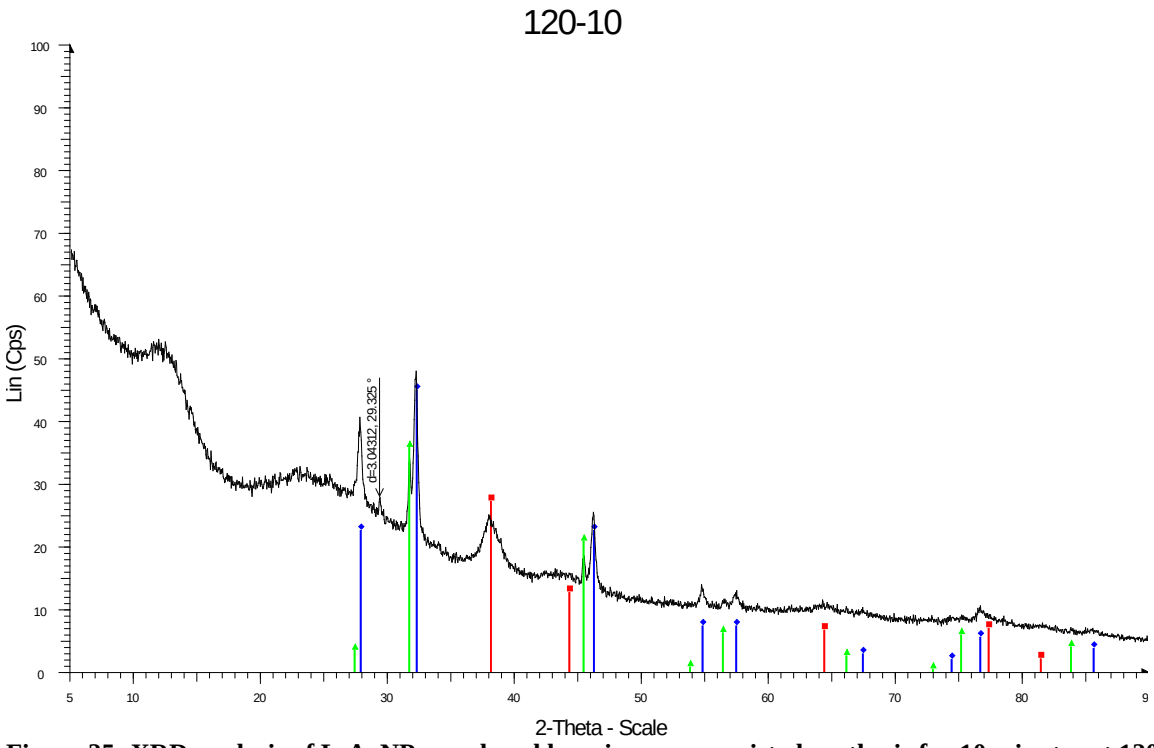

Figure 25: XRD analysis of L-AgNPs produced by microwave-assisted synthesis for 10 minutes at 120°C (blue line corresponds to AgCl and red line corresponds to Ag0)

It is clear from the XRD analysis that the particles produced by microwave-assisted synthesis for 10 minutes at 120°C are almost identical in chemical structure to the particles produced by aerobic or anaerobic 72-hour heating synthesis with pH modification. This means that the microwave-assisted synthesis method I have developed is capable of producing particles with the same chemical properties as the 72-hour heating synthesis while decreasing processing time to 10 minutes. Again these particles contain some amount of AgCl and Ag^0 so for the remaining work in this thesis the results pertain to particles containing both AgCl and Ag^0. Recent research

indicates that the presence of AgCl can provide an additional source of silver ions which can augment the antimicrobial effect of the AgNPs [202].

2.3.2.3 Dynamic Light Scattering Analysis

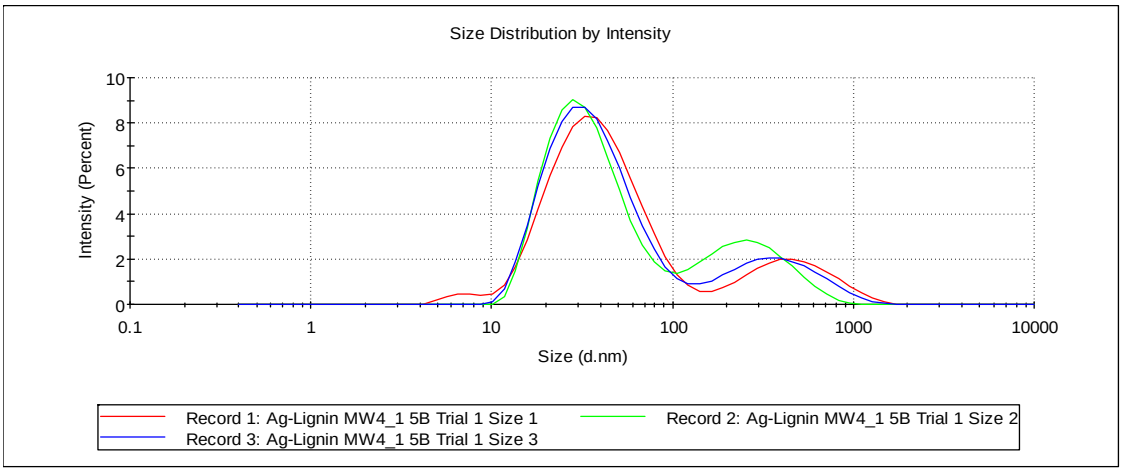

Figure 26: DLS size analysis of L-AgNPs produced by microwaved-assisted synthesis for 4 hours at 60°C

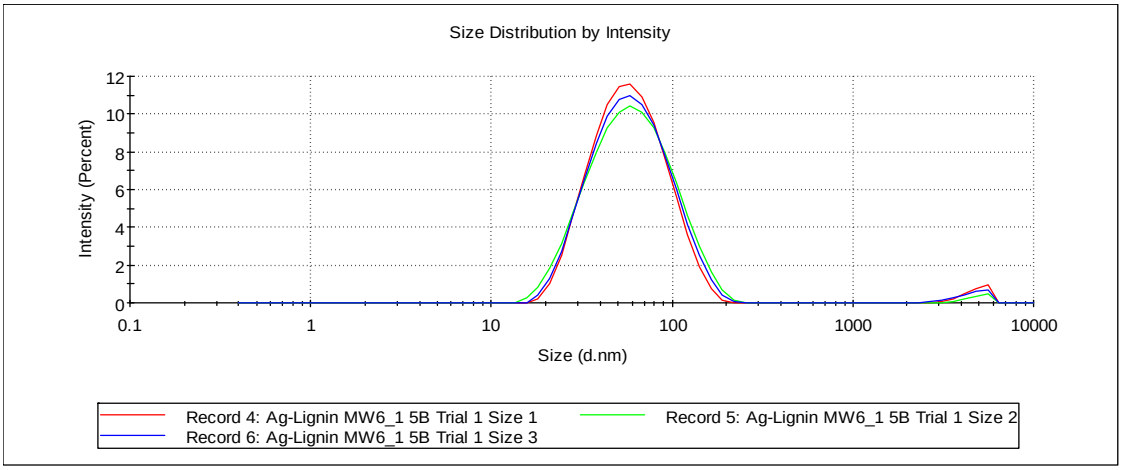

Figure 27: DLS size analysis of L-AgNPs produced by microwaved-assisted synthesis for 6 hours at 60°C

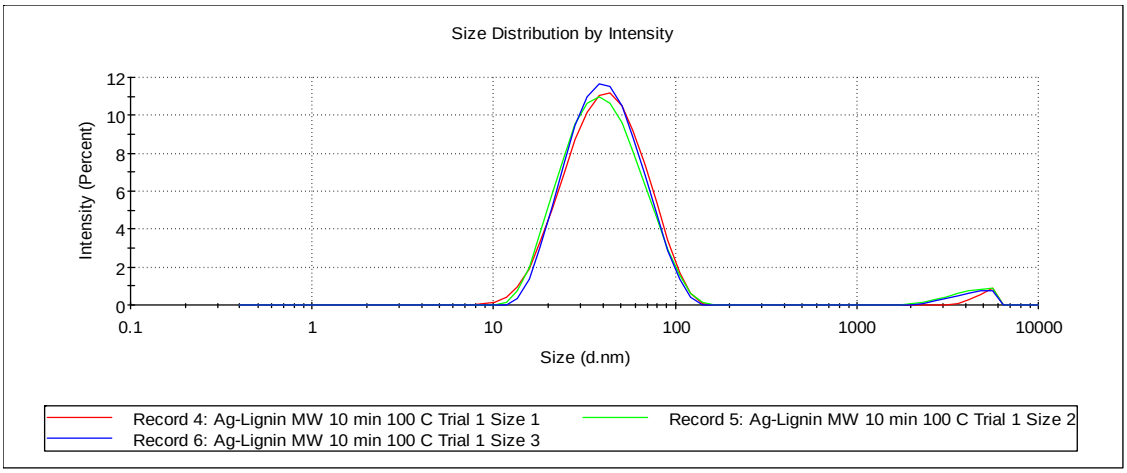

Figure 28: DLS size analysis of L-AgNPs produced by microwaved-assisted synthesis for 10 minutes at 100°C

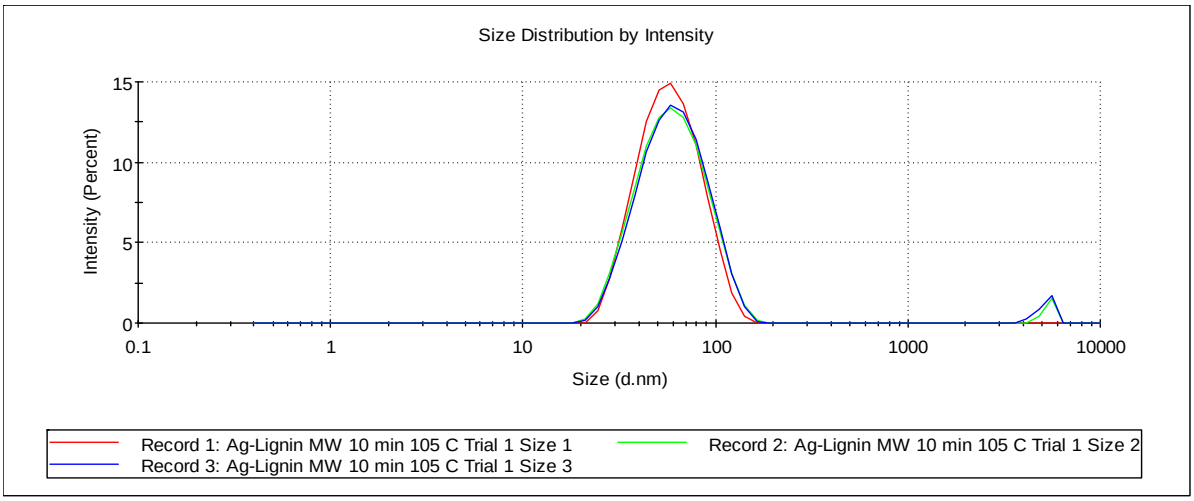

Figure 29: DLS size analysis of L-AgNPs produced by microwaved-assisted synthesis for 10 minutes at 105°C

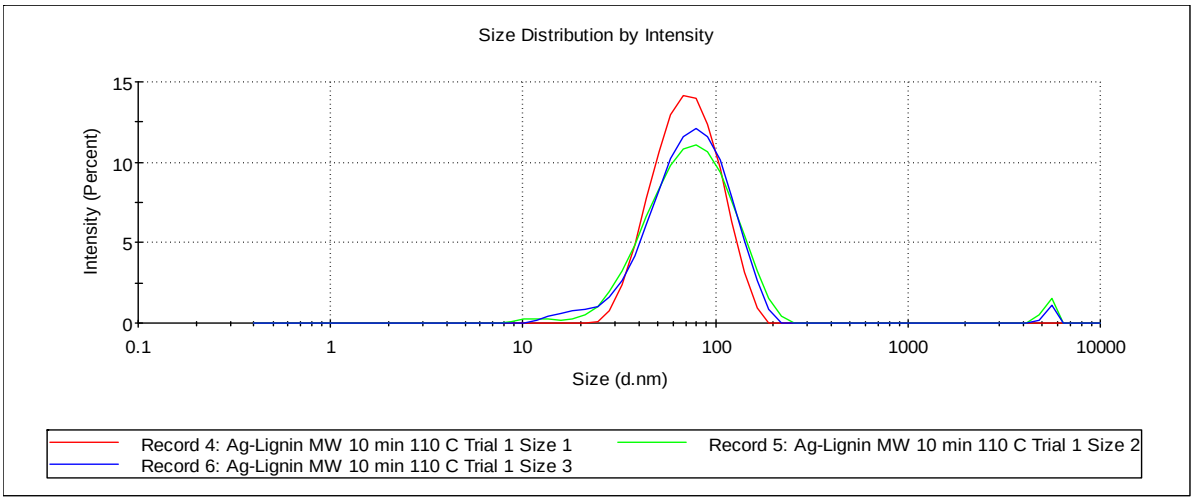

Figure 30: DLS size analysis of L-AgNPs produced by microwaved-assisted synthesis for 10 minutes at 110°C

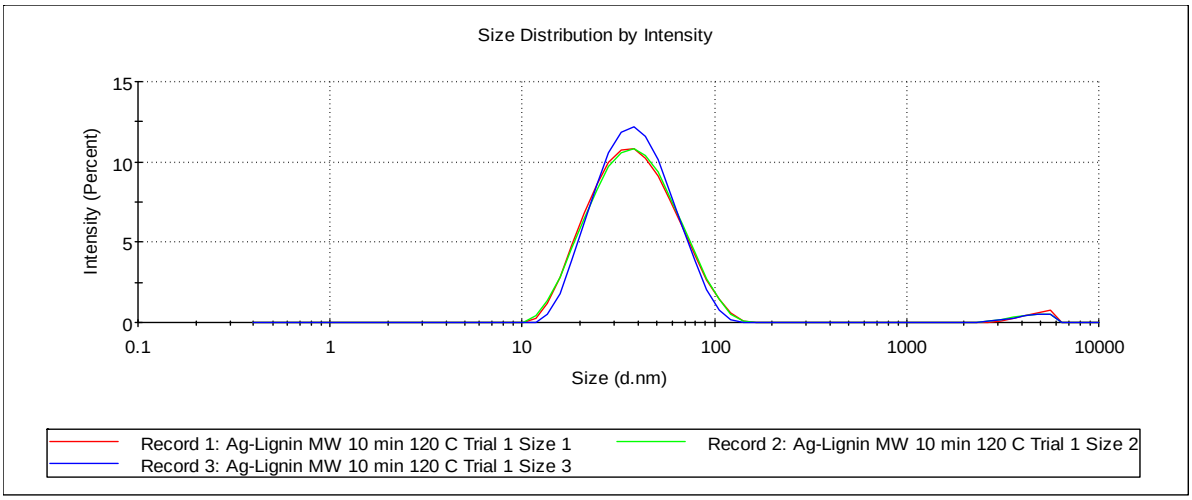

Figure 31: DLS size analysis of L-AgNPs produced by microwaved-assisted synthesis for 10 minutes at 120°C

DLS analysis on the particles produced by microwave-assisted synthesis with varying temperature shows that all methods are capable of producing particles in the nanoscale range (Figure 26 – Figure 31). It is likely that at temperatures of 60 to below 100°C reaction kinetics are so slow that there are simply not enough AgNPs being produced to show a peak on the UV-Vis analysis (Figure 19 and Figure 20). At a processing time of 10 minutes and a temperature of 120°C it appears that the most reliable particles are obtained, so these conditions were chosen for the experiments where varying silver concentrations were examined (Figure 31).

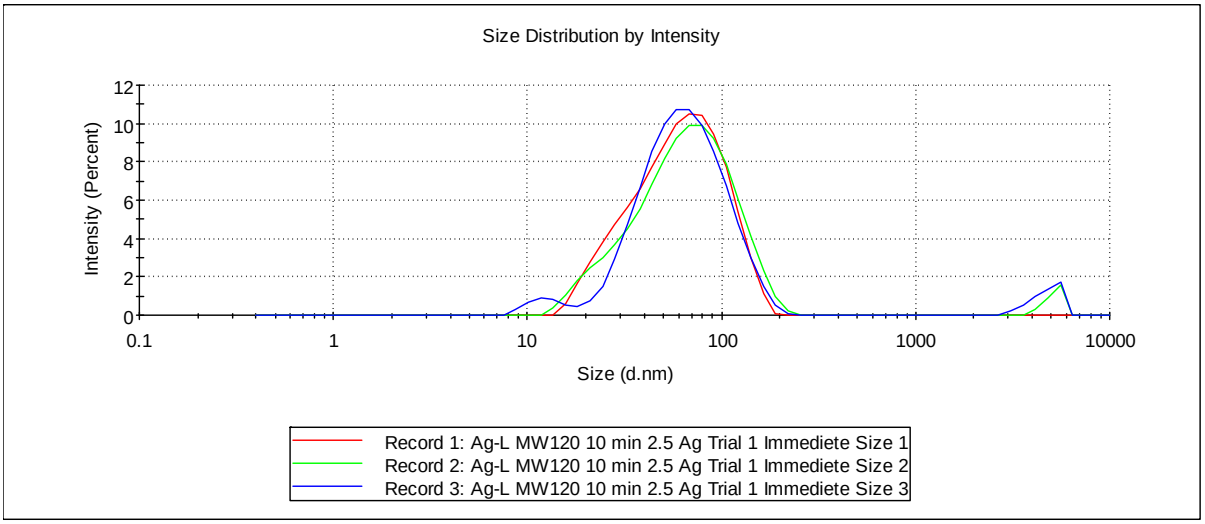

Figure 32: DLS size analysis of L-AgNPs produced by microwaved-assisted synthesis with 2.5 mg/mL $AgNO_3$

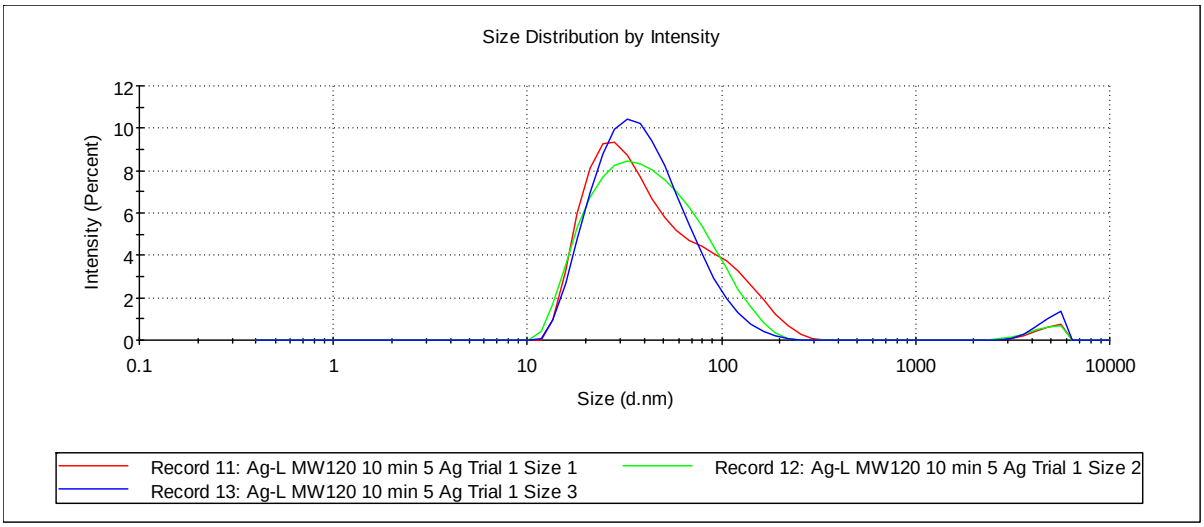

Figure 33: DLS size analysis of L-AgNPs produced by microwaved-assisted synthesis with 5 mg/mL $AgNO_3$

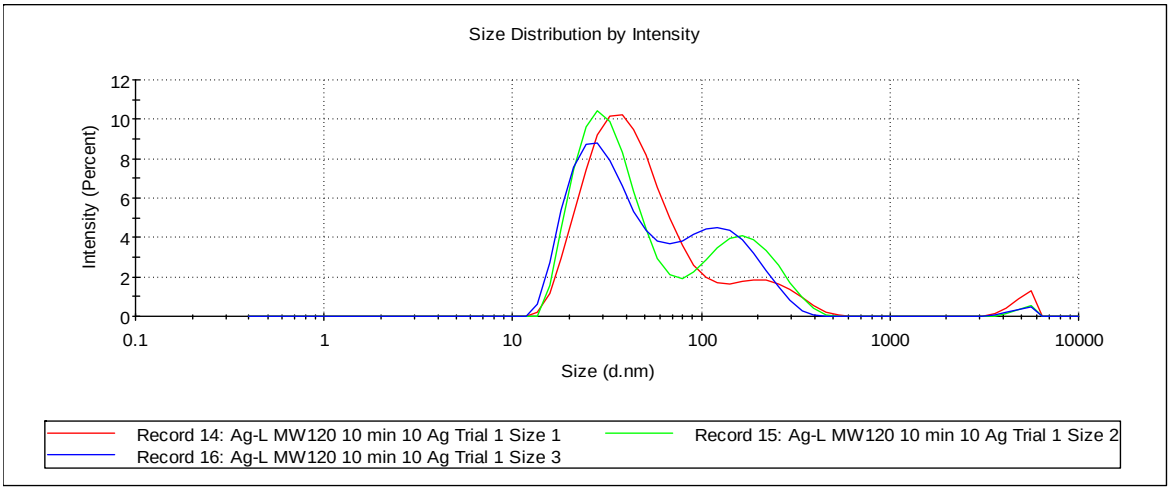

Figure 34: DLS size analysis of L-AgNPs produced by microwaved-assisted synthesis with 10 mg/mL AgNO3

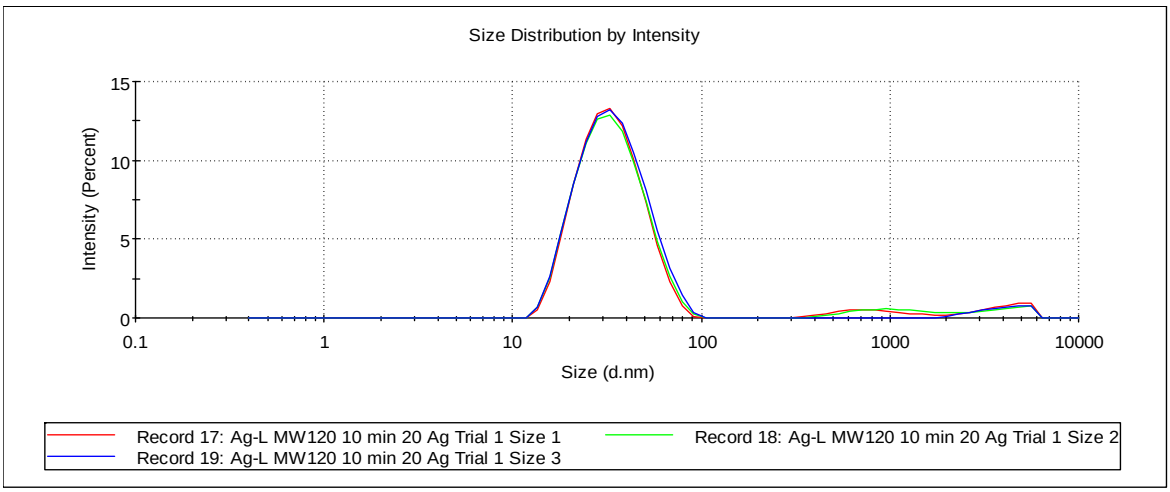

Figure 35: DLS size analysis of L-AgNPs produced by microwaved-assisted synthesis with 20 mg/mL $AgNO_3$

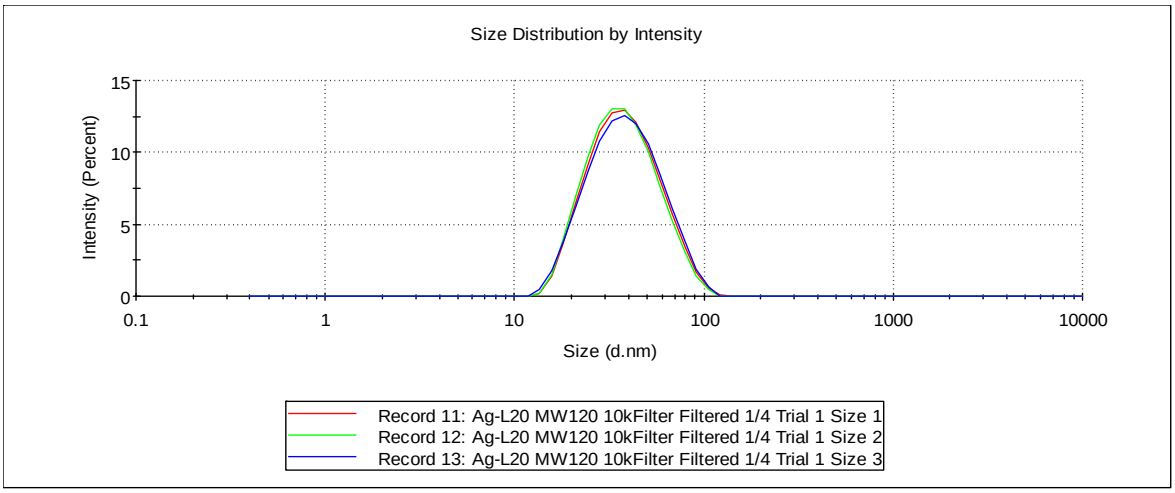

Figure 36: DLS size analysis of L-AgNPs produced by microwaved-assisted synthesis with 20 mg/mL $AgNO_3$ then microconcentrated with a 10 kDa filter and resuspended in DI water

Table 4: Comparison of peak sizes for different conditions used to produce Ag-lignin nanoparticles

Batch Conditions	Main Peak (nm)	Minor Peak (nm)
Aerobic 72 h heating (2 mg/mL $AgNO_3$)	62.34	4.26
Anaerobic 72 h heating (2 mg/mL $AgNO_3$)	53.53	4.796
2 mg/mL $AgNO_3$	42.03	4519
2.5 mg/mL $AgNO_3$	69.33	3302
5 mg/mL $AgNO_3$	49.29	4754
10 mg/mL $AgNO_3$	38.26	181
20 mg/mL $AgNO_3$	35.04	-
20 mg/mL $AgNO_3$ – microconcentrated (passed through a 10 kDa microconcentrator)	40.76	-

AgNPs were produced with $AgNO_3$ starting concentrations of 2 to 20 mg/mL. The particles seemed to show slightly altered size distributions at different $AgNO_3$ concentrations with a significant amount of aggregate formation being seen in Figure 34. The most evenly distributed particles were formed by microwave-assisted synthesis at a starting $AgNO_3$ concentration of 20 mg/mL. A comparison of the mean diameters of the particles produced by varying $AgNO_3$ concentration can be seen in Table 4. By comparing AgNP diameter sizes it can be determined that increasing silver concentration will generally produce smaller particle sizes. Some larger

aggregates are also formed by microwave-assisted synthesis, but they can be removed by simple filtration of the produced particles through a 0.22 µm syringe filter. It is also clear from Figure 36 that particles did not pass through a 10 kDa microconcentration filter and were easily resuspended in DI water while retaining their size distribution, meaning that they can be cleaned by washing in this manner. The supernatant obtained from washing the particles in this manner was also collected and analyzed by UV-Vis and DLS but the concentration of particles was below the limit of detection for both analytical techniques.

2.3.2.4 Zeta Potential Analysis

Table 5: Zeta potential analysis for L-AgNPs produced by microwave-assisted synthesis (MW = microwave) at 110°C, 120°C, and particles produced at 120°C using 20 mg/mL $AgNO_3$

	MW 110°C	MW 120°C	MW 120°C (20 mg/mL $AgNO_3$)
Zeta Potential (mV)	-56.9	-48	-47.5
Standard Deviation (mV)	0.819	1.58	3.26

The microwave-assisted synthesis methods (Table 5) produce particles with "good stability" as evident by the highly negative zeta potentials. These particles have similar stability as the ones produced by the 72 h heating synthesis methods (Table 3). No aggregation has been observed during storage for up to 10 months.

2.3.2.5 Scanning Transmission Electron Microscopy (STEM) Analysis

Initially STEM analysis was performed on particles produced by microwaved-assisted synthesis at 60°C for 4 and 6 hours. The UV-Vis results for the L-AgNPs produced by microwave-assisted synthesis between 100 and 120°C were used to choose only the particles produced at 110°C and 120°C for further STEM analysis. All particles in these images have been negatively stained using uranyl acetate.

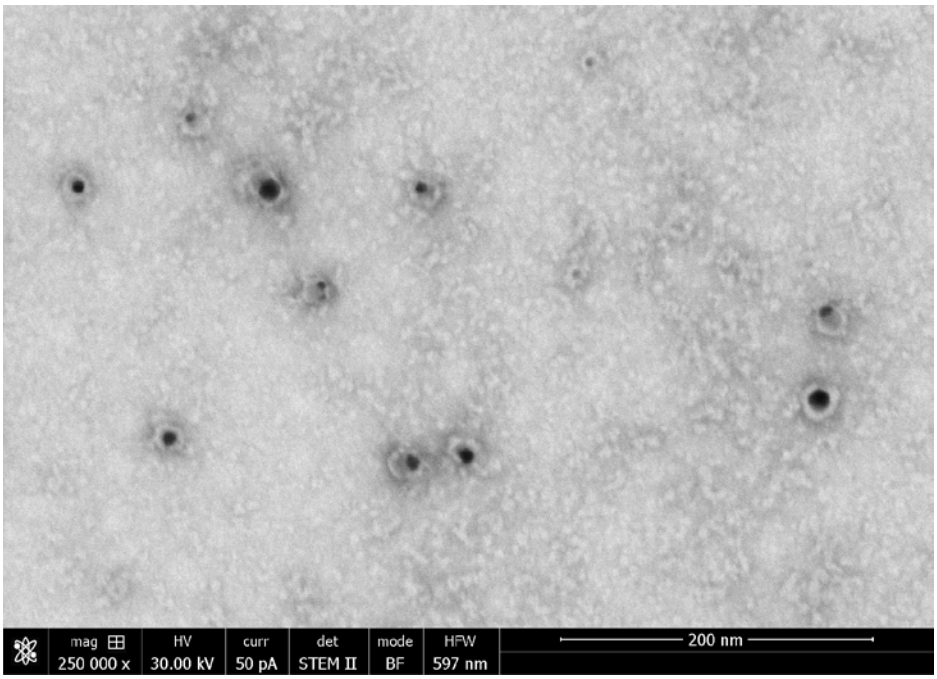

Figure 37: Negatively stained STEM image of L-AgNPs produced by microwaved-assisted synthesis for 4 hours at 60°C

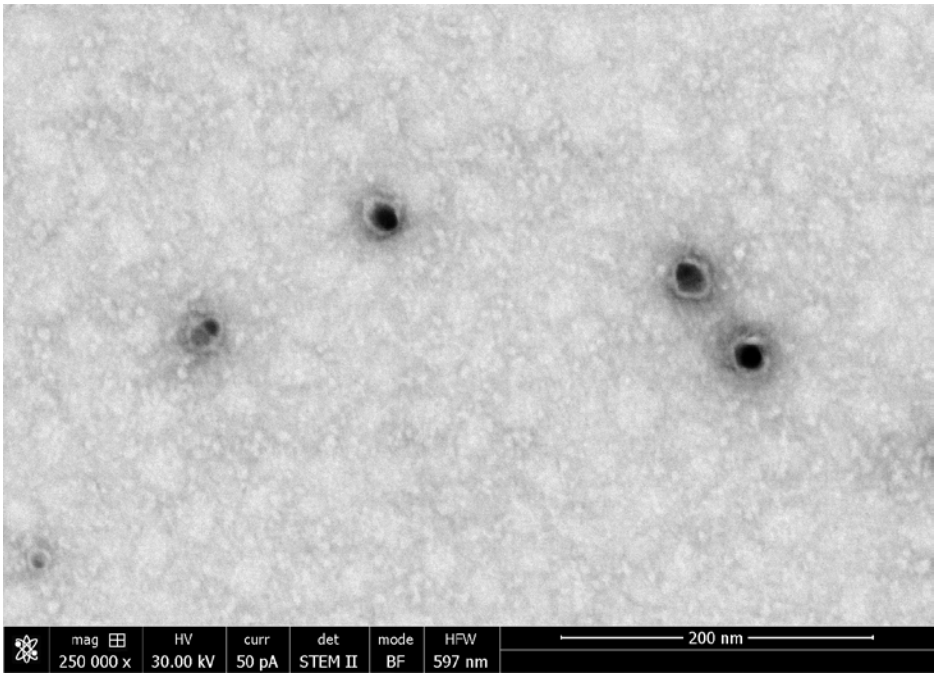

Figure 38: Negatively stained STEM image of L-AgNPs produced by microwaved-assisted synthesis for 6 hours at 60°C

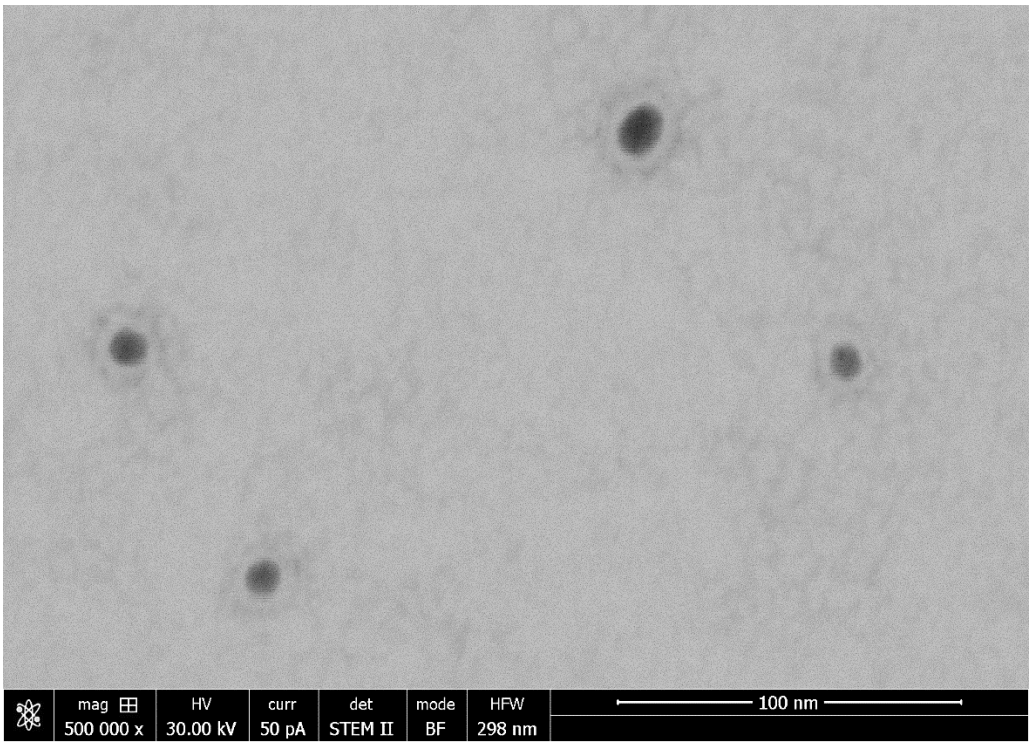

Figure 39: Negatively stained STEM image of L-AgNPs produced by microwaved-assisted synthesis for 10 minutes at 110°C

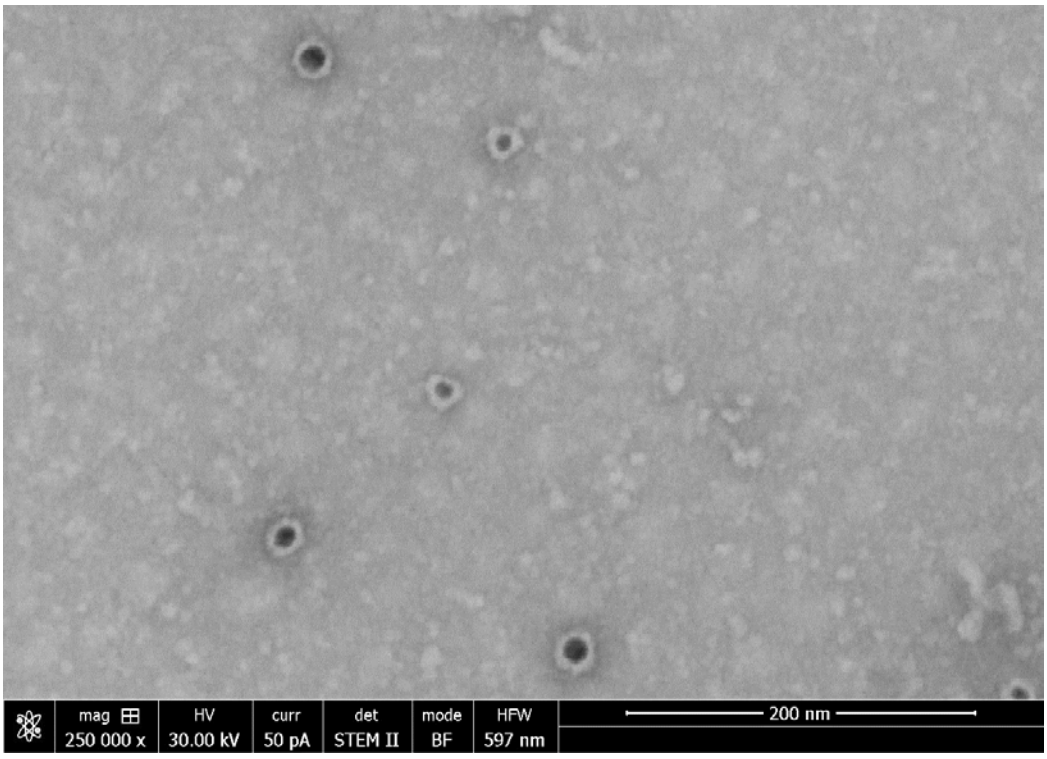

Figure 40: Negatively stained STEM image of L-AgNPs produced by microwaved-assisted synthesis for 10 minutes at 120°C

STEM images confirmed that L-AgNPs are produced under all described microwave-assisted synthesis conditions. The characteristic halo indicating a lignin cap can be seen in all produced images. The lignin likely caps these AgNPs through ionic interactions between the charged functional groups on the lignin and the silver ions present on the surface of the AgNPs. It is interesting that L-AgNP formation is observed for the microwave-assisted synthesis at 60°C for both 4 and 6 hours, while the UV-Vis analysis does not show any AgNP formation. Once again, this is likely due to the particles being produced in such low amounts (due to drastically reduced reaction kinetics) that while they do show up on DLS and STEM they do not show up on the UV-Vis analysis. DLS and STEM are significantly more sensitive analytical methods than UV-Vis, which might explain these findings. The STEM analysis provides additional confirmation that microwave-assisted synthesis methods are capable of producing particles with the same chemical composition, size distribution, and surface morphology as those produced by the 72-hour heating methods while reducing processing time to only 10 minutes.

2.4 Conclusions

In conclusion, particles produced by 72-hour heating synthesis with and without pH modification and under aerobic and anaerobic conditions have been synthesized and fully characterized. A microwave-assisted synthesis method was developed that is capable of producing particles with almost identical chemical composition, size distribution, and surface morphology. All methods are capable of producing L-AgNPs as determined by UV-Vis, DLS, and STEM. All produced L-AgNPs are classified under “good stability” based on zeta potential analysis. Particles produced with pH modification of the starting lignin solution produce L-AgNPs that also contain some AgCl which might be crucial for the antimicrobial activity of these particles. In this thesis, the effects of Ag^0 and AgCl have to be attributed to both forms of silver, but no clear distinction is possible. For this reason, we simple refer to the particles as L-AgNPs in the following chapters. These particles have been fully characterized and are ready for antimicrobial testing both *in vitro* and *in vivo*, and for conjugation with radioactive tracers to determine their biodistribution.

Chapter 3: Radioactive Tagging and Biodistribution

With the rise in use of AgNPs in consumer and therapeutic applications it is imperative to understand how they distribute within the body. Currently, the biodistribution of AgNPs is most often measured by sacrificing animals at specific time points and determining silver concentration in each individual organ by ICP-MS or other ICP methods. These methods, while simple, are significantly underpowered because they do not provide any differentiation between AgNPs and silver ions, cannot show real-time tracking of AgNP distribution, and are extensively time and resource intensive. A simple way to alleviate all these issues is by conjugating AgNPs with a radioactive isotope that can be seen on a radioactive imaging camera. For these imaging methods to work a radiotracer must be chosen with an appropriate half-life, significant gamma ray emission, and it must not alter the chemical structure of the AgNPs. The biodistribution studies were carried out in adherence to ACC protocol A16-0150 VECTor/CT Biodistribution and Imaging Studies II.

3.1 Hypothesis and Objectives

For the biodistribution of L-AgNPs, I have chosen to conjugate the lignin with the SPECT radioisotope ^{123}I. Iodine-123 decays by electron capture to ^{123}Te, and has a half-life of 13.22 hours which makes it an ideal isotope for imaging studies up to about 2 days [206]. The gamma ray emission occurs at an energy of 159 keV which is ideal for SPECT imaging. Additionally, ^{123}I can be easily bound to phenolic aromatics (very abundant in lignin) through a simple iodination reaction (the mechanism can be seen in Figure 41). I hypothesize that the L-AgNPs will be radioactively labeled through the binding of ^{123}I to a phenolic aromatic, and they will be easily imaged on a SPECT/CT imaging machine when administered to a mouse by subcutaneous (SQ) injection or by intratracheal instillation. Further, when administered the L-AgNPs will remain mostly at the injection site with minimal translocation to the kidneys, spleen, and liver. Additionally, any remaining (or released) free Na-^{123}I will distribute systemically and accumulate in the thyroid.

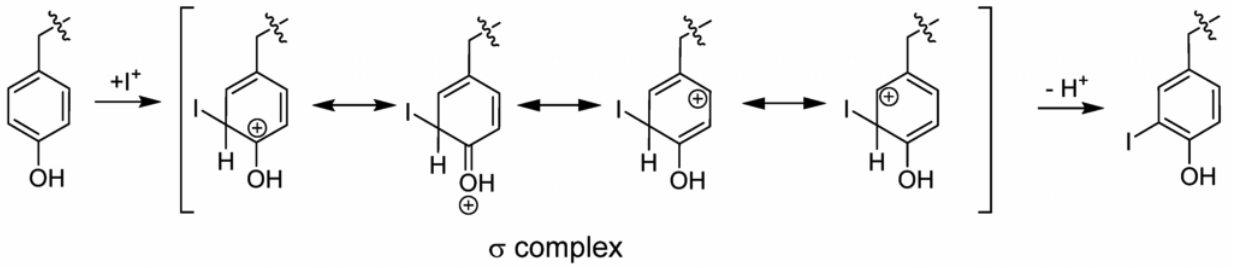

Figure 41: Electrophilic substitution mechanism for iodination of phenol with the help of iodination beads

Since the ^{123}I is bound to the lignin, it is also necessary to radioactively tag the silver core to determine if the lignin coating separates from the silver core in the body and to ensure that the results of the ^{123}I biodistribution study are accurate. To accomplish this I have radioactively tagged the silver core using the radioisotope ^{111}Ag. Silver-111 has a half-life of 7.47 days, and decays by 92% β^- emission at 1.037 MeV, 1.3% gamma emission at 245 keV, and 6.7% gamma emission at 342 keV [52]. To date, ^{111}Ag has only been used for autoradiography and gamma counting, but not for imaging, although its gamma emission is in the SPECT imaging range (70 – 360 keV) and should allow for SPECT/CT imaging [52,53]. Additionally, the long half-life of 7.47 days is ideal for the 72-hour synthesis method because minimal amounts of radiation will be lost over this period of time. It is also theoretically possible to do a dual imaging study using ^{123}I and ^{111}Ag labeled L-AgNPs because the energy levels of the gamma emission of both isotopes do not overlap (Figure 42). I hypothesize that the silver core of the L-AgNPs can be radiolabeled by doping the $AgNO_3$ with ^{111}Ag to produce $^{111}AgNO_3$ for L-AgNP production, and it will be visible when imaged using a SPECT/CT machine.

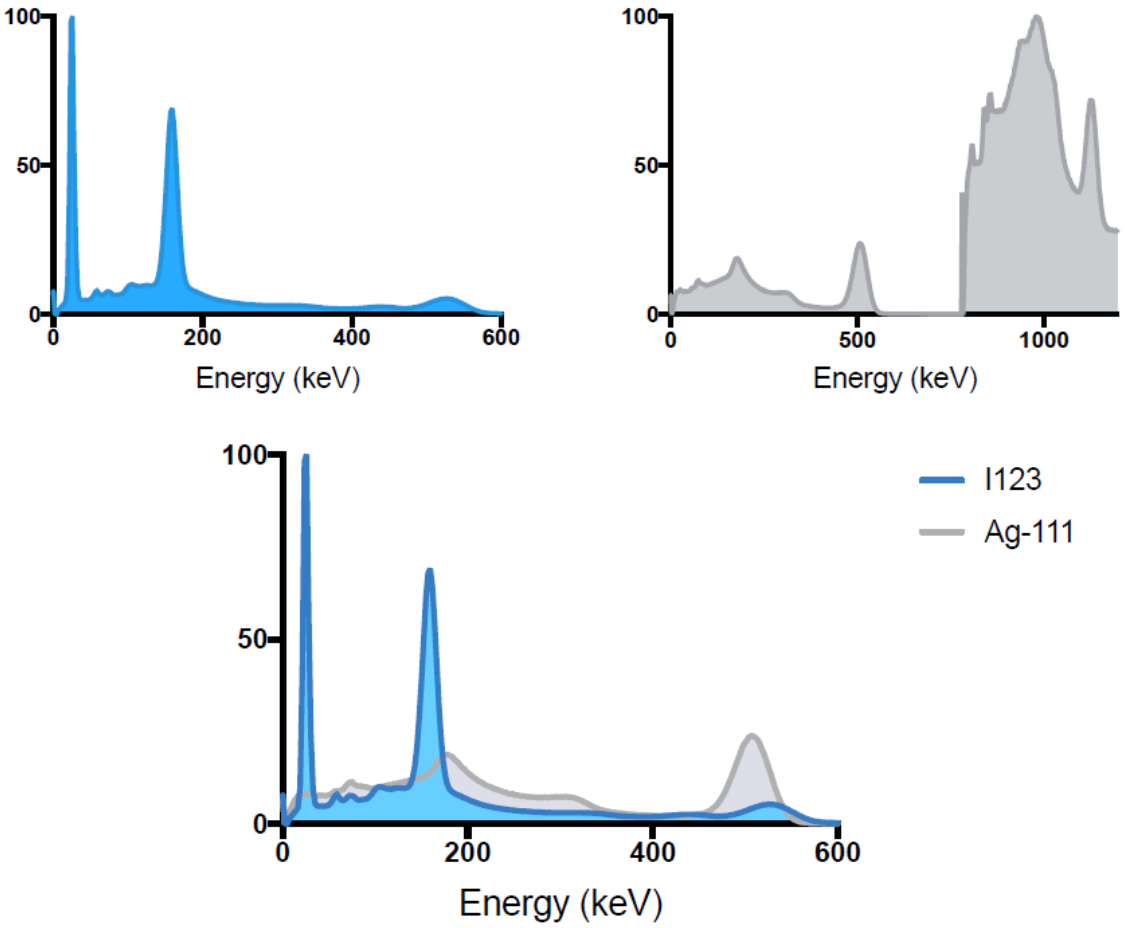

Figure 42: Energy level diagrams for ^{123}I (blue) and ^{111}Ag (grey) showing potential for dual imaging study

^{111}Ag was received from Oak Ridge National Lab (ORNL)in the form of dried silver nitrate ($AgNO_3$). The ^{111}Ag is produced as a side reaction of the production of ^{225}Ac by proton irradiation of a thorium target along with many other radioisotopes, and is removed through a CL resin column. The CL resin column contains a solvent impregnated resin (SIR) carrying an organic solution of alkyl phosphine sulfides and alkyl phosphine oxides (manufactured by Triskem) [207]. The separation mechanism is explained in depth in a recent paper by Mastren et al., and occurs through binding of Ag(I) to a CL resin column which after rinsing can be eluted with 10 M HNO_3 in a two stage process [207].

This chapter contains the results of the radioactive labeling of the L-AgNPs using ^{123}I or ^{111}Ag, and the biodistribution experiments conducted using ^{123}I. The labeling efficiency and particle characterization of the radioactive tagging experiments is presented for ^{123}I and ^{111}Ag.

Biodistribution images obtained from SPECT/CT imaging are presented for SQ injection and intratracheal instillation of ^{123}I-labeled L-AgNPs. The labeling efficiencies, and biodistribution of both administration routes is discussed along with the choice of radiotracer.

3.2 Radiolabeling and Imaging Methods

3.2.1 Radiolabeling Ag-Lignin Nanoparticles with ^{123}I

For this radiolabeling procedure the phenolic aromatics on the lignin are bound to ^{123}I via an electrophilic substitution using iodination beads. First 450 µL of PBS was added to a Thermo Scientific Pierce® Iodination Bead (#28665, ThermoFisher Scientific, Waltham, MA, USA) along with 7 µL of Na^{123}I, and the reaction vial was shaken for 20 min. Then 100 µL of the Ag-Lignin NPs and 150 µL of the iodinated PBS was added to each of n=3 vials and each was shaken for 30 min. Each sample was put into a 10 kDa microconcentration filter with an additional 100 µL of clean PBS and ultracentrifuged at 20,817 × *g* for 10 min. The supernatant was then removed and the filters were washed with 350 µL of PBS and ultracentrifuged again at 20,817 × *g* for 10 min. The supernatant was removed again and the filters were inverted followed by ultracentrifugation at 2,655 × *g* for 5 min, and all samples were resuspended in 100 µL of PBS. All sample activities were measured in a Biodex Atomlab 500 dose calibrator or a Capintec CRC-55tR.

3.2.2 Microwave-Assisted Synthesis of Ag-Lignin Nanoparticles with ^{123}I-Labeled Lignin

The radiolabeling of already produced L-AgNPs caused aggregation of particles so in this synthesis method the lignin was first labeled with ^{123}I, then used to produced ^{123}I-labeled L-AgNPs. As in the previous synthesis method, 450 µL of PBS and 7 µL of Na^{123}I was added to a Thermo Scientific Pierce™ Iodination Bead and shaken for 20 min. Then 500 µL of the Lignin (1%, pH = 5.5) was added to the iodinated PBS and shaken for 30 min. Next each sample was put into a 2 kDa microconcentration filter with an additional 100 µL of clean PBS and ultracentrifuged at 20,817 × *g* for 20 min. The supernatant was removed and the filters were washed with 350 µL of PBS and ultracentrifuged again at 20,817 × *g* for 20 min. The supernatant was removed and the filters were inverted followed by ultracentrifugation at 2,655 × *g* for 5 min, and all samples were resuspended in 500 µL of DI water. The 500 µL of iodinated lignin solution was mixed with 1 mL

of lignin solution (1%, pH = 5.5) and 1 mL of 2 mg/mL $AgNO_3$ in a 2 – 5 mL microwave vial and microwaved at 120°C for 10 minutes with a pressure setting of 5 bar. The vial was allowed to decay for several days in the fridge before the size distribution was measured by DLS.

3.2.3 Synthesizing Radiolabeled Ag-Lignin Nanoparticles with ^{111}Ag

The synthesis of the ^{111}Ag-labeled L-AgNPs was conducted by doping the $AgNO_3$ with ^{111}Ag and then producing L-AgNPs by aerobic 72-hour heating synthesis. The ^{111}Ag was purified by suspending in HNO_3 and H_2O_2 and slowing heating the solution to remove any impurities. For the ^{111}Ag-labeled L-AgNP synthesis, 500 µL of lignin solution (1%, pH = 9.5) and 333 µL of $AgNO_3$ solution (2 mg/mL) was added to all of the purified ^{111}Ag activity. The pH of the mixture was adjusted to 6 using 6 M NaOH and 6 M HNO_3 and the reaction vial was set to shake at 300 rpm in a lead-lined fume hood for 72 h at 68°C. A cold synthesis of the reaction was run in parallel using the same chemicals, but without any of the radioactive silver.

3.2.4 Biodistribution of ^{123}I-Labeled Ag-Lignin Nanoparticles Delivered via Intratracheal Instillation

The intratracheal instillation model was utilized to ensure L-AgNP delivery directly to the lungs. The method of intratracheal instillation was performed similarly to one described by Ortiz-Muñoz and Looney [208]. For this model three 20 g CD-1 female mice were anesthetized with a mixture of ketamine (40 mg/kg) and xylazine (2.5 mg/kg) administered by intraperitoneal (IP) injection. Then 50 µL of ^{123}I-labeled L-AgNPs were administered directly to the lungs by insulin syringe attached to p10 tubing and fed by catheter directly into the trachea. The animals were imaged on a VECTor™ SPECT/CT machine (MILabs, The Netherlands). Respiratory rate and body temperature were constantly monitored during scanning, and bed temperature and isoflurane flow rate were adjusted accordingly. The resulting histology was performed first by fixing the tissue in 10% neutral buffered formalin (tissue sample fixation for at least 48 h). Then the tissue was processed, paraffin embedded, and block sectioning was performed at a thickness of 5 µm. Finally, the unstained tissue sections were deparaffinized, rehydrated, H&E stained and coverslipped.

All produced SPECT/CT images were processed by centering the ^{123}I photopeak window at 158.5 keV with a 20% energy window width. SPECT image reconstructions were carried out with a pixel-ordered subset expectation maximization (POSEM) algorithm that included resolution recovery. For the SPECT images, 16 subsets, 10 iterations and an isotropic 0.4 mm voxel grid were used. The images were decay corrected and after CT registration, attenuation correction was applied. CT scans were acquired with a tube setting of 45 kV and 615 µA. In total 2 frames of 180 projections over 360 degrees were acquired in step and shoot rotation mode. The acquired projection data was reconstructed using SkyScan NRecon software to generate a 3D CT image on 0.169 mm^3 voxel size.

3.2.5 Biodistribution of ^{123}I-Labeled Ag-Lignin Nanoparticles Delivered via Subcutaneous Injection

Due to difficulties with the intratracheal instillation model, a subcutaneous injection model was also investigated to determine the biodistribution of the radiolabeled L-AgNPs. In this model four 29 g CD-1 female mice were anesthetized using isoflurane. Then 100 µL (~16.65 MBq) of particles produced by microwave synthesis with ^{123}I-labeled lignin (as in section 3.2.2) were administered by subcutaneous injection right side of the dorsum underneath the thin skeletal muscle (n = 3). The final mouse was injected via the same route with 100 µL (~22.2 MBq) of free Na-^{123}I (control mouse). The animals were imaged on a MILabs VECTor™ SPECT/CT machine at 10 min, 2 hour, and 24 hours post-injection. Respiratory rate and body temperature were constantly monitored during scanning, and bed temperature and isoflurane flow rate were adjusted accordingly. The animals were sacrificed at 48 hours post-injection and blood was collected by cardiac puncture. All tissues of interest (blood, heart, liver, kidneys, lungs, small intestine, brain, bladder, muscle, spleen, bone, stomach, feces, pancreas) were collected, cleaned of blood, weighed, and their radioactivity was determined by gamma counter (Packard Cobra II auto-gamma counter, Perkin Elmer, Waltham, MA, USA).

3.3 Results and Discussion

3.3.1 Radiolabeling with ^{123}I

Table 6: Efficiencies of radiolabeling L-AgNPs with ^{123}I via iodine bead reaction

	Starting Activity (MBq)	Ending Activity (MBq)	Labeling Efficiency
Trial 1	12.14	8.473	69.79%
Trial 2	12.10	8.066	66.66%
Trial 3	12.06	7.326	60.75%
Average ± S.D.	12.10 ± 0.04	7.955 ± 0.5815	65.73% ± 4.59%

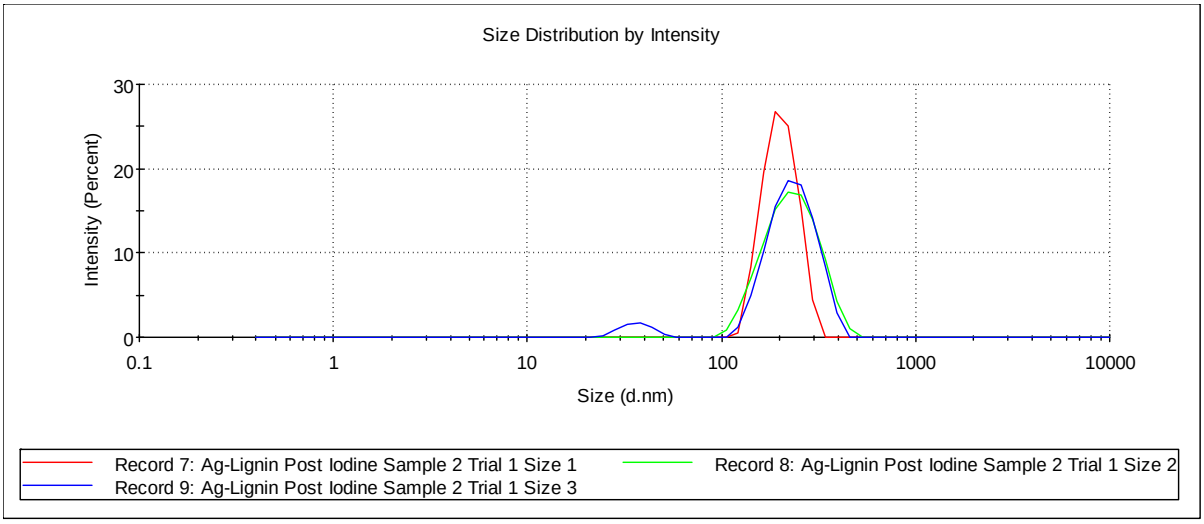

Figure 43: DLS size analysis of L-AgNPs radiolabeled with ^{123}I via iodine bead reaction

L-AgNPs can be successfully and reliably labeled with ^{123}I with a labeling efficiency of 65.73% and low standard deviation (Table 6), which will allow for accurate *in vivo* imaging with a SPECT/CT scanner. However, the DLS analysis (Figure 43) shows that after iodination the NPs from larger aggregates at around 180 nm in size compared to the roughly 50 nm particles, which were synthesized originally. While the produced particles can be labeled with high efficiency, the observed aggregation might cause certain changes in biodistribution.

Table 7: Efficiency of radiolabeling lignin before microwave synthesis of L-AgNPs

	Starting Activity (MBq)	Ending Activity (MBq)	Labelling Efficiency
Run 1	9.805	2.753	28.08%
Run 2	63.94	16.87	26.39%
Run 3	329.3	98.68	29.97%
Average ± S.D.	-	-	28.15 ± 1.79%

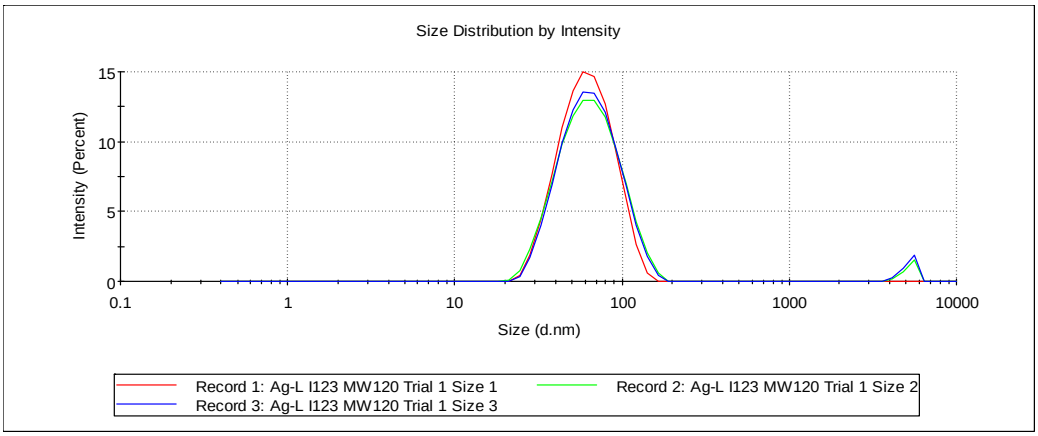

Figure 44: DLS size analysis of L-AgNPs produced by microwave-assisted synthesis for 10 min at 120°C using ^{123}I-labeled lignin

To prevent particle agglomeration an alternate radiolabeling procedure was chosen. Instead of radiolabeling the produced L-AgNPs the lignin was first radiolabeled with ^{123}I, then used to produce the L-AgNPs through a microwave-assisted synthesis method. Labeling the lignin with ^{123}I prior to producing particles by microwave irradiation produced particle size distributions indistinguishable of the cold microwave synthesis. However, the labeling efficiency of the lignin was significantly diminished from 65.73% to 28.15%.

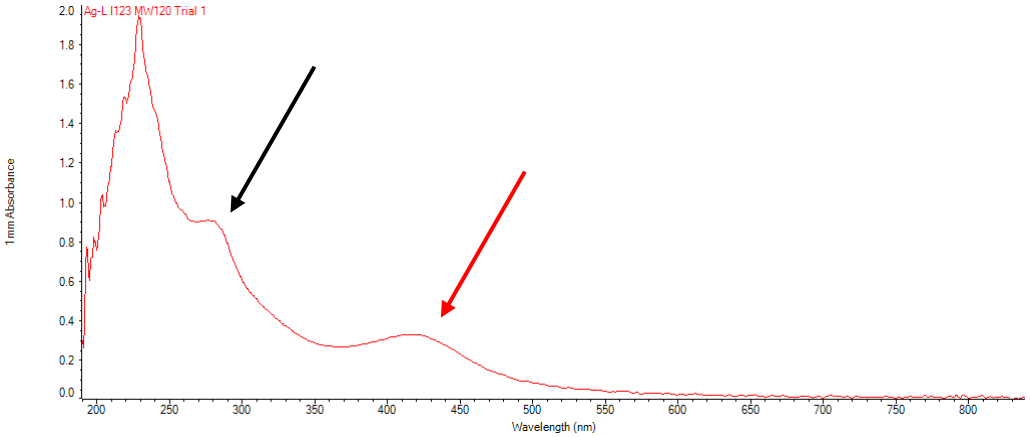

Figure 45: UV-Vis analysis of L-AgNPs produced by microwave-assisted synthesis for 10 mins at 120°C using ^{123}I-labeled lignin

Figure 45 shows that the microwave synthesis of L-AgNPs using previously radiolabeled lignin produces AgNPs with a similar UV-Vis spectrum to that of the particles produced with non-radiolabeled lignin. The spectrum shows the same characteristic peaks at 280 nm (black arrow) and 420 nm (red arrow) indicating presence of lignin aromatic bonds and formation of AgNPs, respectively. This demonstrates that the chemical structure is unchanged by the addition of ^{123}I, and that AgNP synthesis is possible using this method. These particles were considered to be stable as repeated washing with PBS up to 24 hours was not able to release any radioactivity into the buffer.

The issue of low labeling efficiency for labeling the lignin prior to L-AgNP production could be a potential problem because less radiation is introduced per dose which at the low gamma ray efficiency of the radioisotope makes it more difficult to detect in vivo by SPECT/CT. We circumvented this problem by microconcentrating the radiolabeled L-AgNPs with a 10 kDa filter and resuspending them in smaller liquid volumes, allowing for more radiation per dose and eliminating the issues caused by low labeling efficiency. However, when the particles are microconcentrated to allow for higher administered radiation doses then the L-AgNPs concentration administered also increases.

In conclusion, labeling the lignin by an iodination bead reaction, then producing L-AgNPs by microwave-assisted synthesis leads to the production of very stable, radioactively tagged particles. The size distribution is identical to that of the particles produced by the same method without

iodination, and the chemical structure remains unchanged as confirmed by an identical UV-Vis curve (Figure 45).

3.3.2 Biodistribution of L-AgNPs Radiolabeled with ^{123}I and Administered via Intratracheal Instillation

AgNPs are very effective at combatting drug-resistant bacteria when applied locally. In chronic lung infection models such as cystic fibrosis, multidrug resistant (MDR) bacteria tend to be present, causing the infections to be very difficult to treat with conventional antibiotics. For this reason the initial method of deliver for these L-AgNPs was chosen to be intratracheal instillation for direct delivery to the lungs and was imaged using SPECT/CT.

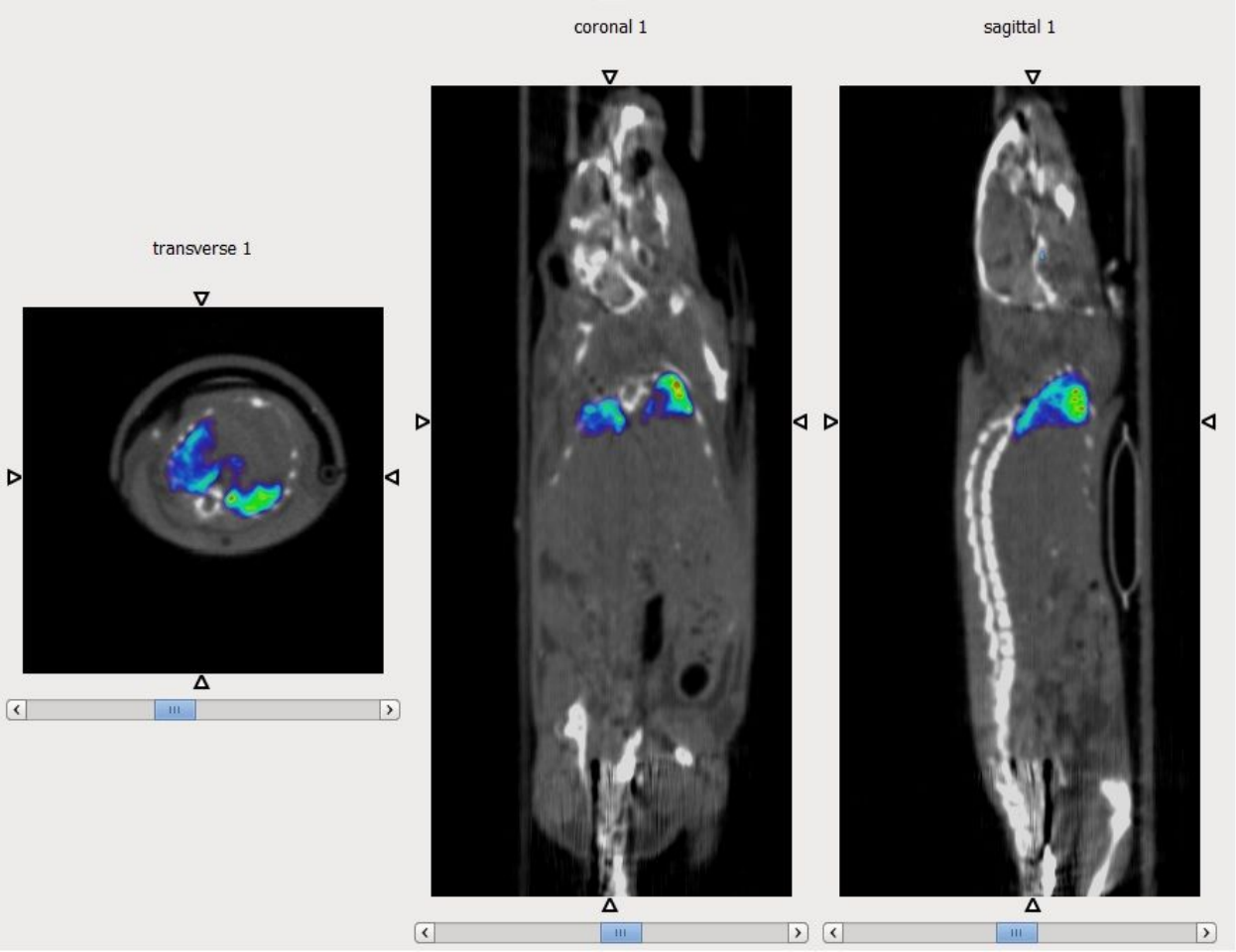

Figure 46: SPECT/CT image of first animal to receive ^{123}I-labeled L-AgNPs via intratracheal instillation

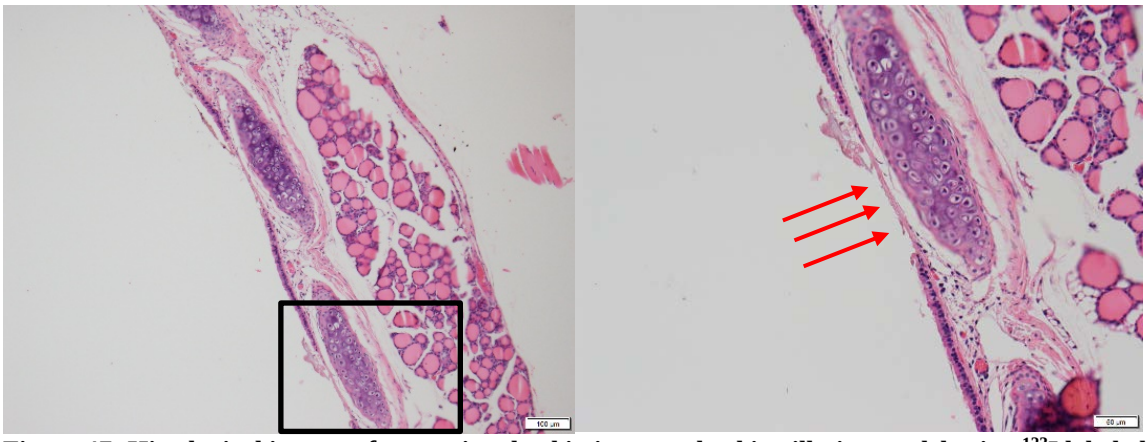

Figure 47: Histological images of mouse involved in intratracheal instillation model using ^{123}I labeled Ag-lignin nanoparticles showing damage to upper trachea (red arrow) at 10X (left image) and 20X (right image)

The intratracheal instillation proceeded smoothly for the first animal, and was imaged successfully (Figure 46). However, the animal's breathing slowed significantly during imaging and it was deceased by the time of exiting the scanner. The additional two animals that received the intratracheal instillation died even before they could be placed in the scanner, and the experiment was halted at that time.

The SPECT/CT image shown in Figure 46 demonstrates that the intratracheal instillation model works as expected. All of the radioactive activity that was administered to the animal remains in the lungs, which means that the method was successful at depositing all activity in the desired location without puncturing the lungs or trachea and without depositing any activity in the stomach.

Histology (Figure 47) was performed on one of the animals which died before it could be scanned, revealing significant physical damage to the upper trachea (red arrow). This damage may have led to severe laryngeal spasms causing severe hypoxia and acute death. All other inspected organs appeared normal, and there was no apparent damage to the lungs. The death of the animals was thus likely related to the method of administration and not caused by the particles themselves because damage was seen in the upper trachea, where no activity visualized in the SPECT/CT image, and not in the lungs where all the particles were delivered. Control experiments were then conducted to deliver saline to the lungs with the same intratracheal instillation model, without any complications. Further histology should be performed on animals receiving saline in this manner

to determine if the inhalation of the L-AgNPs or the administration of the model was the cause of the physical damage to the trachea.

AgNPs have been shown to cause significant decrease in mitochondrial activity *in vitro* and could potentially cause some toxicity *in vivo* [90]. However, the acute toxicity for AgNPs delivered to the lung is significantly higher than the dose used in this model so they should not cause toxicity [209]. Additionally, the only well-known mechanism of toxicity of AgNPs is liver toxicity resulting from oral or intravenous administration of AgNPs [162].

The intratracheal instillation model is quite difficult on small animals like mice. In this case the intratracheal model was not explored further due to the difficulties in administration.

3.3.3 Biodistribution of L-AgNPs Radiolabeled with ^{123}I and Administered via Subcutaneous Injection

Due to the drawbacks of the intratracheal instillation model and difficulties in working with lung infection models (explained further in Chapter 4) another method of localized delivery had to be chosen. For this purpose subcutaneous (SQ) injection was chosen and the biodistribution was visualized using SPECT/CT.

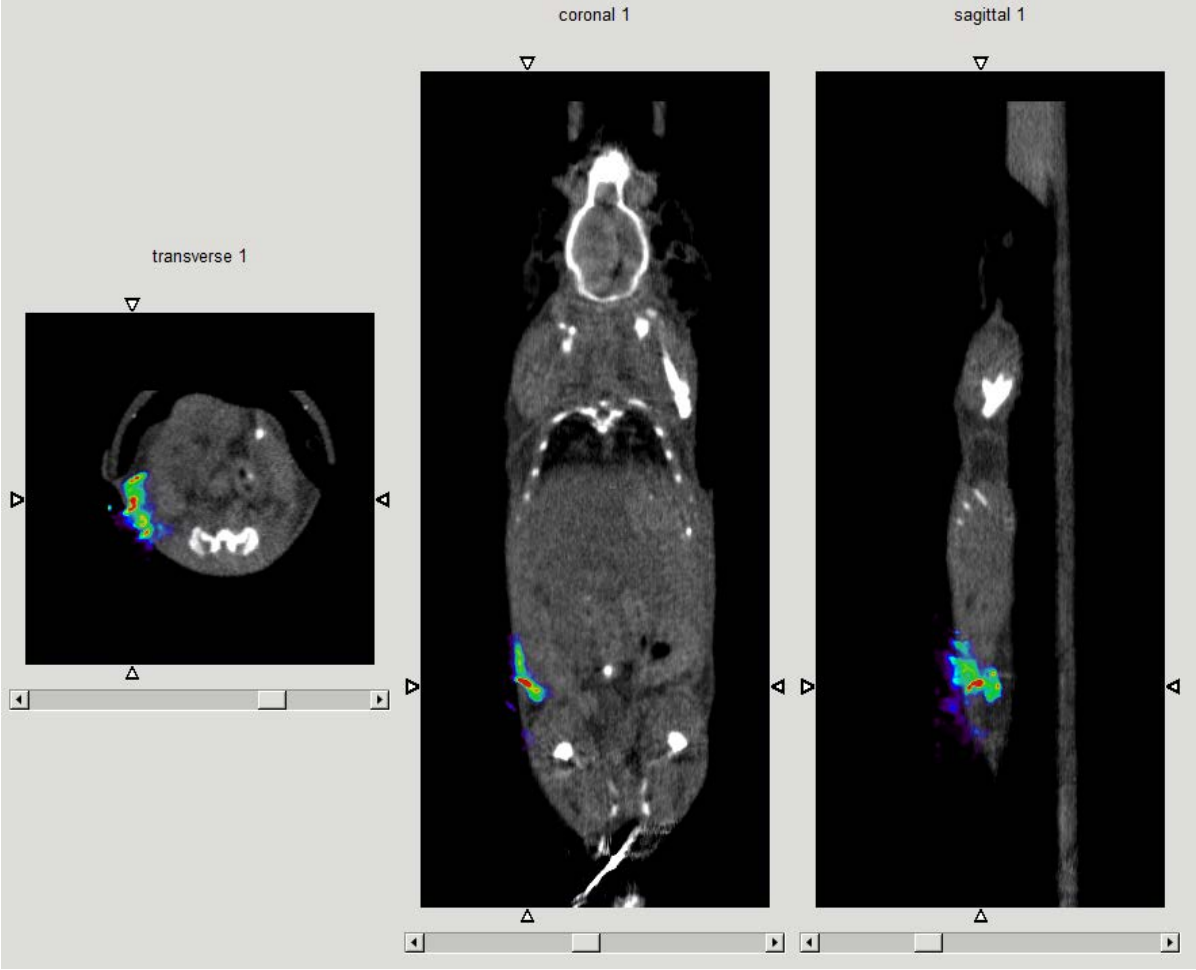

Figure 48: SPECT/CT image of mouse 1 10 minutes post-injection of ^{123}I-L-AgNPs

The subcutaneous (SQ) injection of the ^{123}I labeled L-AgNPs shows that all of the injected activity is found at the injection site immediately after injection. The SPECT/CT image of mouse 1 is shown as a representative image for this early imaging time point (Figure 48).

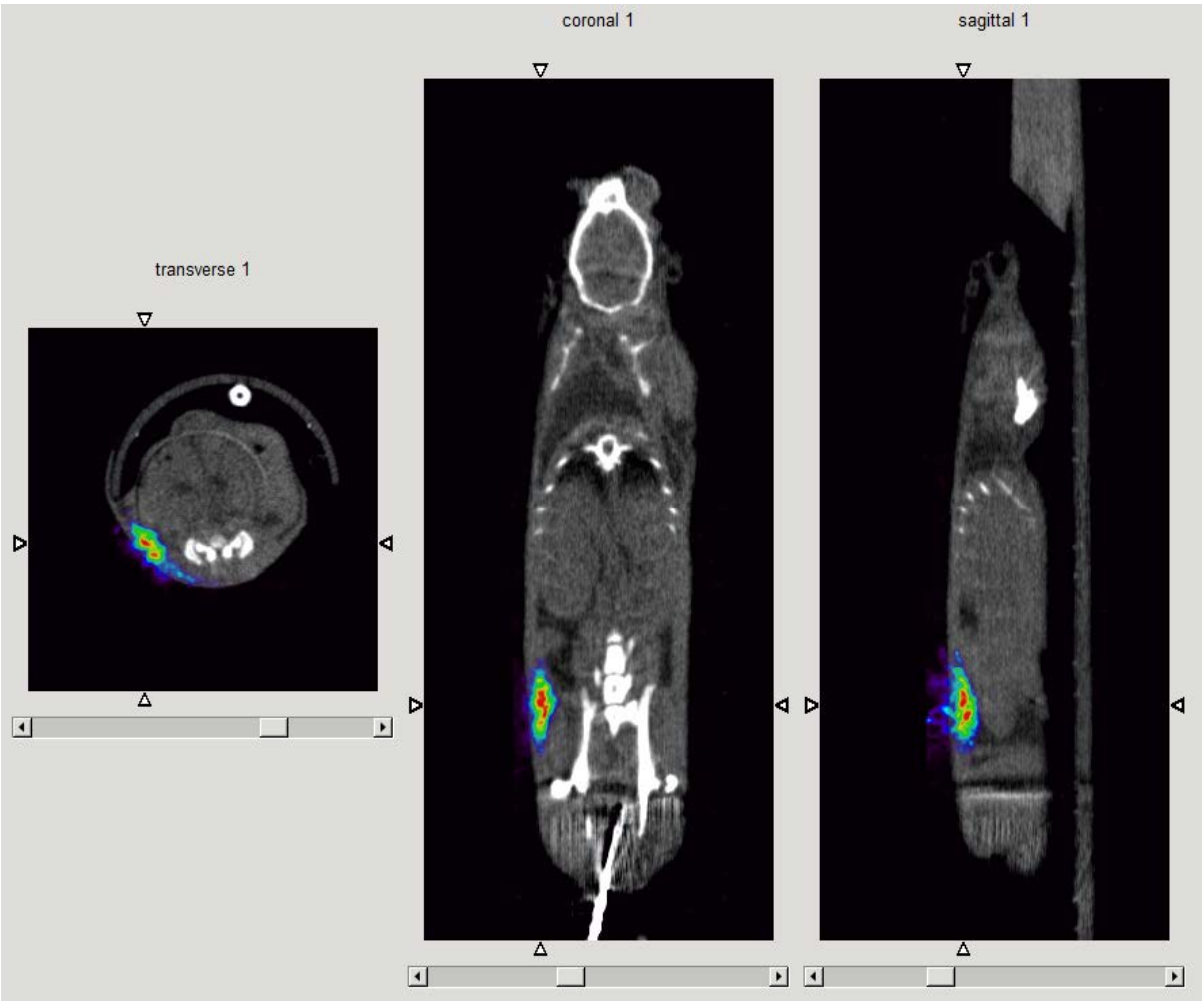

Figure 49: SPECT/CT image of mouse 4 (control mouse) 10 minutes post-injection of Na-^{123}I showing injection site

For the control mouse, all of the injected activity remained in the injection site immediately following the SQ injection of Na-^{123}I. It is important to perform this control using free Na-^{123}I for comparison with the ^{123}I-labeled L-AgNPs to determine if the ^{123}I that has been conjugated to the lignin becomes detached from the particles. It is also important to include this control to show how the presence of the L-AgNPs alters the biodistribution of an injected substance when it is bound to NPs versus contained in a free solution.

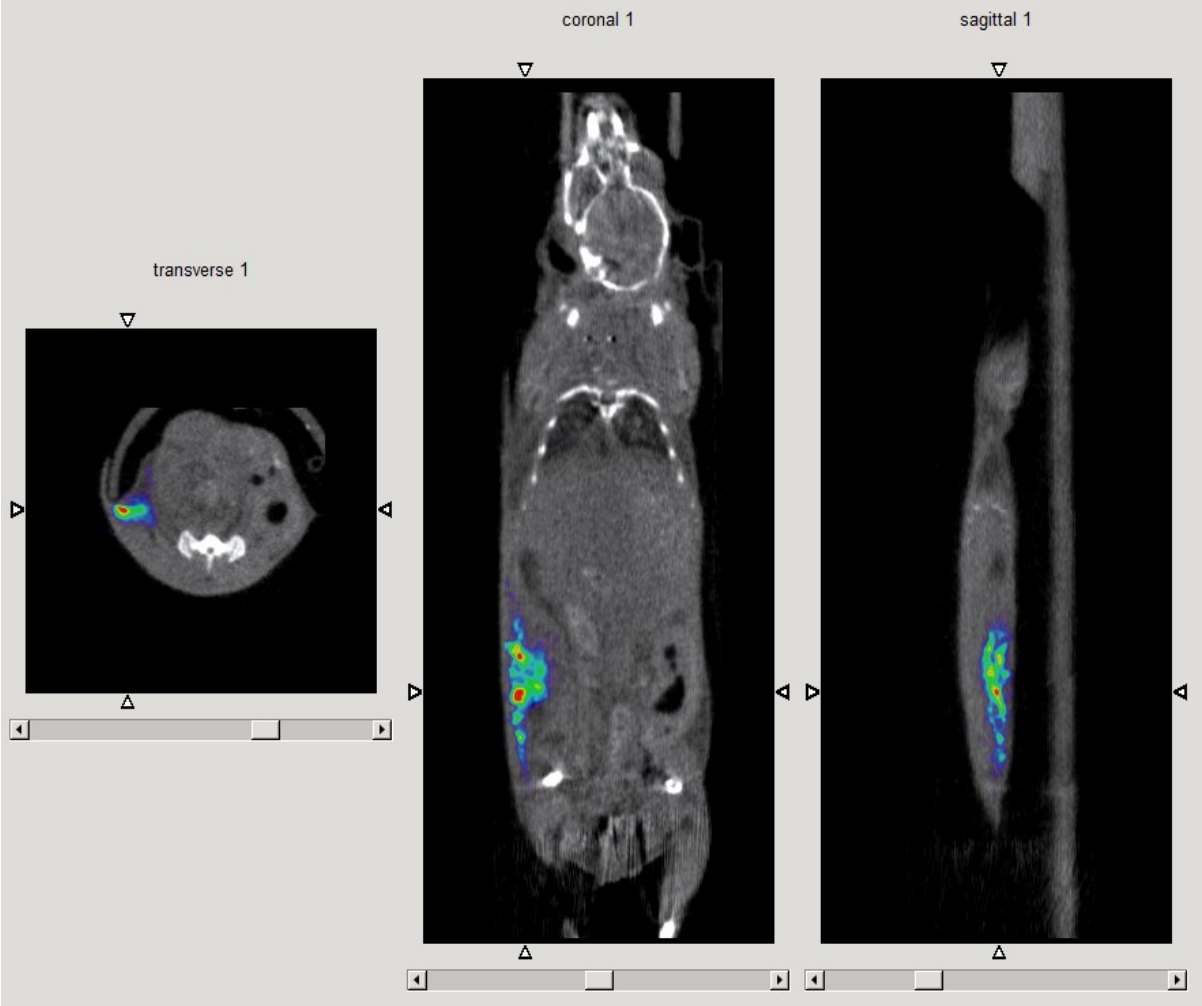

Figure 50: SPECT/CT image of mouse 1 2 hours post-injection of ^{123}I-L-AgNPs

At 2 hours post-injection the ^{123}I-labeled L-AgNPs have begun to spread out locally, but are mainly contained within the area of injection. No activity has been distributed to the liver, bladder, or thyroid meaning that all of the ^{123}I has remained conjugated to the lignin.

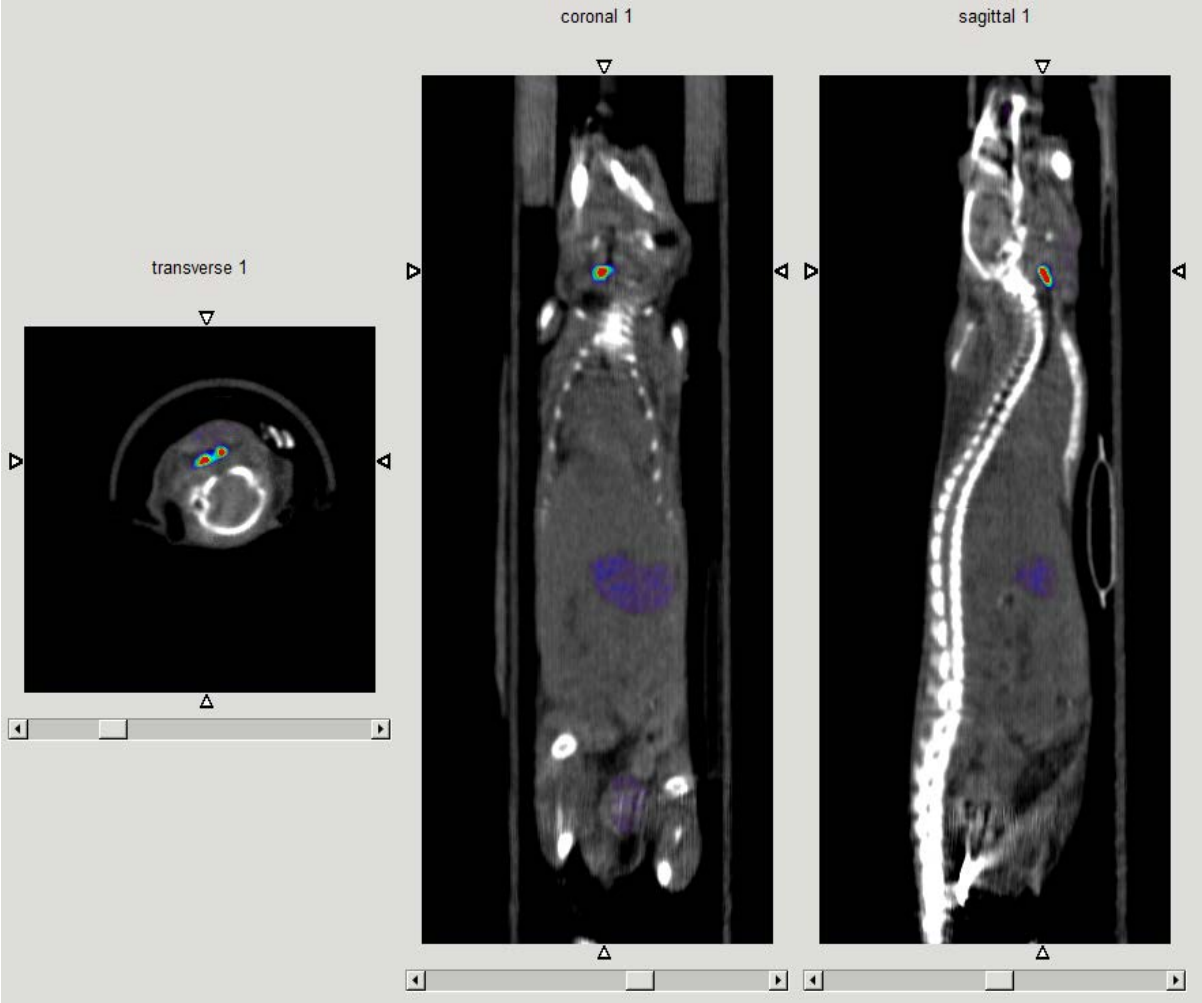

Figure 51: SPECT/CT image of mouse 4 2 hours post-injection of Na-^{123}I showing accumulation in the liver, bladder, and thyroid

At 2 hours post-injection of Na-^{123}I there was no remaining activity in the injection site. The free ^{123}I was quickly taken up by the thyroid and liver and excreted through the bladder. This is in stark comparison to the ^{123}I-labeled L-AgNPs which are almost exclusively contained within the injection area at 2 hours post-injection (Figure 50).

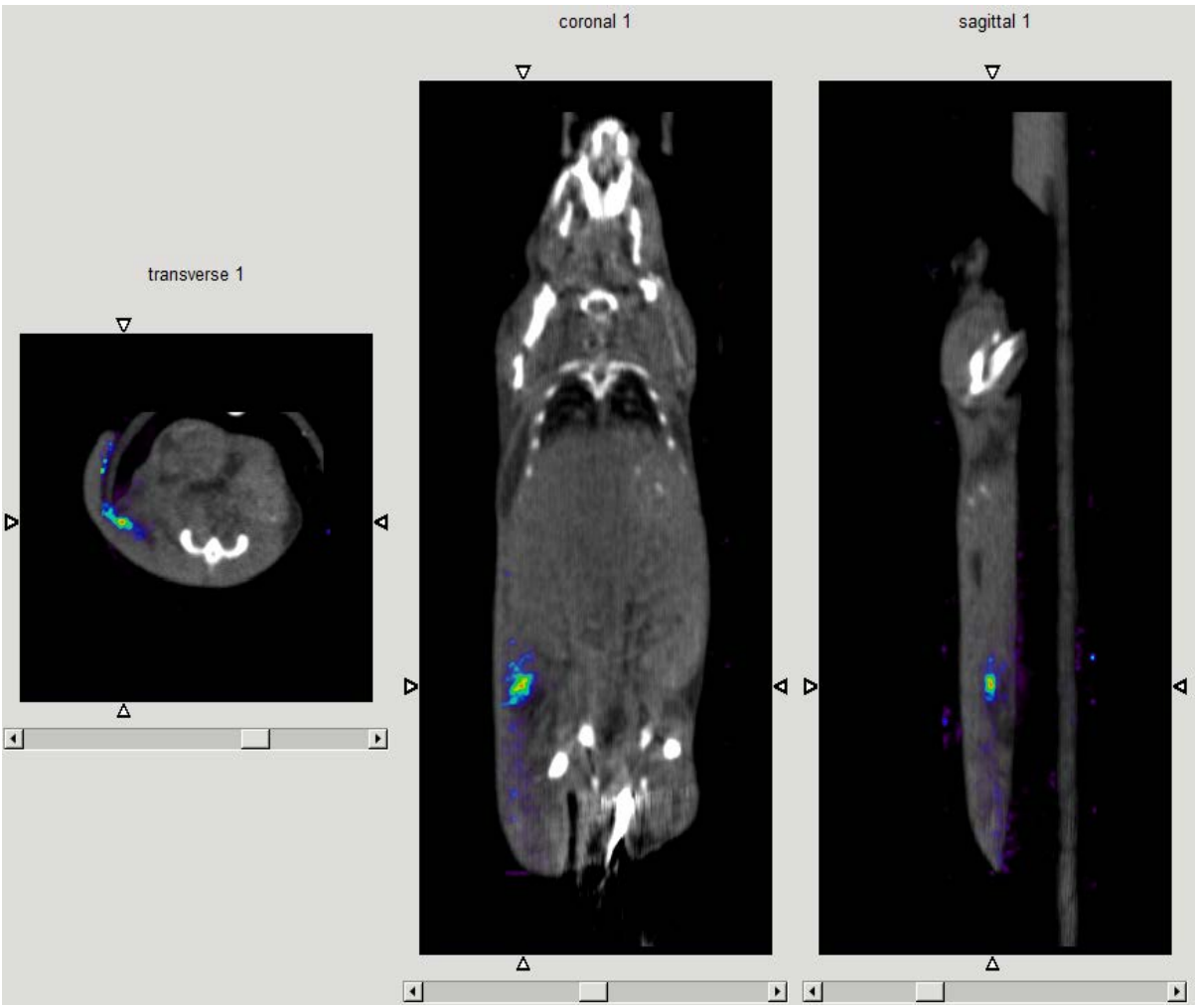

Figure 52: SPECT/CT image of mouse 1 24 hours post-injection of ^{123}I-L-AgNPs showing injection site

At 24 hours post-injection a significant amount of activity was still present in the injection site of the mice injected with the ^{123}I-labeled L-AgNPs.

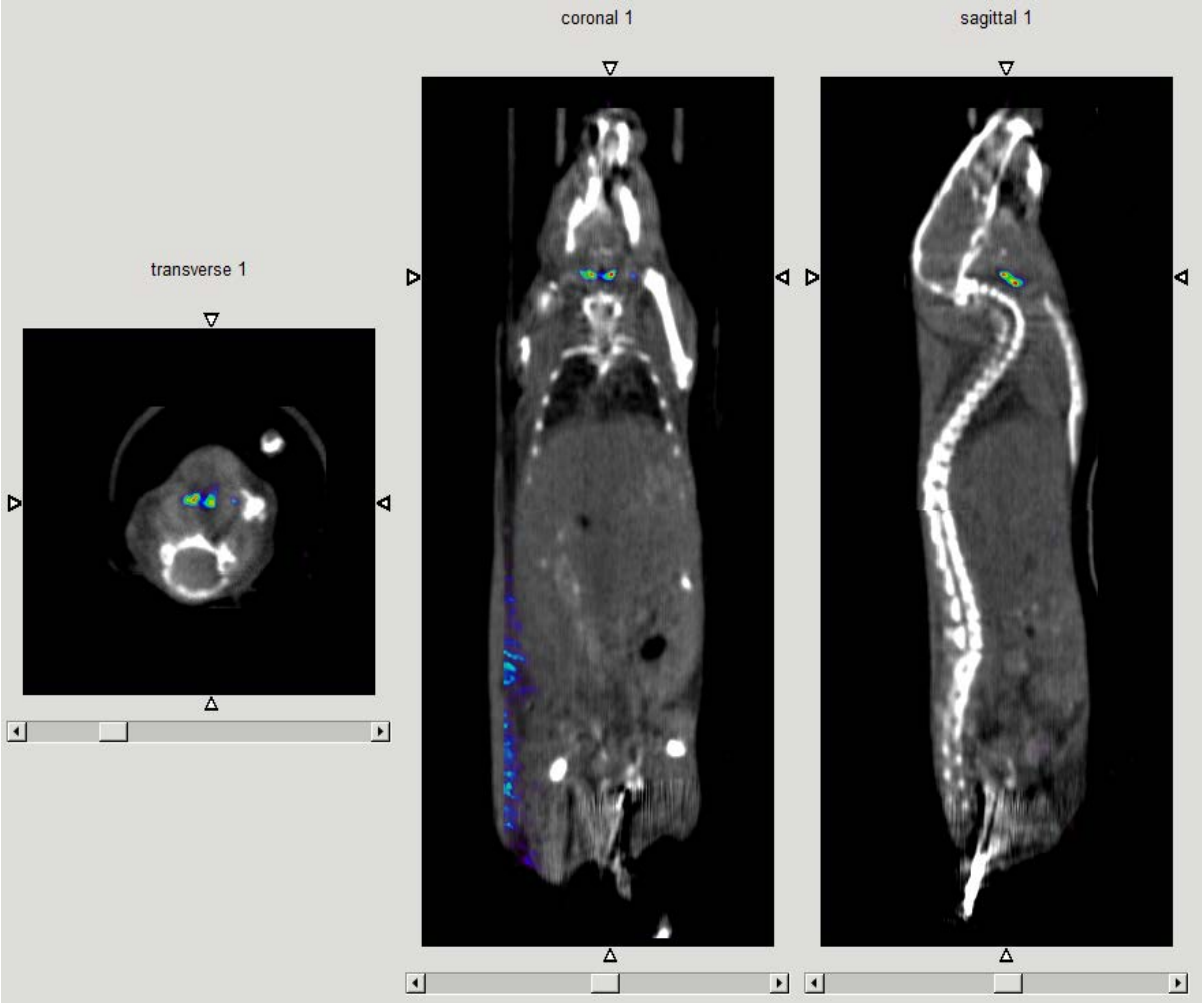

Figure 53: SPECT/CT image of mouse 1 24 hours post-injection of 123I-L-AgNPs showing thyroid uptake

At 24 hours post-injection significant radioactivity was seen in the thyroid of all animals injected with the ^{123}I labeled L-AgNPs. This could be due to the biodegradation of the lignin which would release free ^{123}I and subsequently accumulate in the thyroid. Biodegradation of lignin has been shown with multiple different heme peroxidases, so it is possible that heme peroxidases present in neutrophils and macrophages slightly degraded the lignin resulting in the release of free ^{123}I [210]. Full biodegradation of lignin is extremely difficult so it is unlikely that the lignin is fully biodegraded. Additionally, small amounts of catabolic dehalogenation with uptake in the thyroid has been seen in AgNPs conjugated with ^{125}I and administered intravenously [154].

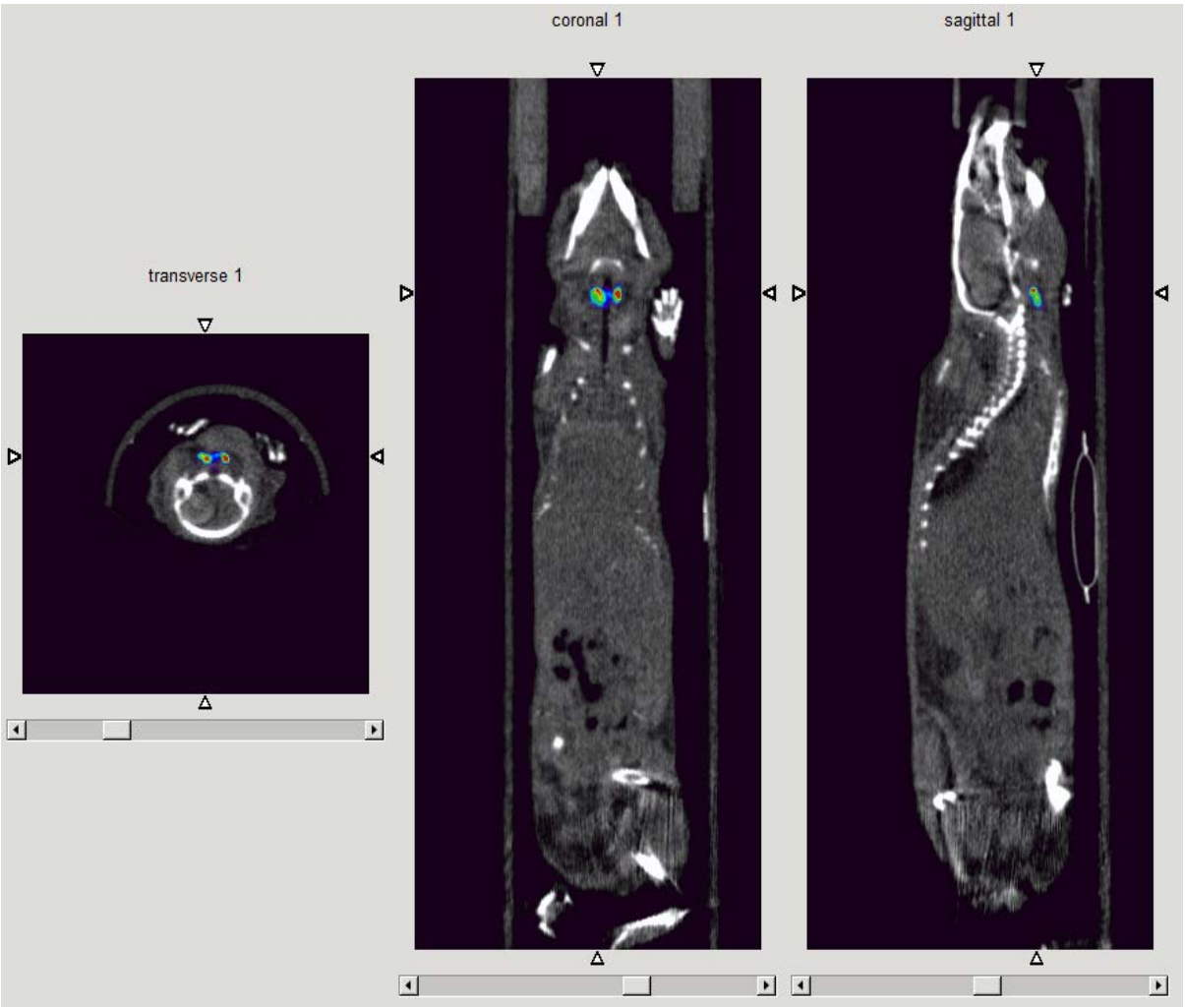

Figure 54 SPECT/CT image of mouse 4 24 hours post-injection of Na-^{123}I showing thyroid uptake

At 24 hours post-injection for the control mouse all of the injected activity was present in the thyroid (Figure 54). There was no remaining activity in the injection site or in the liver or bladder.

From the SPECT/CT images it is clear that when the L-AgNPs are injected SQ they remain in the injection site with minimal translocation up to 24 hours. It is also clear that between 2 hours and 24 hours the lignin begins to be biodegraded or the bonds between the iodine and the lignin begin to break which released free ^{123}I as evident by the thyroid uptake seen in Figure 53. This can be easily compared to the distribution of the subcutaneously injected Na-^{123}I which shows rapid translocation and uptake in the thyroid with no activity remaining in the injection site at 2 hours post-injection.

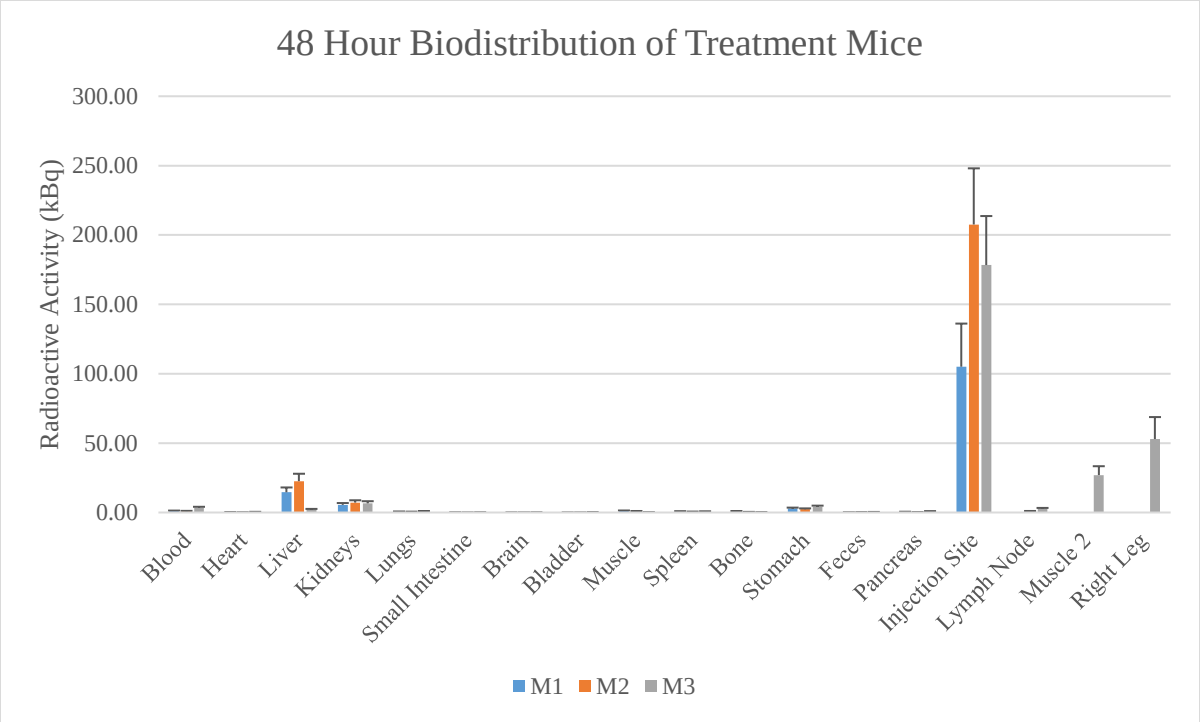

Figure 55: Biodistribution of 16.65 MBq of ^{123}I-labeled L-AgNPs in mice 48 h after subcutaneous injection given as average activity ± S.D. (n = 3).

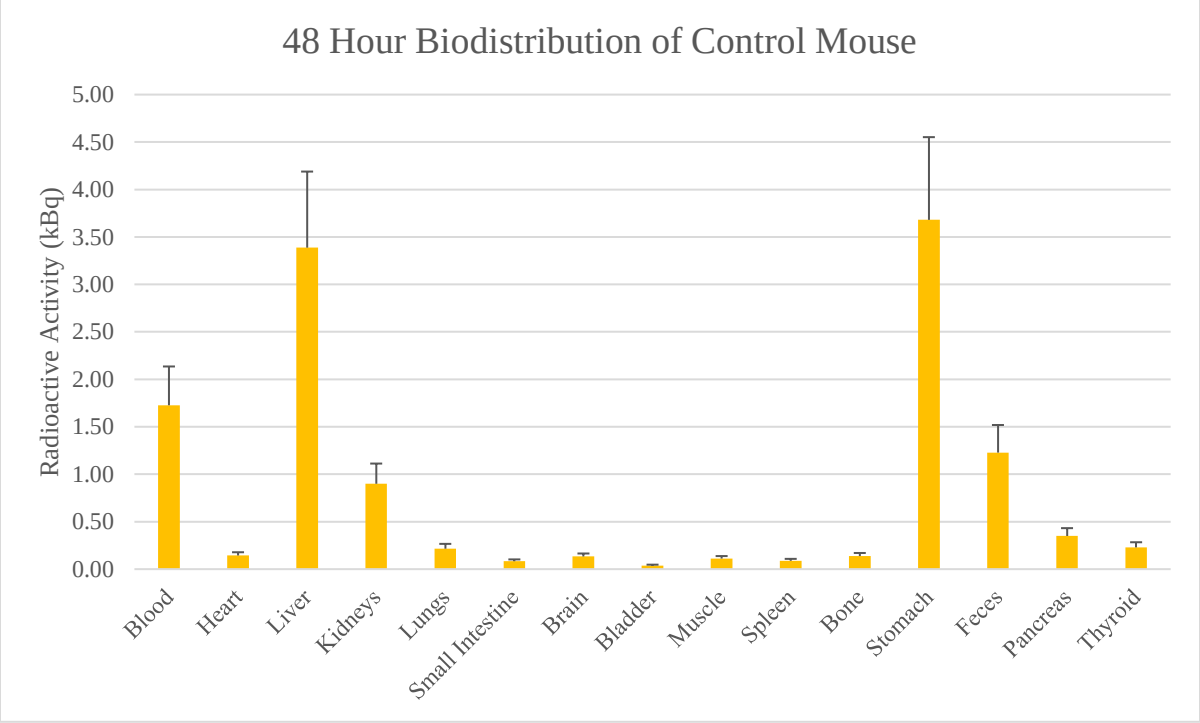

Figure 56: Biodistribution of 22.2 MBq of free Na-^{123}I in mice 48 h after subcutaneous injection given as average activity ± S.D. (n=1)

It is likely that the majority of the injected ^{123}I-labeled L-AgNPs remain in the injection site at 48 hours post-injection (Figure 55). The results for mouse 3 are slightly skewed because the injection was performed partially intramuscularly. This was identified in the SPECT/CT images and confirmed by the activity present in the right leg and muscle tissue taken from the right leg area (muscle 2). It is worth noting that there is slight uptake in the liver and kidneys at 48 hours post-injection. This finding could be due to some amount of translocation of L-AgNPs after subcutaneous injection. This theory is in agreement with the work published by Tang et al., with further confirmation that the silver translocating to other organs could be actual L-AgNPs, not just silver ions. Since the SPECT/CT images show that some free ^{123}I is taken up by the thyroid at 24 hours post-injection it is possible that the activity present in the liver and kidneys is due to excretion of free ^{123}I, not the entire ^{123}I-labeled L-AgNPs. Additionally, the 48 hour biodistribution of the control mouse that received Na-^{123}I (Figure 56) shows significant amounts of radioactivity in the stomach, liver, and kidneys. The liver and kidney activity of the L-AgNP treated mice could thus also be due to the presence of free ^{123}I. However, only tracking ^{123}I does not clearly answer if the lignin coating separates from the silver and maybe translocates to other areas of the body. Further in vivo testing with ^{111}Ag is thus necessary. Additional histological analyses as well as ICP-MS should be done in the future to further elucidate the particles' detailed biodistribution and fate.

While the control mouse initially received about 22.2 MBq of Na-^{123}I, essentially all of it has been excreted with a total of only 12.45 kBq (0.06% ID) of activity remaining in the examined organs. This amount of activity is very minimal when compared to the amounts remaining in the mice treated with ^{123}I-labeled L-AgNPs which indicates that the ^{123}I contained in the L-AgNPs is bound to the particles and does not circulate as free Na-^{123}I. The SPECT/CT images of the control mouse indicate that the injected activity is either quickly taken up by the thyroid or cleared to the liver and excreted through the bladder. The activity remains in the thyroid at 24 hours post-injection. It is interesting that in the control mouse at 48 hours post-injection the majority of the remaining activity is present in the stomach, liver, and blood while showing very small amounts of activity in the thyroid. This could be a potential error due to a small sample size or could only be seen due to the very small amounts of activity still present.

Iodine was chosen as the primary element for radioactive tagging of lignin because of the abundant phenolic aromatic groups present in the structure of lignin, and because iodine can be easily conjugated to phenolic aromatics by a simple electrophilic substitution reaction without the presence of any catalyst. Other iodine radioisotopes could have been chosen for the labeling of these L-AgNPs. For example, ^{125}I has been previously used to label AgNPs with high labeling efficiency for SPECT/CT imaging [154]. However, ^{125}I has a half-life of 59.4 days which is significantly longer than that of ^{123}I (13.22 hours) which poses significant issues for disposal of all radioactive materials. Additionally, in the study utilizing ^{125}I for the labeling of AgNPs uptake was seen in the thyroid after 24 hours so there were no advantages to using ^{125}I instead of ^{123}I for the labeling of the L-AgNPs.

3.3.4 Radiolabeling L-AgNPs with ^{111}Ag

When the *in vivo* biodistribution of AgNPs is determined it is generally carried out by methods where the NPs themselves are not directly measured. ICP-MS methods do not differentiate between AgNPs and silver ions, and the SPECT/CT imaging procedures generally track a secondary radioisotope which has been conjugated to the coating of the AgNP. To circumvent this problem I have radiolabeled the L-AgNPs using a silver isotope so that the SPECT/CT imaging will be directly tracking silver instead of tracking a secondary isotope.

Table 8: Labeling efficiency of producing L-AgNPs with $AgNO_3$ doped with ^{111}Ag

Starting Activity (MBq)	Ending Activity (MBq)	Labeling Efficiency
15.36	7.585	49.38%

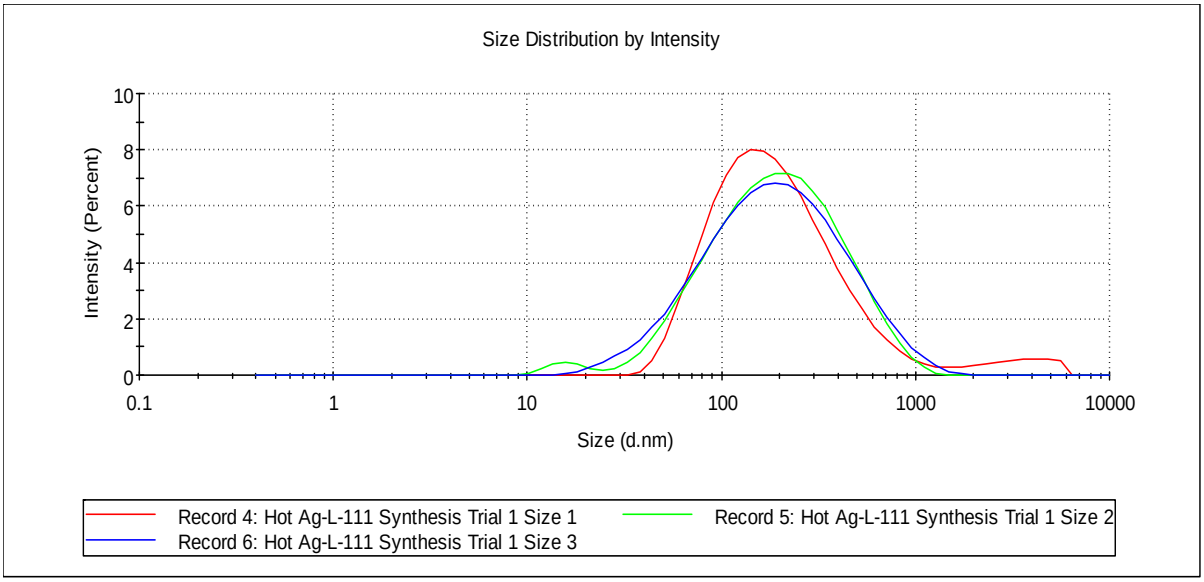

Figure 57: DLS size analysis of L-AgNPs produced by 72-hour heating aerobic synthesis using ^{111}Ag-doped $AgNO_3$

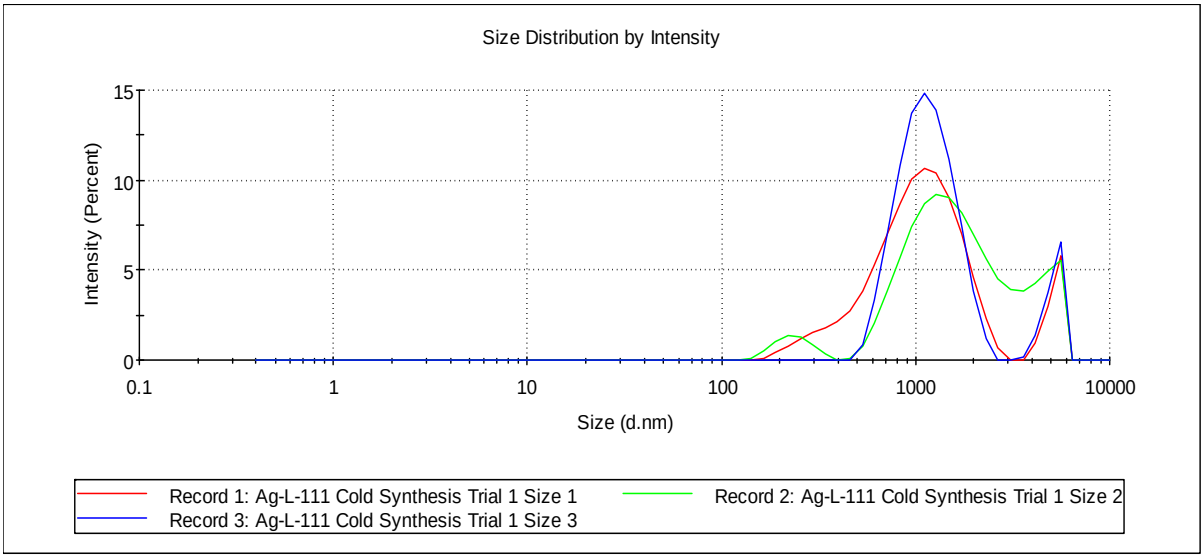

Figure 58: DLS size analysis of L-AgNPs produced by 72-hour heating aerobic cold synthesis parallel to ^{111}Ag synthesis (Figure 57)

While a significantly high radioactive labeling efficiency was achieved, conditions were not equal between the hot and cold synthesis methods of the L-AgNPs labeled with ^{111}Ag as evident by their drastically different size distributions (Table 8, Figure 57 and Figure 58). Likely due to pH differences, the particles produced by the ^{111}Ag-doped synthesis method are almost triple the size of those produced by the 72-hour synthesis method. ^{111}Ag was received from the University of Missouri Research Reactor Center (MURR) in the form of dried silver nitrate ($AgNO_3$).

Unfortunately, the ^{111}Ag that we received contained a significant amount of the solvent impregnated resin present from the separation process, and was very difficult to purify. Eventually the ^{111}Ag was purified, but it had to be resuspended in 6 M HNO_3 and hydrogen peroxide which likely altered the pH of the system and caused particles to form which were significantly larger than those formed by the usual 72-hour synthesis method. It is also possible that the size differences are due to not decreasing the pH of the lignin solution to 5.5 using HCl before processing because XRD analysis has already shown that there is some production of AgCl in the finished particles. Additionally, the presence of hydrogen peroxide could have caused significant problems during synthesis because hydrogen peroxide is known to degrade organic materials like aromatics and halogenated compounds, so it is possible that the addition of hydrogen peroxide could have degraded the lignin in solution further altering the synthesis conditions [211].

3.3.5 SPECT/CT imaging of ^{111}Ag

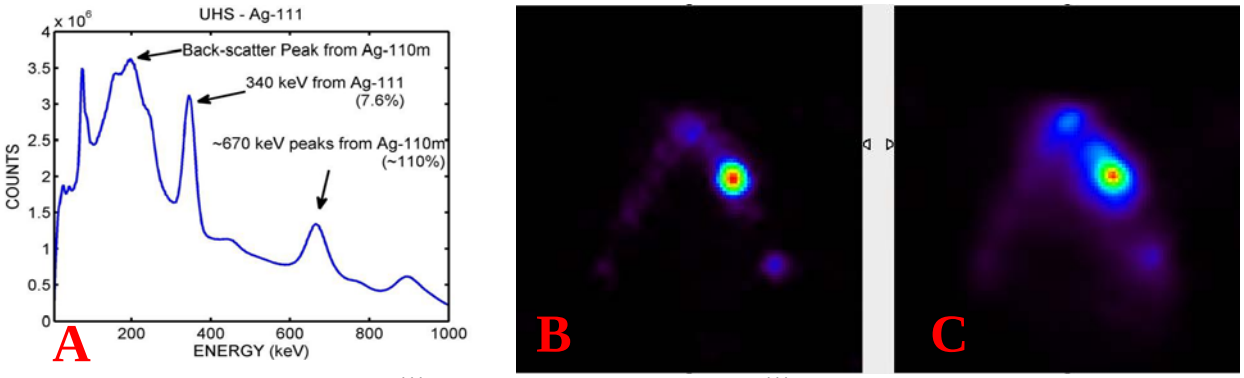

Figure 59: Energy spectrum of ^{111}Ag (A) and SPECT images of ^{111}Ag taken in high-energy ultra-high resolution (HEUHR) collimator (B), ultra-high sensitivity (UHS) collimator (C)

The energy spectrum of the ^{111}Ag received from MURR (Figure 59A) shows the presences of ^{111}Ag along with a small amount of ^{110m}Ag which is a long-lived silver radioisotope ($t_{1/2}$ = 249.8 days) [52]. Due to the presence of this impurity extreme caution was used when handling the ^{111}Ag because any contamination would have resulted in the contaminated surface remaining radioactive for a very long time.

Silver-111 was detected reliably on our SPECT/CT machine with both a high-resolution collimator (Figure 59B) and a high sensitivity collimator (Figure 59C). This means that there is potential for

^{111}Ag to be used as a SPECT isotope, despite its low gamma ray abundance of 1.3% at 245 keV and 6.7% at 342 keV.

AgNP formation was observed utilizing the 72-hour aerobic synthesis method with $AgNO_3$ doped with ^{111}Ag (although the particles were significantly larger than desired). This means that ^{111}Ag can potentially be used to track AgNPs *in vivo* by SPECT/CT imaging, which has not been shown, to date. Of all silver radioisotopes the only one that emits gamma rays in the SPECT range is ^{111}Ag. Further studies exploring the *in vivo* fate of the silver core of the L-AgNPs are planned in the future utilizing ^{111}Ag as the radiotracer.

3.4 Conclusion

Methods were developed to successfully radioactively label the L-AgNPs with both ^{123}I and ^{111}Ag. The radiolabeling of synthesized L-AgNPs with ^{123}I is possible with very high efficiency, but causes significant particle aggregation. Therefore, the lignin should be labeled with ^{123}I and then L-AgNPs should be synthesized by microwave-assisted synthesis because very stable particles are produced although labeling efficiency is slightly lower.

The particles produced with ^{111}Ag doped $AgNO_3$ were significantly larger than the particles that have been produced by the general 72-hour heating synthesis method. This is likely due to issues related to pH control and the addition of hydrogen peroxide. Although ^{111}Ag availability is an issue, further studies should be explored using the microwave-assisted synthesis method to produce ^{111}Ag-labeled L-AgNPs.

Biodistribution studies were conducted with ^{123}I showing that L-AgNPs can be administered directly to the lungs with minimal deposition in the mouth or stomach. Biodistribution studies conducted after subcutaneous injection of ^{123}I-labeled L-AgNPs show that the majority of the injected dose stays directly in the injection site until 24 hours post-injection when some amount of free ^{123}I accumulates in the thyroid. However, further experiments including biodistributions with ^{111}Ag and histology or ICP-MS of other organs should be performed to confirm that the lignin remains conjugated to the silver and to determine if the silver translocates to other organs. At 48

hours post-injection some amount of activity can be seen in the liver, kidneys, and stomach which is likely due to the presence and translocation of free ^{123}I.

To our knowledge, imaging ^{111}Ag by SPECT/CT is a first. There is potential for the use of this silver radioisotope to determine the biodistribution of AgNPs in the future.

Chapter 4: Antimicrobial Activity *In Vitro* and *In Vivo*

Extensive literature has been published concerning the antimicrobial activity of AgNPs *in vitro*, but few studies explore the *in vivo* antimicrobial activity. In this chapter, L-AgNPs were tested against multidrug resistant (MDR) bacterial strains both *in vitro* and *in vivo* to determine their antimicrobial activity. It is important to perform the *in vitro* antimicrobial tests in physiological broth in order to ensure that the results will be accurate for transferring to *in vivo* models. Antimicrobial L-AgNPs would be especially useful for the treatment of MDR lung infections. However, an *in vivo* model for this disease is extremely difficult to perform. For this reason, we chose to perform a cutaneous infection (abscess) model instead. The *in vivo* abscess model was performed in adherence to ACC protocol A14-0363 and has been validated as a chronic infection model [212].

4.1 Hypothesis and Objectives

I hypothesize that the L-AgNPs will show excellent antimicrobial behavior both *in vitro* and *in vivo* against MDR and non-MDR bacterial strains, and that they will not be toxic. To examine this hypothesis, the following objectives were investigated:

(1) The *in vitro* antimicrobial activity was determined by broth dilution tests against clinical isolate MDR bacterial strains, and the results are presented as the minimum inhibitory concentration (MIC) (concentration at which no bacterial growth is observed).

(2) The cytotoxicity was determined by MTT assay of human-derived monocyte (THP-1) cells *in vitro* and the biocompatibility was examined *in vivo* by determining if inflammation or necrotic tissue was present after subcutaneous injection.

(2) The *in vivo* antimicrobial testing was determined by treatment of a biofilm forming abscess after administration of MDR bacteria and L-AgNPs. The results of bacterial load and abscess size are presented in this chapter.

The *in vitro* antimicrobial effects of the particles are discussed including the differences in effect of the particles produced by the 72-hour heating method and those produced by the microwave-assisted synthesis method. The *in vivo* effectivity and toxicity is also discussed.

4.2 Antimicrobial Testing Methods

4.2.1 *In Vitro* Antimicrobial Testing Method

The *in vitro* antimicrobial testing is very important to determine how effective the produced particles are at killing bacteria before they are used in an *in vivo* setting. It is also very important to use biological media for the *in vitro* testing so that the results translate better into an *in vivo* setting. For the *in vitro* antimicrobial testing broth was first added to each well of a 96-well plate along with appropriate amounts of NPs. Next 5 µL of bacteria was added to each well and the plate was placed in 37°C shaker overnight. The next day the 96-well plate was observed for bacterial growth, determined by which wells were turbid or clear. If the well was clear then the corresponding NP concentration was determined to be the minimum inhibitory concentration (MIC).

4.2.2 *In Vitro* Toxicity Testing Method (MTT Assay)

On the first day 100,000 THP-1 cells were seeded with 40 ng/mL propidium monoazide (PMA) into a flat-bottom 96-well plate to a final volume of 100 µL/well, and incubated at 37°C supplemented with 5% CO_2. On the second day the media was aspirated and replaced to remove PMA and leave only adhering cells. The NPs were added (after ultracentrifugation 67,600 × *g* for 30 min and supernatant replacement with 0.6% lignin solution) in varying concentrations to each well in triplicates. Three wells were left untreated as a negative control, 1 µL of Tween-20 was placed in three wells as a positive control, and the cells were incubated at 37°C overnight. On day three 10 µL of MTT (5 mg/mL in PBS) was added per well, incubated at 37°C for 4 hours, and formazan crystals were dissolved with 100 µL/well of solubilization solution (20% w/v SDS added to a 50% DMF solution containing 2.5% acetic acid and 2.5% 1 M HCl). The cells were then incubated at 37°C overnight and the plate was read at 570 nm. Cell viability can be represented as the OD value compared to the untreated negative control.

4.2.3 *In Vivo* Cutaneous Infection (Abscess) Effectivity Model

The ideal infection model for the L-AgNPs would have been a lung infection model, but this model is extremely difficult and there are very few laboratories practicing it currently. For this reason a cutaneous infection model caused by MDR bacteria was chosen instead. To begin the experiment the fur on the back of each CD-1 female mouse was removed by shaving. Bacteria were grown to an OD_{600} of 1.0 in double yeast tryptone (dYT) broth then washed with sterile PBS and resuspended at desired concentration depending on strain (*P. aeruginosa* or *S. aureus*). L-AgNPs produced by microwave-assisted synthesis with 20 mg/mL $AgNO_3$ (as described in 2.2.4) were concentrated to 10 and 100 mg/mL in PBS using a 10 kDa microconcentration filter, and resuspended in PBS to avoid any toxicity issues surrounding the pH of the solution. Next 50 µL of bacteria were injected subcutaneously into the right side of the dorsum underneath the thin skeletal muscle. At 1 hour post-injection saline, 1% lignin in PBS, or L-AgNPs at an appropriate concentration in PBS were injected subcutaneously into the infected area. The progression of the abscess was monitored daily, and at three days post-injection the mice were euthanized with carbon dioxide and then cervically dislocated. Abscess size was measured with calipers without considering swelling and inflammation. Skin abscesses (including all accumulated pus) were excised and homogenized in sterile PBS using a Mini-Beadbeater-96 cell disrupter (BioSpec Products) for 5 min and bacterial counts (in CFU) were determined by serial dilution and plating overnight at 37°C.

4.2.4 *In Vivo* Cutaneous Toxicity Model

The L-AgNPs had to be tested for toxicity in the *in vivo* model without the presence of any bacteria before they could be used in the efficacy study. Toxicity was determined as the presence of any inflammation or necrotic tissue in the injection site. For the toxicity experiment, the fur on the back of each CD-1 female mouse was removed by shaving. L-AgNPs were produced using the microwave synthesis method with 20 mg/mL $AgNO_3$ (as described in 2.2.4) and concentrated to 100, 80, 60, 40, and 20 mg/mL in PBS using a 10 kDa microconcentration filter. Then 50 µL of

1% lignin in PBS, or L-AgNPs at an appropriate concentration in PBS were injected subcutaneously into the right side of the dorsum underneath the thin skeletal muscle. At three days post-injection the mice were euthanized with carbon dioxide and then cervically dislocated. The injection site was excised and visually observed for signs of inflammation or necrotic tissue to determine toxicity.

4.3 Results and Discussion

4.3.1 *In Vitro* Antimicrobial Testing by Broth Dilution

In order to determine how effective the L-AgNPs were at treating multidrug resistant (MDR) bacteria *in vitro* antimicrobial testing had to be performed. When performing these tests it is important to use biological media instead of water so that the results will be more easily transferrable to *in vivo* testing where the presence of additional salts proteins can alter antimicrobial activity. For the *in vitro* antimicrobial testing several different Gram-positive and Gram-negative MDR and ATCC bacterial strains were chosen to determine the antimicrobial efficiency of the produced L-AgNPs against a wide range of bacteria.

Table 9: Results of antimicrobial testing of four sets of L-AgNPs against 5 clinical isolate MDR bacterial strains (MW designates microwave-assisted synthesis)

Bacterial Strain	Minimum Inhibitory Concentration (μg/mL)			
	MW 110°C	**MW 120°C**	**Aerobic 019**	**Anaerobic 017**
***S. aureus* 700**	2.5	2.5	2.5	2.5
***P. aeruginosa* 205**	5.0	2.5	2.5	2.5
***K. pneumoniae* 124**	5.0	5.0	2.5	2.5
***A. baumannii* 808**	≤ 1.0	≤ 1.0	≤ 1.0	≤ 1.0
***E. casseliflavus* 1**	≤ 1.0	2.5	≤ 1.0	≤ 1.0

The L-AgNPs produced both by 72-hour heating synthesis and by microwave-assisted synthesis showed excellent antimicrobial action against all studied clinical isolate MDR bacterial strains (Table 9). These strains are particularly dangerous because they have been identified as very drug-resistant and have been isolated as human pathogens from a clinical setting. The bacterial strains

chosen for these test represent an array of very difficult to treat Gram-positive and Gram-negative strains.

Antimicrobial testing was continued only with the L-AgNPs produced by aerobic 72-hour heating synthesis because the reported MIC was exactly the same for the particles produced by 72-hour heating anaerobic synthesis, and particle production was significantly less complicated with aerobic synthesis method.

Table 10: Results of antimicrobial testing of four sets of L-AgNPs against 4 ATCC bacterial strains (MW designates microwave-assisted synthesis)

Bacterial Strain	Minimum Inhibitory Concentration (μg/mL)		
	MW 110°C	**MW 120°C**	**Aerobic 019**
***S. aureus* MRSA**	2.5	2.5	2.5
P. aeruginosa	≤ 1.0	≤ 1.0	≤ 1.0
A. baumannii	≤ 1.0	≤ 1.0	≤ 1.0
E. coli	2.5	2.5	2.5

The L-AgNPs showed excellent antimicrobial activity against both Gram-positive and Gram-negative MDR bacterial strains, so it was necessary to test the particles against some non-resistant bacterial strains as well. When tested against a variety of Gram-positive and Gram-negative ATCC bacterial strains, the L-AgNPs showed very similar antimicrobial activity as when tested against the MDR strains. This similarity shows that the L-AgNPs are capable of antimicrobial action regardless of bacterial drug resistance. The L-AgNPs were then tested against the biofilm-forming MDR bacterial strains used in the *in vivo* cutaneous infection (abscess) model to determine the required concentration for transferring from the *in vitro* model to the *in vivo* model (Table 11).

Table 11: Results of *in vitro* antimicrobial testing by broth dilution of L-AgNPs against bacterial strains used in the abscess model

Bacterial Strain	Minimum Inhibitory Concentration (µg/mL)		
	MW 110°C	**MW 120°C**	**Aerobic 019**
***S. aureus* LAC**	2.5	5.0	2.5
***P. aeruginosa* LESB58**	2.5	2.5	2.5

All produced particles show excellent antimicrobial behavior *in vitro* against all 5 Gram-negative and Gram-positive clinical isolate MDR bacterial strains (Table 9). The MIC was exactly the same for particles produced by 72-hour heating aerobic or anaerobic synthesis methods when administered to the 5 clinical isolate MDR bacterial strains, so antimicrobial testing was only continued with the particles produced by aerobic synthesis method. This result is likely due to the fact that the anaerobic and aerobic synthesis methods produce L-AgNPs with similar size distributions and chemical composition.

The particles produced by microwave-assisted synthesis showed slightly higher MICs for only the *K. pneumoniae* 124, *P. aeruginosa* 205 (MW 110°C), and *E. casseliflavus* 1 (MW 120°C). In general the recorded MICs were almost identical for the L-AgNPs produced by microwave-assisted synthesis and the particles produced using the 72-hour heating methods when administered to the clinical isolate MDR bacterial strains (Table 9).

All particles showed identical antimicrobial action against the ATCC bacterial strains with MICs of 2.5 µg/mL or below (results can be seen in Table 10). The results of this testing are not necessarily expected because the L-AgNPs show the same MIC values when administered to *S. aureus* MRSA (Gram-positive) and *E. coli* (Gram-negative). It is generally expected that Gram-negative bacteria are more susceptible to AgNPs than Gram-positive bacteria due to differences in concentration of peptidoglycans at the bacterial cell wall and differences in cell wall thickness, so it is possible that the addition of the lignin cap facilitates the uptake of the L-AgNPs by Gram-positive bacteria [137]. The MIC values for the L-AgNPs when administered to the MDR bacterial strains used in the abscess model (Table 11) were almost identical for the particles produced by microwave-assisted synthesis and those produced by 72-hour heating, with only the MW 120°C

particles showing a slightly higher MIC when administered to the *S. aureus* LAC bacterial strain. This result is expected because *P. aeruginosa* LESB58 is a Gram-negative bacterial strain and AgNPs generally show greater toxicity to Gram-negative bacterial strains.

All the tested L-AgNPs show extremely high antimicrobial activity against both Gram-positive and Gram-negative bacteria which classifies them as a broad-spectrum antimicrobial agent. Additionally, when the MIC values are compared to other AgNPs produced using natural compounds (Table 4), it can be determined that the L-AgNPs show superior antimicrobial activity to almost any other compound. The mechanism of action of these L-AgNPs likely includes the attachment to the bacterial cellular membrane or cell wall which cause electron dense pits to form leading to increased permeability and cell death [135]. The increased permeability can allow additional silver ions to penetrate and produce radicals which cause significant DNA damage [145]. This result could potentially be due to the presence of AgCl NPs as well as AgNPs which provides an additional source of silver ions and thereby increasing the antimicrobial effects of these particles [202]. The superiority of the L-AgNPs could also be due to the lignin facilitating the binding of the L-AgNPs to the bacterial cell wall. Further studies should be conducted exploring the *in vivo* mechanisms by which the L-AgNPs exert toxicity on Gram-negative and Gram-positive bacterial strains.

4.3.2 *In Vitro* Toxicity

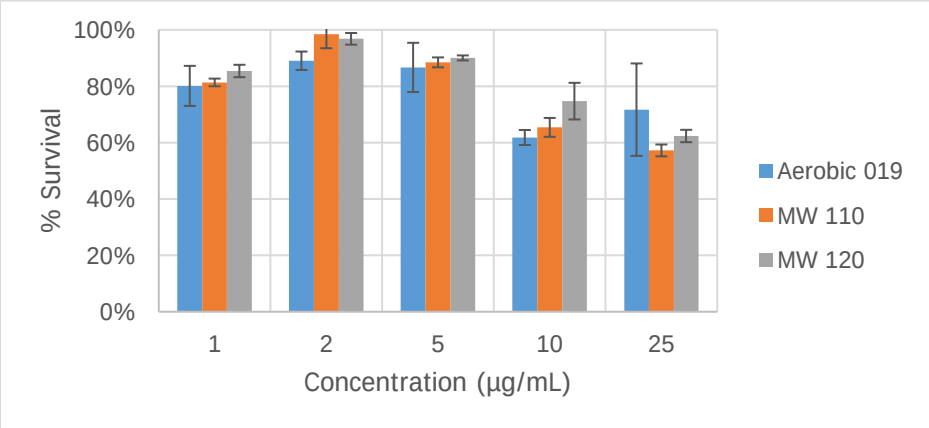

Figure 60: MTT toxicity assay results for particles produced by 72-hour aerobic synthesis and microwave-assisted synthesis

The results of the MTT toxicity assay against THP-1 cells in Figure 60 indicates that the L-AgNPs produced by either aerobic 72-hour heating synthesis or by microwave-assisted synthesis start to become slightly toxic at a concentration of 10 µg/mL. MTT assay on THP-1 cells is a useful approximation of the AgNPs' effect on the immune system as these cells contain significant numbers of macrophages and monocytes. The MTT assay determines the effect of a substance on the mitochondrial activity of a specific cell line, and AgNPs are known to inhibit mitochondrial function [90]. This is a fairly low concentration for toxicity. However, since the determined MICs for these particles are all below 5 µg/mL, this overall toxicity might be acceptable. In order to better determine the actual cytotoxicity of these particles more toxicity tests should be performed including methylene blue exclusion test and a life/death assay.

4.3.3 *In Vivo* Abscess Model Efficacy

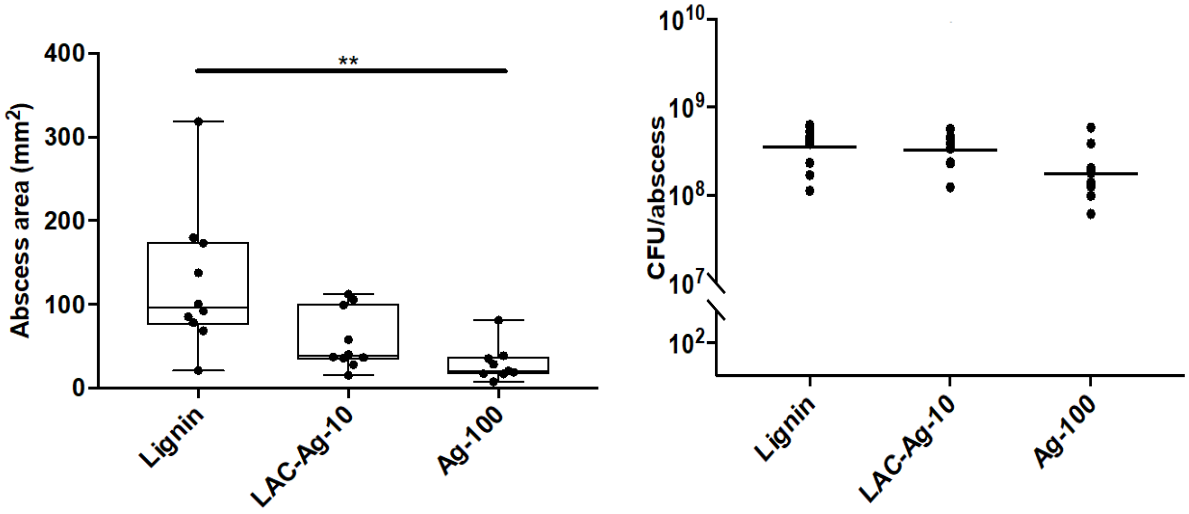

Figure 61: Efficacy of L-AgNPs produced by microwave-assisted synthesis using 20 mg/mL $AgNO_3$ (as described in 2.2.4) against *S. aureus* LAC strain *in vivo* at 10 and 100 mg/mL versus 1% lignin control displayed as reduction in abscess size (left) and reduction in bacterial colonization (right).

Statistical analysis by a two-sample, two-tailed Student's t-test assuming unequal variance shows a significant difference in abscess size between the 1% lignin control and L-AgNPs at both 10 mg/mL and 100 mg/mL ($p<0.05$) for the tested *S. aureus* LAC strain (Figure 61). However, no significant difference is observed in the bacterial load.

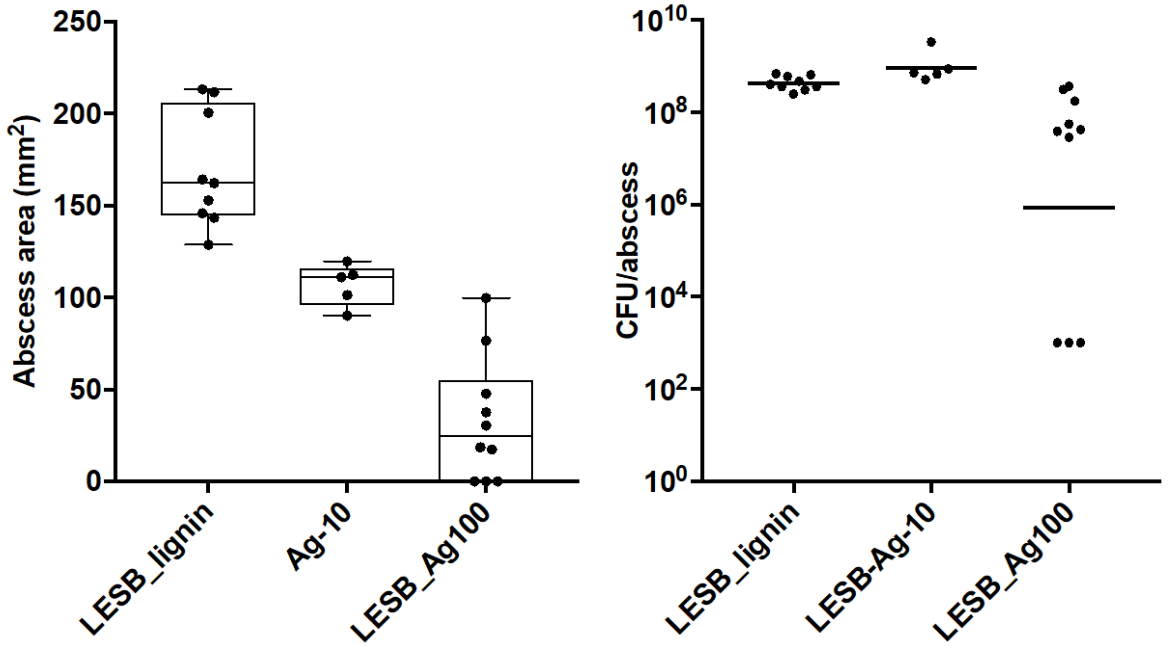

Figure 62: Efficacy of L-AgNPs produced by microwave-assisted synthesis using 20 mg/mL $AgNO_3$ (as described in 3.2.4) against *P. aeruginosa* LESB strain *in vivo* at 100 mg/mL versus 1% lignin control displayed as reduction in abscess size (left) and reduction in bacterial colonization (right)

Statistical analysis by a two-sample, two-tailed Student's t-test assuming unequal variance shows a significant decrease in abscess size between the 1% lignin control and the L-AgNPs applied at 10 mg/mL and 100 mg/mL ($p<0.001$) in the P. aeruginosa LESB strain (Figure 62). A significant difference is also seen between the 1% lignin control and the bacterial load in CFU when the L-AgNPs were applied at 100 mg/mL ($p<0.001$) but not at 10 mg/mL.

There is a significant concentration dependent decrease in abscess size (left) and a slight downward trend in bacterial load (right) when the L-AgNPs were applied to the abscess model using the MDR bacterial strain, *S. aureus* LAC compared to a 1% lignin control (Figure 61). At a concentration of 10 mg/mL there is a slight decrease in abscess size, but no significant decrease in bacterial load. When the concentration is increased to 100 mg/mL there is a significant decrease in abscess size and slight downward trend in bacterial load when compared to a 1% lignin control. When the L-AgNPs are applied to the *P. aeruginosa* LESB strain there is a more significant concentration dependent decrease in abscess size compared to the *S. aureus* LAC strain, and a more significant decrease in bacterial load at a concentration of 100 mg/mL (Figure 62). However, at a concentration of 10 mg/mL there is essentially no change in bacterial load. These are significant

findings because this model produces a very resistant biofilm and is extremely difficult to treat. While a significant decrease is seen in the bacterial load when the L-AgNPs were applied against the *P. aeruginosa* LESB strain, the log reduction of 0.6 might not be therapeutically significant.

The high amounts of biofilm formation present in this model severely interfere with antimicrobial activity and antimicrobials can be ineffective at doses 100 to 10,000 times greater than their *in vitro* MIC [212]. The presence of biofilm is likely the reason that the L-AgNPs are not very effective below 100 mg/mL when the *in vitro* MIC for this strain is 2.5 µg/mL. Currently, the L-AgNPs are capable of significantly reducing the size of an abscess produced by *S. aureus* LAC strain or *P. aeruginosa* MDR strains. However, at a concentration of 10 mg/mL no significant reduction in bacterial load was observed when applied to the *P. aeruginosa* LESB bacterial strain, and no significant decrease in bacterial load was observed at any concentration applied to the *S. aureus* LAC strain. This is generally expected since AgNPs are considered to be more effective against Gram-negative bacteria than Gram-positive due to the more negatively charged cell membrane on Gram-negative bacteria and their thinner cell wall [137]. Since the L-AgNPs remain localized in the injection site (as determined by the biodistribution study in 3.3.3) it is likely that they are more efficient at treating more localized infections like those produced by the *P. aeruginosa* LESB strain.

It has also been identified that AgNPs show an immunological adjuvant effect when applied to mice via intraperitoneal or subcutaneous injection. Xu et al., determined that while AgNPs show some toxicity *in vitro,* they have a leukocyte and macrophage recruiting effect *in vivo* which provides an immunological adjuvant effect [213]. This immunological adjuvant effect would likely stimulate the immune system to better fight off the bacterial infection and speed up the process by which the abscess heals. It is likely that the antimicrobial effect combined with the immunological adjuvant effect is responsible for the decreases in bacterial load and abscess size. It is also likely that the presence of this immunological adjuvant effect is the reason for the very significant concentration dependent decrease in abscess size.

4.3.4 *In Vivo* Abscess Model Toxicity

Figure 63: Toxicity testing of particles produced by microwave-assisted synthesis using 20 mg/mL $AgNO_3$ and resuspended in PBS at 20 mg/mL (left) and 100 mg/mL (right)

When the L-AgNPs were injected subcutaneously, a significant amount of discoloration is visible, but no inflammation or necrotic tissue is observed (Figure 63). If significant amounts of inflammation were present there would be a significant amount of redness and additional blood vessels around the injection site. If necrotic tissue were present there would be a large necrotic lesion on the skin resulting from the host shutting off blood flow to the area causing tissue death. The absence of any inflammation or necrotic tissue means that while the particles discolor the injection site they likely are not toxic. However, more experiments should be performed to determine any hidden inflammation, including histology or assays to detect pro-inflammatory cytokines. The discoloration is likely due to the dark color of the lignin combined with the potential for AgNPs to discolor skin. Although the MTT assay showed slight toxicity to THP1 cells at a concentration of 10 µg/mL, there does not appear to be any direct toxicity when the particles are injected subcutaneously, even at concentrations up to 100 mg/mL.

4.4 Conclusion

The L-AgNPs produced by anaerobic 72-hour heating, aerobic 72-hour heating, and microwave-assisted synthesis methods all showed excellent antimicrobial activity against a wide variety of Gram-positive and Gram-negative bacterial strains *in vitro*. Compared to other AgNPs produced using natural compounds our L-AgNPs show superior antimicrobial activity with MICs ranging from 1 to 5 µg/mL compared to most AgNPs showing MICs ranging from 6.25 to 50 µg/mL (Table

1). One reason could be the presence of AgCl and Ag^0 in these particles, with future AgNPs preparations containing distinct and well controlled amounts of each. The L-AgNPs begin to show toxicity to human monocyte peripheral blood (THP-1) cells at around 10 µg/mL, which would still allow for their therapeutic application, as the MIC values for all produced particles were below 5 µg/mL.

When applied *in vivo* to a very difficult biofilm-forming abscess model only the L-AgNPs produced by microwave-assisted synthesis using 20 mg/mL $AgNO_3$ and concentrated to 100 mg/mL showed significant reductions in both abscess size and bacterial load only against *P. aeruginosa* LESB. It is likely that the reduction in abscess size and bacterial load is due to the significant recruitment of local leukocytes and macrophages combined with the antimicrobial activity of the L-AgNPs themselves. Additionally, some amount of discoloring was noted, but no significant toxicological effects were seen *in vivo* even at a concentration of 100 mg/mL. Significant difference in abscess size were seen with both the *S. aureus* LAC and *P. aeruginosa* LESB strains at concentrations of 10 mg/mL and 100 mg/mL.

Significantly more articles are published pertaining to the antimicrobial activity of AgNPs *in vitro* than *in vivo*. This could be due to the low antimicrobial activity of AgNPs *in vivo* or due to their significant toxicity profile when applied systemically. One possible explanation for this phenomenon is that AgNPs require the presence of oxygen for antimicrobial activity [133]. When particles are administered subcutaneously they receive significantly less oxygen than those administered as an antimicrobial wound dressing. Additionally, when AgNPs are injected IV they very quickly accumulate in the liver and spleen and may cause toxicity before significant antimicrobial activity is seen [154]. The toxicity profile of AgNPs when applied systemically *in vivo* is likely the reason that the majority of commercially available products containing antimicrobial silver is limited to wound dressings. It could also explain why there is a large gap in the literature between AgNPs *in vitro* and AgNPs *in vivo*.

Chapter 5: Conclusion

Overall, procedures were developed to produce highly stable lignin-capped silver nanoparticles (L-AgNPs) by anaerobic or aerobic 72-hour heating with a mean size of around 50 nm and excellent antimicrobial activity. A microwave-assisted synthesis method was also developed to decrease the processing time from 72-hours to 10 minutes while maintaining particle size, stability, chemical composition, and surface morphology. All produced particles were fully characterized by a variety of analytical chemistry methods to determine that the end product was indeed L-AgNPs.

The produced L-AgNPs were successfully radiolabeled using the two SPECT radioisotopes ^{123}I and ^{111}Ag. However, the particles produced with ^{111}Ag differed significantly from those produced without utilizing the silver radioisotope. The biodistribution of ^{123}I-labeled L-AgNPs was successfully investigated after subcutaneous injection from 10 minutes to 48 hours post-injection, and showed that the majority of the injected activity remained directly in the injection site. Further experiments should be conducted on this model including histology and ICP-MS to determine if the lignin becomes detached from the AgNP *in vivo*. It was successfully demonstrated that ^{111}Ag can be used to radioactively label L-AgNPs, and that it can be visualized by SPECT imaging. This research provides evidence for the possible use of ^{111}Ag to be used as a SPECT imaging isotope to monitor the biodistribution of AgNPs, and further studies investigating the production of L-AgNPs labeled with ^{111}Ag using a microwave-assisted synthesis should be conducted.

All produced L-AgNPs showed excellent antimicrobial activity against a wide variety of clinically isolated and ATCC MDR Gram-positive and Gram-negative bacteria *in vitro*. This is of significant relevance because the clinically isolated strains have been identified as drug-resistant human pathogens that are very difficult to treat. The produced particles also showed low toxicity both *in vitro* and *in vivo*. However, more experiments must be performed to determine the viability of cells treated with these particles and to determine if any inflammation is observed *in vivo*. The L-AgNPs produced a significant decrease in abscess size *in vivo* when administered subcutaneously to a biofilm-forming abscess produced by MDR bacteria at concentrations of 10 and 100 mg/mL. However, they were only effective at reducing the bacterial load for the *P. aeruginosa* LESB strain

at the highest concentration of 100 mg/mL. The L-AgNPs only caused a 0.6 log reduction, which means that its effect might be at a subtherapeutic level.

Our work contributes significantly to the field of antimicrobial AgNPs by going beyond the usual synthesis, characterization, and *in vitro* antimicrobial effects. It further examines the radioactive labeling, biodistribution, and *in vivo* antimicrobial effects of AgNPs in an abscess model. Significant information has been gained concerning the ability to determine the biodistribution of AgNPs by SPECT/CT imaging using ^{123}I and, in particular, the novel radioisotope ^{111}Ag. The limited availability of ^{111}Ag, however, significantly impacted the use of the silver radioisotope in this thesis. Additional AgNP synthesis and biodistribution studies utilizing ^{111}Ag as a SPECT radioisotope should be performed in the future. There is also significant potential for the further development of the intratracheal instillation model to determine both the biodistribution of the L-AgNPs, and to use them to treat MDR bacterial lung infections.

References

[1] Alanis AJ (2005). *Resistance to antibiotics: are we in the post-antibiotic era?* Archives of medical research **36**, 697-705.

[2] de Kraker ME, Stewardson AJ, Harbarth S (2016). *Will 10 million people die a year due to antimicrobial resistance by 2050?* PLoS medicine **13**, e1002184.

[3] Ventola CL (2015). *The antibiotic resistance crisis: part 1: causes and threats*. P & T : a peer-reviewed journal for formulary management **40**, 277-83.

[4] Boucher HW, Talbot GH, et al. (2009). *Bad Bugs, No Drugs: No ESKAPE! An Update from the Infectious Diseases Society of America*. Clinical Infectious Diseases **48**, 1-12.

[5] Centers for Disease Control and P (2013). *Antibiotic resistance threats in the United States, 2013. Atlanta: CDC; 2013*.

[6] Morel CM, Mossialos E (2010). *Stoking the antibiotic pipeline*. Bmj **340**, c2115.

[7] Maiti SN, Phillips OA, et al. (1998). *Beta-lactamase inhibitors: agents to overcome bacterial resistance*. Curr Med Chem **5**, 441-56.

[8] Boehr DD, Draker KA, et al. (2003). *Broad-spectrum peptide inhibitors of aminoglycoside antibiotic resistance enzymes*. Chem Biol **10**, 189-96.

[9] Piddock LJ (2006). *Clinically relevant chromosomally encoded multidrug resistance efflux pumps in bacteria*. Clin Microbiol Rev **19**, 382-402.

[10] Epand RM, Vogel HJ (1999). *Diversity of antimicrobial peptides and their mechanisms of action*. Bba-Biomembranes **1462**, 11-28.

[11] Hancock REW, Sahl HG (2006). *Antimicrobial and host-defense peptides as new anti-infective therapeutic strategies*. Nature Biotechnology **24**, 1551-1557.

[12] Zasloff M (2002). *Antimicrobial peptides of multicellular organisms*. Nature **415**, 389-95.

[13] Zasloff M (1987). *Magainins, a class of antimicrobial peptides from Xenopus skin: isolation, characterization of two active forms, and partial cDNA sequence of a precursor*. Proceedings of the National Academy of Sciences of the United States of America **84**, 5449-53.

[14] Giuliani A, Rinaldi AC (2011). *Beyond natural antimicrobial peptides: multimeric peptides and other peptidomimetic approaches*. Cellular and molecular life sciences : CMLS **68**, 2255-66.

[15] Scott RW, DeGrado WF, Tew GN (2008). *De novo designed synthetic mimics of antimicrobial peptides*. Curr Opin Biotechnol **19**, 620-7.

[16] Tew GN, Scott RW, et al. (2009). *De novo design of antimicrobial polymers, foldamers, and small molecules: from discovery to practical applications*. Accounts of chemical research **43**, 30-39.

[17] Biswas B, Adhya S, et al. (2002). *Bacteriophage therapy rescues mice bacteremic from a clinical isolate of vancomycin-resistant Enterococcus faecium*. Infect Immun **70**, 204-10.

[18] Lu TK, Koeris MS (2011). *The next generation of bacteriophage therapy*. Curr Opin Microbiol **14**, 524-31.

[19] d'Herelle F (1931). *Annual Graduate Fortnight. Medical and Surgical Aspects of Acute Bacterial Infections, October 20 to 31, 1930: Bacteriophage as a Treatment in Acute Medical and Surgical Infections*. Bulletin of the New York Academy of Medicine **7**, 329.

[20] Duckworth DH (1976). *" Who discovered bacteriophage?"*. Bacteriological reviews **40**, 793.
[21] Summers WC (2012). *The strange history of phage therapy*. Bacteriophage **2**, 130-133.
[22] Demaeyer P, Akodad EM, et al. (1993). *Disposition of liposomal gentamicin following intrabronchial administration in rabbits*. J Microencapsul **10**, 77-88.
[23] Dong Y, Chen S, et al. (2013). *Synergy of ultrasound microbubbles and vancomycin against Staphylococcus epidermidis biofilm*. The Journal of antimicrobial chemotherapy **68**, 816-26.
[24] Kole R, Krainer AR, Altman S (2012). *RNA therapeutics: beyond RNA interference and antisense oligonucleotides*. Nature reviews Drug discovery **11**, 125-40.
[25] Kurreck J (2003). *Antisense technologies. Improvement through novel chemical modifications*. European journal of biochemistry **270**, 1628-44.
[26] Maleki A, Shahmoradi B, et al. (2013). *Assessment of ultrasound irradiation on inactivation of gram negative and positive bacteria isolated from hospital in aqueous solution*. Journal of Advances in Environmental Health Research **1**
[27] Martin I, Jayaraman G, et al. (2011). *Trends in antimicrobial resistance in Neisseria gonorrhoeae isolated in Canada: 2000-2009*. Sex Transm Dis **38**, 892-8.
[28] Millezi AF, Caixeta DS, et al. (2012). *In vitro antimicrobial properties of plant essential oils thymus vulgaris, cymbopogon citratus and laurus nobilis against five important foodborne pathogens*. Ciencia Tecnol Alime **32**, 167-172.
[29] Wong JP, Yang H, et al. (2003). *Liposome delivery of ciprofloxacin against intracellular Francisella tularensis infection*. Journal of controlled release : official journal of the Controlled Release Society **92**, 265-73.
[30] Bhushan B (2017). *Springer handbook of nanotechnology*. Springer
[31] Council NSaT (2017). *The National Nanotechnology Initiative Supplement to the Presidents 2018 Budget*. In: Council NSaT (ed)
[32] Congress US (2003). *21st century nanotechnology research and development act*. Public Law **108**, 153.
[33] Iso N (2008). *Terminology and definitions for nano-objectsâ€“Nanoparticle, nanofibre and nanoplate*. ISO/TS **27687**
[34] Salata O (2004). *Applications of nanoparticles in biology and medicine*. J Nanobiotechnology **2**, 3.
[35] Dhand C, Dwivedi N, et al. (2015). *Methods and strategies for the synthesis of diverse nanoparticles and their applications: a comprehensive overview*. Rsc Advances **5**, 105003-105037.
[36] Valodkar M, Modi S, et al. (2011). *Synthesis and anti-bacterial activity of Cu, Ag and Cu-Ag alloy nanoparticles: A green approach*. Materials Research Bulletin **46**, 384-389.
[37] Dev A, Binulal NS, et al. (2010). *Preparation of poly(lactic acid)/chitosan nanoparticles for anti-HIV drug delivery applications*. Carbohydrate Polymers **80**, 833-838.
[38] Gupta R, Bajpai AK (2011). *Magnetically guided release of ciprofloxacin from superparamagnetic polymer nanocomposites*. Journal of biomaterials science Polymer edition **22**, 893-918.
[39] Mishra RK, Segal E, et al. (2015). *New life for an old antibiotic*. ACS Appl Mater Interfaces **7**, 7324-33.

[40] Rejinold NS, Muthunarayanan M, et al. (2011). *Curcumin-loaded biocompatible thermoresponsive polymeric nanoparticles for cancer drug delivery*. J Colloid Interface Sci **360**, 39-51.
[41] Saraogi GK, Gupta P, et al. (2010). *Gelatin nanocarriers as potential vectors for effective management of tuberculosis*. International Journal of Pharmaceutics **385**, 143-149.
[42] Wilson B, Samanta MK, et al. (2010). *Chitosan nanoparticles as a new delivery system for the anti-Alzheimer drug tacrine*. Nanomed-Nanotechnol **6**, 144-152.
[43] Slavin YN, Asnis J, et al. (2017). *Metal nanoparticles: understanding the mechanisms behind antibacterial activity*. J Nanobiotechnology **15**, 65.
[44] Klasen HJ (2000). *Historical review of the use of silver in the treatment of burns. I. Early uses*. Burns **26**, 117-130.
[45] Rai M, Yadav A, Gade A (2009). *Silver nanoparticles as a new generation of antimicrobials*. Biotechnology Advances **27**, 76-83.
[46] Owens B (2013). *Silver makes antibiotics thousands of times more effective*. Nature News **19**
[47] Lansdown ABG (2004). *A review of the use of silver in wound care: facts and fallacies*. British journal of nursing **13**, S6-S19.
[48] Prabhu S, Poulose EK (2012). *Silver nanoparticles: mechanism of antimicrobial action, synthesis, medical applications, and toxicity effects*. International nano letters **2**, 32.
[49] Chernousova S, Epple M (2012). *Silver as antibacterial agent: ion, nanoparticle, and metal*. Angewandte Chemie International Edition **52**, 1636-1653.
[50] Hu S, Hsieh Y-L (2015). *Silver nanoparticle synthesis using lignin as reducing and capping agents: A kinetic and mechanistic study*. International journal of biological macromolecules **82**, 856-862.
[51] Hu SX, Hsieh YL (2015). *Synthesis of surface bound silver nanoparticles on cellulose fibers using lignin as multi-functional agent*. Carbohydrate Polymers **131**, 134-141.
[52] Aweda TA, Ikotun O, et al. (2013). *The use of Ag-111 as a tool for studying biological distribution of silver-based antimicrobials*. Medchemcomm **4**, 1015-1017.
[53] Aweda TA, Zhang S, et al. (2015). *Investigating the pharmacokinetics and biological distribution of silver-loaded polyphosphoester-based nanoparticles using 111Ag as a radiotracer*. Journal of Labelled Compounds and Radiopharmaceuticals **58**, 234-241.
[54] Dizaj SM, Lotfipour F, et al. (2014). *Antimicrobial activity of the metals and metal oxide nanoparticles*. Materials science & engineering C, Materials for biological applications **44**, 278-84.
[55] Mody VV, Siwale R, et al. (2010). *Introduction to metallic nanoparticles*. Journal of pharmacy & bioallied sciences **2**, 282-9.
[56] Becker MF, Brock JR, et al. (1998). *Metal nanoparticles generated by laser ablation*. Nanostructured Materials **10**, 853-863.
[57] Liang CH, Shimizu Y, et al. (2005). *Preparation of ultrafine TiO2 nanocrystals via pulsed-laser ablation of titanium metal in surfactant solution*. Appl Phys a-Mater **80**, 819-822.
[58] Mafuné F, Kohno J-y, et al. (2002). *Full physical preparation of size-selected gold nanoparticles in solution: laser ablation and laser-induced size control*. The Journal of Physical Chemistry B **106**, 7575-7577.

[59] Mafuné F, Kohno J-y, et al. (2000). *Formation and size control of silver nanoparticles by laser ablation in aqueous solution*. The Journal of Physical Chemistry B **104**, 9111-9117.
[60] Yeh MS, Yang YS, et al. (1999). *Formation and characteristics of Cu colloids from CuO powder by laser irradiation in 2-propanol*. J Phys Chem B **103**, 6851-6857.
[61] Horikoshi S, Serpone N (2013). *Microwaves in nanoparticle synthesis: fundamentals and applications*. John Wiley & Sons
[62] Choi DS, Robertson AW, et al. (2016). *Low-Temperature Chemical Vapor Deposition Synthesis of Pt-Co Alloyed Nanoparticles with Enhanced Oxygen Reduction Reaction Catalysis*. Adv Mater **28**, 7115-22.
[63] Stopić S, Friedrich B, et al. (2008). *Characterization of nano-powder morphology obtained by ultrasonic spray pyrolysis*. Metalurgija **14**, 41-54.
[64] Thanh NT, Maclean N, Mahiddine S (2014). *Mechanisms of nucleation and growth of nanoparticles in solution*. Chem Rev **114**, 7610-30.
[65] Polte J, Ahner TT, et al. (2010). *Mechanism of gold nanoparticle formation in the classical citrate synthesis method derived from coupled in situ XANES and SAXS evaluation*. J Am Chem Soc **132**, 1296-301.
[66] Schmid G (2005). *General Introduction*. Nanoparticles. Wiley-VCH Verlag GmbH & Co. KGaA, 1-3.
[67] Wiley B, Sun Y, et al. (2005). *Shape-controlled synthesis of metal nanostructures: the case of silver*. Chemistry **11**, 454-63.
[68] Iravani S, Korbekandi H, et al. (2014). *Synthesis of silver nanoparticles: chemical, physical and biological methods*. Res Pharm Sci **9**, 385-406.
[69] Capek I (2017). *Noble Metal Nanoparticles*. Noble Metal Nanoparticles: Preparation, Composite Nanostructures, Biodecoration and Collective Properties. Springer Japan, Tokyo, 125-210.
[70] Du L, Jiang H, et al. (2007). *Biosynthesis of gold nanoparticles assisted by Escherichia coli DH51 and its application on direct electrochemistry of hemoglobin*. Electrochemistry Communications **9**, 1165-1170.
[71] Duran N, Marcato PD, et al. (2011). *Mechanistic aspects in the biogenic synthesis of extracellular metal nanoparticles by peptides, bacteria, fungi, and plants*. Appl Microbiol Biotechnol **90**, 1609-24.
[72] Husseiny MI, El-Aziz MA, et al. (2007). *Biosynthesis of gold nanoparticles using Pseudomonas aeruginosa*. Spectrochim Acta A **67**, 1003-1006.
[73] Iravani S (2011). *Green synthesis of metal nanoparticles using plants*. Green Chemistry **13**, 2638-2650.
[74] Narayanan KB, Sakthivel N (2010). *Biological synthesis of metal nanoparticles by microbes*. Adv Colloid Interface Sci **156**, 1-13.
[75] Shahverdi AR, Minaeian S, et al. (2007). *Rapid synthesis of silver nanoparticles using culture supernatants of Enterobacteria: A novel biological approach*. Process Biochemistry **42**, 919-923.
[76] Raveendran P, Fu J, Wallen SL (2003). *Completely "green" synthesis and stabilization of metal nanoparticles*. J Am Chem Soc **125**, 13940-1.
[77] Kalishwaralal K, Deepak V, et al. (2008). *Extracellular biosynthesis of silver nanoparticles by the culture supernatant of Bacillus licheniformis*. Materials Letters **62**, 4411-4413.

[78] Klaus-Joerger T, Joerger R, et al. (2001). *Bacteria as workers in the living factory: metal-accumulating bacteria and their potential for materials science*. Trends in Biotechnology **19**, 15-20.
[79] Konishi Y, Ohno K, et al. (2007). *Bioreductive deposition of platinum nanoparticles on the bacterium Shewanella algae*. J Biotechnol **128**, 648-53.
[80] Lang C, Schuler D (2006). *Biogenic nanoparticles: production, characterization, and application of bacterial magnetosomes*. J Phys-Condens Mat **18**, S2815-S2828.
[81] Lengke MF, Fleet ME, Southam G (2006). *Morphology of gold nanoparticles synthesized by filamentous cyanobacteria from gold(I)-thiosulfate and gold(III)--chloride complexes*. Langmuir **22**, 2780-7.
[82] Prasad K, Jha AK, Kulkarni AR (2007). *Lactobacillus assisted synthesis of titanium nanoparticles*. Nanoscale Research Letters **2**, 248-250.
[83] Yong P, Rowson NA, et al. (2002). *Bioreduction and biocrystallization of palladium by Desulfovibrio desulfuricans NCIMB 8307*. Biotechnol Bioeng **80**, 369-79.
[84] Dhuper S, Panda D, Nayak PL (2012). *Green synthesis and characterization of zero valent iron nanoparticles from the leaf extract of Mangifera indica*. Nano Trends: J Nanotech App **13**, 16-22.
[85] Begum NA, Mondal S, et al. (2009). *Biogenic synthesis of Au and Ag nanoparticles using Aqueous solutions of Black Tea leaf extracts*. Colloid Surface B **71**, 113-118.
[86] Vilchis-Nestor AR, Sanchez-Mendieta V, et al. (2008). *Solventless synthesis and optical properties of Au and Ag nanoparticles using Camellia sinensis extract*. Materials Letters **62**, 3103-3105.
[87] Daniel SCGK, Banu BN, et al. (2014). *Ipomea carnea-based silver nanoparticle synthesis for antibacterial activity against selected human pathogens*. Journal of Experimental Nanoscience **9**, 197-209.
[88] Ghaffari-Moghaddam M, Hadi-Dabanlou R, et al. (2014). *Green synthesis of silver nanoparticles using plant extracts*. Korean Journal of Chemical Engineering **31**, 548-557.
[89] Nazeruddin GM, Prasad NR, et al. (2014). *Extracellular biosynthesis of silver nanoparticle using Azadirachta indica leaf extract and its anti-microbial activity*. Journal of Alloys and Compounds **583**, 272-277.
[90] Roy N, Gaur A, et al. (2013). *Green synthesis of silver nanoparticles: an approach to overcome toxicity*. Environ Toxicol Pharmacol **36**, 807-12.
[91] Shankar SS, Ahmad A, Sastry M (2003). *Geranium leaf assisted biosynthesis of silver nanoparticles*. Biotechnol Prog **19**, 1627-31.
[92] Vidhu VK, Philip D (2014). *Spectroscopic, microscopic and catalytic properties of silver nanoparticles synthesized using Saraca indica flower*. Spectrochim Acta A **117**, 102-108.
[93] Hitchcock RT (2001). *Radio-Frequency and Microwave Radiation*. Wiley Online Library
[94] Greene DL, Mingos DMP (1991). *Application of Microwave Dielectric Loss Heating Effects for the Rapid and Convenient Synthesis of Ruthenium(Ii) Polypyridine Complexes*. Transition Metal Chemistry **16**, 71-72.
[95] Kappe CO, Stadler A, Dallinger D (2012). *Microwaves in organic and medicinal chemistry*. John Wiley & Sons
[96] Stuerga D, Delmotte M, et al. (2006). *Microwaves in organic synthesis*.

[97] Grace AN, Pandian K (2007). *One pot synthesis of polymer protected Pt, Pd, Ag and Ru nanoparticles and nanoprisms under reflux and microwave mode of heating in glycerol - A comparative study*. Materials Chemistry and Physics **104**, 191-198.
[98] Gabriel C, Gabriel S, et al. (1998). *Dielectric parameters relevant to microwave dielectric heating*. Chemical Society Reviews **27**, 213-223.
[99] Wiese GR, Healy TW (1970). *Effect of particle size on colloid stability*. Transactions of the Faraday Society **66**, 490-499.
[100] Van der Waals JD (1873). *Over de Continuiteit van den Gas-en Vloeistoftoestand*. Sijthoff
[101] Derjaguin BV (1941). *Theory of the stability of strongly charged lyophobic sols and the adhesion of strongly charged particles in solutions of electrolytes*. Acta Physicochim USSR **14**, 633-662.
[102] Malvern *Zetasizer Nano Series*. https://www.malvern.com/en/products/product-range/zetasizer-range/zetasizer-nano-range/zetasizer-nano-z
[103] Stern O (1924). *The theory of the electrolytic double-layer*. Z Elektrochem **30**, 1014-1020.
[104] Kirby BJ (2010). *Micro-and nanoscale fluid mechanics: transport in microfluidic devices*. Cambridge university press
[105] áO'Brien RW (1990). *Electroacoustic studies of moderately concentrated colloidal suspensions*. Faraday Discussions of the Chemical Society **90**, 301-312.
[106] Napper DH (1977). *Steric stabilization*. Plenary and Invited Lectures. Elsevier, 413-430.
[107] Dorobantu LS, Fallone C, et al. (2015). *Toxicity of silver nanoparticles against bacteria, yeast, and algae*. Journal of Nanoparticle Research **17**, 172.
[108] Inbaraj BS, Kao TH, et al. (2011). *The synthesis and characterization of poly (Î³-glutamic acid)-coated magnetite nanoparticles and their effects on antibacterial activity and cytotoxicity*. Nanotechnology **22**, 075101.
[109] Kumar A, Pandey AK, et al. (2011). *Engineered ZnO and TiO2 nanoparticles induce oxidative stress and DNA damage leading to reduced viability of Escherichia coli*. Free Radical Biology and Medicine **51**, 1872-1881.
[110] Leung YH, Ng AM, et al. (2014). *Mechanisms of antibacterial activity of MgO: non-ROS mediated toxicity of MgO nanoparticles towards Escherichia coli*. Small **10**, 1171-83.
[111] Nazari P, Dowlatabadi-Bazaz R, et al. (2014). *The antimicrobial effects and metabolomic footprinting of carboxyl-capped bismuth nanoparticles against Helicobacter pylori*. Appl Biochem Biotechnol **172**, 570-9.
[112] Simon-Deckers A, Loo S, et al. (2009). *Size-, Composition- and Shape-Dependent Toxicological Impact of Metal Oxide Nanoparticles and Carbon Nanotubes toward Bacteria*. Environmental Science & Technology **43**, 8423-8429.
[113] Sohm B, Immel F, et al. (2015). *Insight into the primary mode of action of TiO2 nanoparticles on Escherichia coli in the dark*. Proteomics **15**, 98-113.
[114] Xie Y, He Y, et al. (2011). *Antibacterial activity and mechanism of action of zinc oxide nanoparticles against Campylobacter jejuni*. Appl Environ Microbiol **77**, 2325-31.
[115] Rudramurthy GR, Swamy MK, et al. (2016). *Nanoparticles: Alternatives Against Drug-Resistant Pathogenic Microbes*. Molecules **21**, 836.
[116] Adams AP, Santschi EM, Mellencamp MA (1999). *Antibacterial properties of a silver chloride-coated nylon wound dressing*. Veterinary surgery : VS **28**, 219-25.

[117] Dasgupta MK (1994). *Silver peritoneal catheters reduce bacterial colonization*. Advances in peritoneal dialysis Conference on Peritoneal Dialysis **10**, 195-8.
[118] Greenfeld JI, Sampath L, et al. (1995). *Decreased bacterial adherence and biofilm formation on chlorhexidine and silver sulfadiazine-impregnated central venous catheters implanted in swine*. Crit Care Med **23**, 894-900.
[119] Maynard A, Michelson E (2006). *The nanotechnology consumer products inventory*. Woodrow Wilson International Center for Scholars, Washington, DC, accessed March **23**
[120] Brett DW (2006). *A discussion of silver as an antimicrobial agent: Alleviating the confusion*. Ostomy Wound Manag **52**, 34-41.
[121] Jain J, Arora S, et al. (2009). *Silver Nanoparticles in Therapeutics: Development of an Antimicrobial Gel Formulation for Topical Use*. Molecular Pharmaceutics **6**, 1388-1401.
[122] Dipankar C, Murugan S (2012). *The green synthesis, characterization and evaluation of the biological activities of silver nanoparticles synthesized from Iresine herbstii leaf aqueous extracts*. Colloids and surfaces B, Biointerfaces **98**, 112-9.
[123] Krishnaraj C, Jagan EG, et al. (2010). *Synthesis of silver nanoparticles using Acalypha indica leaf extracts and its antibacterial activity against water borne pathogens*. Colloid Surface B **76**, 50-56.
[124] Wei DW, Sun WY, et al. (2009). *The synthesis of chitosan-based silver nanoparticles and their antibacterial activity*. Carbohydrate Research **344**, 2375-2382.
[125] Sun Q, Cai X, et al. (2014). *Green synthesis of silver nanoparticles using tea leaf extract and evaluation of their stability and antibacterial activity*. Colloid Surface A **444**, 226-231.
[126] Kumar S, Singh M, et al. (2014). *Mechanistic study of antibacterial activity of biologically synthesized silver nanocolloids*. Colloid Surface A **449**, 82-86.
[127] Raut RW, Mendhulkar VD, Kashid SB (2014). *Photosensitized synthesis of silver nanoparticles using Withania somnifera leaf powder and silver nitrate*. J Photoch Photobio B **132**, 45-55.
[128] Panáček A, Kvitek L, et al. (2006). *Silver colloid nanoparticles: synthesis, characterization, and their antibacterial activity*. The Journal of Physical Chemistry B **110**, 16248-16253.
[129] Sathishkumar M, Sneha K, et al. (2009). *Cinnamon zeylanicum bark extract and powder mediated green synthesis of nano-crystalline silver particles and its bactericidal activity*. Colloids and surfaces B, Biointerfaces **73**, 332-8.
[130] Shahverdi AR, Fakhimi A, et al. (2007). *Synthesis and effect of silver nanoparticles on the antibacterial activity of different antibiotics against Staphylococcus aureus and Escherichia coli*. Nanomedicine : nanotechnology, biology, and medicine **3**, 168-71.
[131] Wang YW, Tang H, et al. (2016). *Enhanced bactericidal toxicity of silver nanoparticles by the antibiotic gentamicin*. Environ Sci-Nano **3**, 788-798.
[132] Ahmed S, Ahmad M, et al. (2016). *A review on plants extract mediated synthesis of silver nanoparticles for antimicrobial applications: A green expertise*. J Adv Res **7**, 17-28.
[133] Xiu ZM, Zhang QB, et al. (2012). *Negligible particle-specific antibacterial activity of silver nanoparticles*. Nano Lett **12**, 4271-5.
[134] Abbaszadegan A, Ghahramani Y, et al. (2015). *The Effect of Charge at the Surface of Silver Nanoparticles on Antimicrobial Activity against Gram-Positive and Gram-Negative Bacteria: A Preliminary Study*. Journal of Nanomaterials **16**, 53.

[135] Sondi I, Salopek-Sondi B (2004). *Silver nanoparticles as antimicrobial agent: a case study on E-coli as a model for Gram-negative bacteria*. Journal of Colloid and Interface Science **275**, 177-182.
[136] McQuillan JS, Infante HG, et al. (2012). *Silver nanoparticle enhanced silver ion stress response in Escherichia coli K12*. Nanotoxicology **6**, 857-66.
[137] Kim JS, Kuk E, et al. (2007). *Antimicrobial effects of silver nanoparticles*. Nanomedicine : nanotechnology, biology, and medicine **3**, 95-101.
[138] Pal S, Tak YK, Song JM (2007). *Does the antibacterial activity of silver nanoparticles depend on the shape of the nanoparticle? A study of the gram-negative bacterium Escherichia coli*. Applied and Environmental Microbiology **73**, 1712-1720.
[139] Li XZ, Nikaido H, Williams KE (1997). *Silver-resistant mutants of Escherichia coli display active efflux of Ag+ and are deficient in porins*. J Bacteriol **179**, 6127-32.
[140] McQuillan JS, Shaw AM (2014). *Differential gene regulation in the Ag nanoparticle and Ag(+)-induced silver stress response in Escherichia coli: a full transcriptomic profile*. Nanotoxicology **8 Suppl 1**, 177-84.
[141] Feng QL, Wu J, et al. (2000). *A mechanistic study of the antibacterial effect of silver ions on Escherichia coli and Staphylococcus aureus*. J Biomed Mater Res **52**, 662-8.
[142] Klueh U, Wagner V, et al. (2000). *Efficacy of silver-coated fabric to prevent bacterial colonization and subsequent device-based biofilm formation*. J Biomed Mater Res **53**, 621-31.
[143] Monteiro DR, Silva S, et al. (2013). *Silver colloidal nanoparticles: effect on matrix composition and structure of Candida albicans and Candida glabrata biofilms*. J Appl Microbiol **114**, 1175-83.
[144] Rai MK, Deshmukh SD, et al. (2012). *Silver nanoparticles: the powerful nanoweapon against multidrug-resistant bacteria*. J Appl Microbiol **112**, 841-52.
[145] Kim S-H, Lee H-S, et al. (2011). *Antibacterial activity of silver-nanoparticles against Staphylococcus aureus and Escherichia coli*. Korean J Microbiol Biotechnol **39**, 77-85.
[146] Wang L, He H, et al. (2014). *Excellent antimicrobial properties of silver-loaded mesoporous silica SBA-15*. J Appl Microbiol **116**, 1106-18.
[147] Huang CC, Aronstam RS, et al. (2010). *Oxidative stress, calcium homeostasis, and altered gene expression in human lung epithelial cells exposed to ZnO nanoparticles*. Toxicology in vitro : an international journal published in association with BIBRA **24**, 45-55.
[148] Ramalingam B, Parandhaman T, Das SK (2016). *Antibacterial Effects of Biosynthesized Silver Nanoparticles on Surface Ultrastructure and Nanomechanical Properties of Gram-Negative Bacteria viz. Escherichia coli and Pseudomonas aeruginosa*. ACS Appl Mater Interfaces **8**, 4963-76.
[149] Stambe C, Atkins RC, et al. (2004). *The role of p38alpha mitogen-activated protein kinase activation in renal fibrosis*. Journal of the American Society of Nephrology : JASN **15**, 370-9.
[150] Xie H, Mason MM, Wise JP, Sr. (2011). *Genotoxicity of metal nanoparticles*. Rev Environ Health **26**, 251-68.
[151] Yamanaka M, Hara K, Kudo J (2005). *Bactericidal actions of a silver ion solution on Escherichia coli, studied by energy-filtering transmission electron microscopy and proteomic analysis*. Appl Environ Microbiol **71**, 7589-93.

[152] Dakal TC, Kumar A, et al. (2016). *Mechanistic Basis of Antimicrobial Actions of Silver Nanoparticles*. Front Microbiol **7**, 1831.
[153] Duran N, Duran M, et al. (2016). *Silver nanoparticles: A new view on mechanistic aspects on antimicrobial activity*. Nanomedicine : nanotechnology, biology, and medicine **12**, 789-799.
[154] Chrastina A, Schnitzer JE (2010). *Iodine-125 radiolabeling of silver nanoparticles for in vivo SPECT imaging*. Int J Nanomedicine **5**, 653-9.
[155] Farrag NS, El-Sabagh HA, et al. (2017). *Comparative study on radiolabeling and biodistribution of core-shell silver/polymeric nanoparticles-based theranostics for tumor targeting*. Int J Pharm **529**, 123-133.
[156] Ashraf A, Sharif R, et al. (2015). *In vivo evaluation of the biodistribution of intravenously administered naked and functionalised silver nanoparticles in rabbit*. IET Nanobiotechnol **9**, 368-74.
[157] Sun T, Zhang YS, et al. (2014). *Engineered nanoparticles for drug delivery in cancer therapy*. Angewandte Chemie **53**, 12320-64.
[158] Melnik EA, Buzulukov YP, et al. (2013). *Transfer of Silver Nanoparticles through the Placenta and Breast Milk during in vivo Experiments on Rats*. Acta Naturae **5**, 107-115.
[159] Audinot JN, Georgantzopoulou A, et al. (2013). *Identification and localization of nanoparticles in tissues by mass spectrometry*. Surface and Interface Analysis **45**, 230-233.
[160] Liu W, Wu Y, et al. (2010). *Impact of silver nanoparticles on human cells: effect of particle size*. Nanotoxicology **4**, 319-30.
[161] Kim YS, Kim JS, et al. (2008). *Twenty-eight-day oral toxicity, genotoxicity, and gender-related tissue distribution of silver nanoparticles in Sprague-Dawley rats*. Inhal Toxicol **20**, 575-83.
[162] Xue Y, Zhang S, et al. (2012). *Acute toxic effects and gender-related biokinetics of silver nanoparticles following an intravenous injection in mice*. Journal of applied toxicology : JAT **32**, 890-9.
[163] Lee KJ, Nallathamby PD, et al. (2007). *In vivo imaging of transport and biocompatibility of single silver nanoparticles in early development of zebrafish embryos*. ACS Nano **1**, 133-43.
[164] Tang JL, Xiong L, et al. (2008). *Influence of silver nanoparticles on neurons and blood-brain barrier via subcutaneous injection in rats*. Applied Surface Science **255**, 502-504.
[165] Ji JH, Jung JH, et al. (2007). *Twenty-eight-day inhalation toxicity study of silver nanoparticles in Sprague-Dawley rats*. Inhal Toxicol **19**, 857-71.
[166] National Research C (1982). *Drinking Water and Health,: Volume 4*. The National Academies Press, Washington, DC.
[167] Kim JS, Song KS, et al. (2013). *Genotoxicity, acute oral and dermal toxicity, eye and dermal irritation and corrosion and skin sensitisation evaluation of silver nanoparticles*. Nanotoxicology **7**, 953-60.
[168] Maneewattanapinyo P, Banlunara W, et al. (2011). *An evaluation of acute toxicity of colloidal silver nanoparticles*. The Journal of veterinary medical science **73**, 1417-23.
[169] Nakkala JR, Mata R, Sadras SR (2017). *Green synthesized nano silver: Synthesis, physicochemical profiling, antibacterial, anticancer activities and biological in vivo toxicity*. J Colloid Interface Sci **499**, 33-45.

[170] Lam PK, Chan ESY, et al. (2004). *In vitro cytotoxicity testing of a nanocrystalline silver dressing (Acticoat) on cultured keratinocytes*. British Journal of Biomedical Science **61**, 125-127.
[171] Tredget EE, Shankowsky HA, et al. (1998). *A matched-pair, randomized study evaluating the efficacy and safety of Acticoat silver-coated dressing for the treatment of burn wounds*. The Journal of burn care & rehabilitation **19**, 531-7.
[172] Wright JB, Lam K, et al. (2002). *Early healing events in a porcine model of contaminated wounds: effects of nanocrystalline silver on matrix metalloproteinases, cell apoptosis, and healing*. Wound repair and regeneration : official publication of the Wound Healing Society [and] the European Tissue Repair Society **10**, 141-51.
[173] Panyala NR, Pena-Mendez EM, Havel J (2008). *Silver or silver nanoparticles: a hazardous threat to the environment and human health?* J Appl Biomed **6**, 117-129.
[174] Ip M, Lui SL, et al. (2006). *Antimicrobial activities of silver dressings: an in vitro comparison*. J Med Microbiol **55**, 59-63.
[175] Tang J, Xiong L, et al. (2009). *Distribution, translocation and accumulation of silver nanoparticles in rats*. J Nanosci Nanotechnol **9**, 4924-32.
[176] Shockman GD, Barrett JF (1983). *Structure, function, and assembly of cell walls of gram-positive bacteria*. Annual review of microbiology **37**, 501-27.
[177] Beveridge TJ (1999). *Structures of gram-negative cell walls and their derived membrane vesicles*. Journal of Bacteriology **181**, 4725-4733.
[178] Cavassin ED, de Figueiredo LF, et al. (2015). *Comparison of methods to detect the in vitro activity of silver nanoparticles (AgNP) against multidrug resistant bacteria*. J Nanobiotechnology **13**, 64.
[179] Kim TH, Kim M, et al. (2012). *Size-dependent cellular toxicity of silver nanoparticles*. Journal of biomedical materials research Part A **100**, 1033-43.
[180] Livermore DM, Pearson A (2007). *Antibiotic resistance: location, location, location*. Clinical microbiology and infection : the official publication of the European Society of Clinical Microbiology and Infectious Diseases **13 Suppl 2**, 7-16.
[181] Hegstad K, Mikalsen T, et al. (2010). *Mobile genetic elements and their contribution to the emergence of antimicrobial resistant Enterococcus faecalis and Enterococcus faecium*. Clinical Microbiology and Infection **16**, 541-554.
[182] Magiorakos AP, Srinivasan A, et al. (2012). *Multidrug-resistant, extensively drug-resistant and pandrug-resistant bacteria: an international expert proposal for interim standard definitions for acquired resistance*. Clinical microbiology and infection : the official publication of the European Society of Clinical Microbiology and Infectious Diseases **18**, 268-81.
[183] Rice LB *Mechanisms of resistance and clinical relevance of resistance to Î²-lactams, glycopeptides, and fluoroquinolones* Mayo Clinic Proceedings 2012. Elsevier, 198-208.
[184] Munita JM, Arias CA (2016). *Mechanisms of Antibiotic Resistance*. Microbiol Spectr **4**
[185] Khan S, Mukherjee A, Chandrasekaran N (2011). *Silver nanoparticles tolerant bacteria from sewage environment*. J Environ Sci (China) **23**, 346-52.
[186] McHugh GL, Moellering R, et al. (1975). *Salmonella typhimurium resistant to silver nitrate, chloramphenicol, and ampicillin: A new threat in burn units?* The Lancet **305**, 235-240.

[187] Pümpel T, Schinner F (1986). *Silver tolerance and silver accumulation of microorganisms from soil materials of a silver mine*. Applied microbiology and Biotechnology **24**, 244-247.
[188] Lok CN, Ho CM, et al. (2007). *Silver nanoparticles: partial oxidation and antibacterial activities*. Journal of biological inorganic chemistry : JBIC : a publication of the Society of Biological Inorganic Chemistry **12**, 527-34.
[189] Samberg ME, Oldenburg SJ, Monteiro-Riviere NA (2010). *Evaluation of silver nanoparticle toxicity in skin in vivo and keratinocytes in vitro*. Environ Health Perspect **118**, 407-13.
[190] Silver S (2003). *Bacterial silver resistance: molecular biology and uses and misuses of silver compounds*. FEMS Microbiol Rev **27**, 341-53.
[191] Norgren M, Edlund H (2014). *Lignin: Recent advances and emerging applications*. Current Opinion in Colloid & Interface Science **19**, 409-416.
[192] Hu S, Hsieh Y-L (2016). *Silver nanoparticle synthesis using lignin as reducing and capping agents: A kinetic and mechanistic study*. International journal of biological macromolecules **82**, 856-862.
[193] Coccia F, Tonucci L, et al. (2013). *Palladium nanoparticles, stabilized by lignin, as catalyst for cross-coupling reactions in water*. Inorganica Chimica Acta **399**, 12-18.
[194] Coccia F, Tonucci L, et al. (2012). *One-pot synthesis of lignin-stabilised platinum and palladium nanoparticles and their catalytic behaviour in oxidation and reduction reactions*. Green Chemistry **14**, 1073-1078.
[195] Li P, Lv W, Ai S (2016). *Green and gentle synthesis of Cu2O nanoparticles using lignin as reducing and capping reagent with antibacterial properties*. Journal of Experimental Nanoscience **11**, 18-27.
[196] Buoro RM, Bacil RP, et al. (2013). *Lignin-AuNp modified carbon paste electrodes—Preparation, characterization, and applications*. Electrochimica Acta **96**, 191-198.
[197] Rak MJ, Friščić T, Moores AH (2016). *One-step, solvent-free mechanosynthesis of silver nanoparticle-infused lignin composites for use as highly active multidrug resistant antibacterial filters*. RSC Advances
[198] Huang ZY, Mills G, Hajek B (1993). *Spontaneous formation of silver particles in basic 2-propanol*. The Journal of Physical Chemistry **97**, 11542-11550.
[199] Zhang X-F, Liu Z-G, et al. (2016). *Silver nanoparticles: synthesis, characterization, properties, applications, and therapeutic approaches*. International journal of molecular sciences **17**, 1534.
[200] Das R, Nath SS, et al. (2010). *Synthesis of silver nanoparticles and their optical properties*. Journal of Experimental Nanoscience **5**, 357-362.
[201] Engh RA (2006). *X-Ray Crystallography, Basic Principles*. Encyclopedic Reference of Genomics and Proteomics in Molecular Medicine. Springer Berlin Heidelberg, Berlin, Heidelberg, 2026-2029.
[202] Durán N, Nakazato G, Seabra AB (2016). *Antimicrobial activity of biogenic silver nanoparticles, and silver chloride nanoparticles: an overview and comments*. Applied microbiology and biotechnology **100**, 6555-6570.
[203] Tomaszewska E, Soliwoda K, et al. (2013). *Detection Limits of DLS and UV-Vis Spectroscopy in Characterization of Polydisperse Nanoparticles Colloids*. Journal of Nanomaterials **2013**, 10.

[204] De Carlo S, Harris JR (2011). *Negative staining and Cryo-negative Staining of Macromolecules and Viruses for TEM*. Micron (Oxford, England : 1993) **42**, 117-131.
[205] Hu S, Hsieh Y-L (2015). *Synthesis of surface bound silver nanoparticles on cellulose fibers using lignin as multi-functional agent*. Carbohydrate Polymers **131**, 134-141.
[206] Helene OA, Vanin VR, et al. (2007). *Update of X-ray and Gamma-ray Decay Data Standards for Detector Calibration and Other Applications*. International Atomic Energy Agency: Vienna, 210.
[207] Mastren T, Radchenko V, et al. (2018). *Chromatographic separation of the theranostic radionuclide 111Ag from a proton irradiated thorium matrix*. Analytica chimica acta **998**, 75-82.
[208] Ortiz-Muñoz G, Looney MR (2015). *Non-invasive intratracheal instillation in mice*. Bio-protocol **5**
[209] Sung JH, Ji JH, et al. (2011). *Acute inhalation toxicity of silver nanoparticles*. Toxicology and industrial health **27**, 149-154.
[210] Martínez AT (2002). *Molecular biology and structure-function of lignin-degrading heme peroxidases*. Enzyme and Microbial Technology **30**, 425-444.
[211] Pera-Titus M, García-Molina V, et al. (2004). *Degradation of chlorophenols by means of advanced oxidation processes: a general review*. Applied Catalysis B: Environmental **47**, 219-256.
[212] Pletzer D, Mansour SC, et al. (2017). *New mouse model for chronic infections by Gram-negative bacteria enabling the study of anti-infective efficacy and host-microbe interactions*. mBio **8**, e00140-17.
[213] Xu Y, Tang H, et al. (2013). *Evaluation of the adjuvant effect of silver nanoparticles both in vitro and in vivo*. Toxicology letters **219**, 42-48.